Forward-Backward asymmetry in Λ_b production and search for the Ξ_b^- and Ω_b^- baryons in $p\bar{p}$ collisions at $\sqrt{s} = 1.96$ TeV

José Andrés García González

A thesis submitted to obtain the degree of Doctor in Science

Centro de Investigación y de Estudios Avanzados del Instituto Politécnico Nacional

Advisor: Dr. Eduard De la Cruz-Burelo

April 21, 2015

Acknowledgments

This dissertation was supported by the Centro de Investigación y de Estudios Avanzados del IPN (CINVESTAV Mexico), by the Consejo Nacional de Ciencia y Tecnología (CONACyT) by means of a scholarship for PhD degree with CVU number 270871, and by Fermi National Accelerator Laboratory.

"Natura non facit saltum"

Contents

Resumen

Presentamos la búsqueda de los bariónes pesados $\Xi_b^-(bsd)$ y $\Omega_b^-(ssb)$ en decaimientos $\Xi_b^- \to J/\psi\Xi^- \to J/\psi\Lambda\pi^-, J/\psi \to \mu^+\mu^-$ y $\Omega_b^- \to J/\psi\Omega^- \to J/\psi\Lambda K^-, J/\psi \to \mu^+\mu^-$ respectivamente. Analizamos la muestra de datos completa Run II, reprocesada utilizando el algoritmo de tracking extendido para aumentar la eficiencia de la reconstrucción de estos decaimientos. Para el barión Ξ_b^-, observamos un total de eventos de señal de $27,4 \pm 6,6$ candidatos, con una masa M $(\Xi_b^-) = 5,813 \pm 0,010$ GeV consistente con las mediciones existentes. Con base en estos resultados, esperamos ver 16 ± 8 eventos Ω_b^- en la muestra completa de datos, y 18 eventos de ruido. Observamos una estructura de señal con un total de 12.6 ± 4.6, correspondiente a una significancia estadística de 3σ. Se mide la masa de esta estructura para ser 6129 ± 13 MeV, mayor que la masa establecida en el PDG (CDF y LHCb). Hay una pequeña pero significativa superposición de estos eventos con la publicación original de DØ en 2008, que realizó la observación del barión Ω_b^-.

Abstract

We present a search for the heavy-flavor baryons $\Xi_b(bsd)$ and $\Omega_b^-(ssb)$ in decays $\Xi_b^- \to J/\psi\Xi^- \to J/\psi\Lambda\pi^-, J/\psi \to \mu^+\mu^-$ and $\Omega_b^- \to J/\psi\Omega^- \to J/\psi\Lambda K^-, J/\psi \to \mu^+\mu^-$ respectively. We analyse the full Run II data sample, reprocessed using the extended tracking algorithm to increase the efficiency for reconstructing these decays. For the Ξ_b, we observe a total signal yield of 27.4 ± 6.6 candidates, with a mass $\mathrm{M}(\Xi_b) = 5.813 \pm 0.010$ GeV consistent with existing measurements. Based on these findings, we expect to see 16 ± 8 Ω_b^- events in the full data sample, and 18 background events. We observe a peaking structure with a signal yield of 12.6 ± 4.6, corresponding to a statistical significance of 3σ. The mass of this structure is measured to be 6129 ± 13 MeV, higher than the established mass from the PDG (CDF and LHCb measurements). There is a small but significant overlap of these events with the original 2008 DØ publication, which claimed observation of the Ω_b^- baryon.

List of Figures

List of Tables

Chapter 1

Introduction

In 2007, DØ announced the first discovery of the heavy-flavor baryon Ξ_b (with quark content bsd), decaying to $J/\psi\Xi^-$ [1][1]. The measured mass of this state agreed with the expectations from the quark model [2, 3, 4, 5, 6, 7], and it has subsequently been seen by both CDF [8, 9] and LHCb [10, 11] collaborations, with the three experiments reporting consistent masses (see Table 1.1). In addition, CDF later reported an independent confirmation in the channel $\Xi_b \to \Xi_c^0\pi^-$ [9, 13]. A second analysis from DØ was published in 2008, reporting the first observation of the Ω_b^- baryon (with quark content bss) in the similar decay $\Omega_b^- \to \Omega^- J\psi$ [14]. In contrast to the Ξ_b^- case, the reported mass of the Ω_b^- was higher than the theoretical expectations [2, 3, 4, 5, 6, 7]. A later analysis by the CDF collaboration [15] determined a mass consistent with previous measurements, and around 100 MeV below the DØ value (see Table 1.1). CDF has subsequently released an updated measurement with their full data sample, consistent with their original publication [9]. In the absence of a third, independent, experimental input, it was not clear which of the two experiments was reporting the correct mass. However, recent LHC publications have confirmed the CDF value, with a high-precision measurement [10].

Naïvely, there are three possible explanations for the anomalous mass measurement from DØ. First, the observed resonance could be the result of a second particle, distinct from the Ω_b^- ; this is highly disfavored, with no reasonable candidates for such a specific decay chain, and no evidence from either CDF or LHCb of a second peak. Second, the resonance could be a genuine Ω_b^- signal, with the mass shifted due to some unexpected systematic effect; this is also extremely unlikely, since DØ has published many mass measurements, including the topologically identical Ξ_b^- case, and all masses are in good agreement with the world-average values. The remaining option is that the reported excess of events, interpreted as a Ω_b^- signal, was actually an upward statistical fluctuation of the background. A statistical significance in excess of 5σ was reported although there was some discussion about this topyc (see, for example, Ref. [16]). It is also worth noting that both CDF and LHCb observed significantly more Ξ_b^- candidates than Ω_b^- , with CDF converting this into a ratio of production fractions times branching ratios [15],

[1] Charge conjugate equivalents of decays are implicitly assumed throughout this note.

	$M(\Xi_b^-)$			$M(\Omega_b^-)$		
DØ	5774	$\pm$	19	6165	$\pm$	10
CDF	5793.4	$\pm$	1.8	6047.5	$\pm$	3.8
LHCb	5797.7	$\pm$	0.46	6046.0	$\pm$	2.2

Table 1.1: Summary of measured masses of Ξ_b^- and Ω_b^- baryons, using the most recent results from DØ [1, 14], CDF [9], and LHCb [10, 11, 12]. All measurements are given in MeV, with statistical and systematic uncertainties added in quadrature.

$$f_{\Omega_b^-/\Xi_b} = \frac{f(b \to \Omega_b^-) \cdot \mathcal{B}(\Omega_b^- \to J/\psi\Omega^-)}{f(b \to \Xi_b^-) \cdot \mathcal{B}(\Xi_b^- \to J/\psi\Xi^-)} = 0.27 \pm 0.12(\text{stat.}) \ \pm 0.01(syst.) \qquad (1.1)$$

In contrast, the DØ analysis reported a significantly higher Ω_b^- rate, $f = 0.80 \pm 0.32(\text{stat.}) \ ^{+0.14}_{-0.22}(\text{syst.})$ [14]. This inconsistency is perhaps another indication that the DØ signal is driven by a background fluctuation.

Given the clear disagreement between the original DØ Ω_b^- analysis, and the other experimental results, it is our duty to perform a thorough investigation of the DØ data, using both Run IIa and Run IIb samples. Many in-depth cross-checks of the original analysis have been performed, both prior to publication, and following the emergence of the mass anomaly; so far no problems have been found: the excess of events interpreted as the Ω_b^- signal appears to be genuine, rather than driven by some bug or bias in the selection. The aim of this analysis is to perform an independent blinded investigation of both Run IIa and Run IIb data, using multivariate selection techniques, to search first for the Ξ_b^- baryon, and then for the Ω_b^- . The first stage is to establish a Ξ_b^- signal which is then used as a reference and normalization channel to optimize the Ω_b^- search. We are including the unblinded results for both Ξ_b^- and Ω_b^- searches. A second tentative aim of this analysis is to extract the lifetime of the Ξ_b^- baryon.

Chapter 2

Theoretical framework

2.1 Standard Model

The theoretical model that have to describe what we believe are the building blocks of nature and the interactions, is known as the *Standard Model*. The Standard Model (SM) is the combination of Electroweak Theory and Quantum Chromodynamics into a single core in the attempt to include all interactions of subatomic particles except those due to gravity in a simple framework. This SM model (Figure 2.4) has proved to be highly accurate in predicting certain interactions, but it does not explain all aspects of subatomic particles. For example, it can not say how many particles there should be or what their masses should be. The search goes on for a more complete theory, and in particular an unified field theory describing the strong, weak, and electromagnetic forces. Twelve elementary particles that are known in the SM are the following: the Fermions. They have spin 1/2 and obey the Pauli Exclusion Principle. Fermions are divided into six Quarks: up u, down d, charm c, strange s, top t and, bottom b; and six Leptons: electron e, muon μ, tau τ, electron neutrino ν_e, muon neutrino ν_μ and, tau neutrino ν_τ . Quarks interact via the strong force because they carry color charge, electromagnetically because of their electric charge and via the weak nuclear interaction because of the weak isospin. Quarks form color-neutral composite particles known as Hadrons which are divided in Mesons, containing a quark and an antiquark and Baryons, made of three quarks. Leptons have no color charge and can not interact via the strong force. Only three of them have electric charge, hence they interact electromagnetically. The motion of non-electrically charged leptons, the neutrinos, is influenced only by the weak nuclear interaction

We will provide a brief description of how the use of symmetries will explain the existence of b baryons and how the braking of these symmetries will lead to the prediction of their masses. Current experimental results have confirm such predictions and they are in very good agreement whith them giving an other succesful result to the SM.

2.2 $\mathbf{SU(5)^3}$

We are going to find the representations of $SU(5)^3$ so we can find the multiplets that represent a baryon containing a b quark. We are using 5 quarks as basis vectors for SU(5) [25]:

$$u = \begin{pmatrix} 1 \\ 0 \\ 0 \\ 0 \\ 0 \end{pmatrix}, d = \begin{pmatrix} 0 \\ 1 \\ 0 \\ 0 \\ 0 \end{pmatrix}, s = \begin{pmatrix} 0 \\ 0 \\ 1 \\ 0 \\ 0 \end{pmatrix}, c = \begin{pmatrix} 0 \\ 0 \\ 0 \\ 1 \\ 0 \end{pmatrix}, b = \begin{pmatrix} 0 \\ 0 \\ 0 \\ 0 \\ 1 \end{pmatrix} \tag{2.1}$$

We will define $SU(5)^3$ as follows:

$$SU(5)^3 = SU(5) \otimes SU(5) \otimes SU(5)$$

The $SU(5)^3$ representations are the following:

$SU(5) \otimes SU(5) \otimes SU(5) =$ 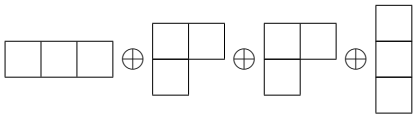 (2.2)

and we can calculate their dimension using the hook method as follows:

$$\begin{aligned} 5 \otimes 5 \otimes 5 &= \begin{array}{|c|c|c|}\hline 5 & 6 & 7 \\ \hline \end{array} \oplus \begin{array}{|c|c|}\hline 5 & 6 \\ \hline 4 \\ \cline{1-1} \end{array} \oplus \begin{array}{|c|c|}\hline 5 & 6 \\ \hline 4 \\ \cline{1-1} \end{array} \oplus \begin{array}{|c|}\hline 5 \\ \hline 4 \\ \hline 3 \\ \hline \end{array} \\ 125 &= \frac{5 \times 6 \times 7}{1 \times 2 \times 3} + \frac{5 \times 6 \times 4}{1 \times 3 \times 1} + \frac{5 \times 6 \times 4}{1 \times 3 \times 1} + \frac{5 \times 4 \times 3}{3 \times 2 \times 1} \\ 125 &= 35 + 40 + 40 + 10 \\ 125 &= 125 \end{aligned} \tag{2.3}$$

The $SU(4)^3$ subgroups that we are interestend on are the following:

$$\overset{SU(5)}{\begin{array}{|c|c|c|}\hline & & \\ \hline \end{array}} \supset \overset{SU(4)}{\begin{array}{|c|c|c|}\hline & & \\ \hline \end{array}} \oplus \overset{SU(4)}{\begin{array}{|c|c|c|}\hline & & b \\ \hline \end{array}} \oplus \overset{SU(4)}{\begin{array}{|c|c|c|}\hline & b & b \\ \hline \end{array}} \oplus \overset{SU(4)}{\begin{array}{|c|c|c|}\hline b & b & b \\ \hline \end{array}} \tag{2.4}$$

$$\overset{SU(5)}{\begin{array}{|c|c|}\hline & \\ \hline & \\ \cline{1-1} \end{array}} \supset \overset{SU(4)}{\begin{array}{|c|c|}\hline & \\ \hline & \\ \cline{1-1} \end{array}} \oplus \overset{SU(4)}{\begin{array}{|c|c|}\hline & b \\ \hline & \\ \cline{1-1} \end{array}} \oplus \overset{SU(4)}{\begin{array}{|c|c|}\hline & \\ \hline b & \\ \cline{1-1} \end{array}} \tag{2.5}$$

Now we are going to take the following $SU(3)^3$ subgroups that are useful to find the baryon multiplets that we are looking for:

$$\overset{SU(4)}{\begin{array}{|c|c|c|}\hline & & b \\ \hline \end{array}} \supset \overset{SU(3)}{\begin{array}{|c|c|c|}\hline & & b \\ \hline \end{array}} \oplus \overset{SU(3)}{\begin{array}{|c|c|c|}\hline & c & b \\ \hline \end{array}} \oplus \overset{SU(3)}{\begin{array}{|c|c|c|}\hline c & c & b \\ \hline \end{array}} \tag{2.6}$$

$$\overset{SU(4)}{\begin{array}{|c|c|}\hline & b \\ \hline & \\ \cline{1-1} \end{array}} \supset \overset{SU(3)}{\begin{array}{|c|c|}\hline & b \\ \hline & \\ \cline{1-1} \end{array}} \oplus \overset{SU(4)}{\begin{array}{|c|c|}\hline & b \\ \hline c & \\ \cline{1-1} \end{array}} \tag{2.7}$$

We are going to use the following eigenvalue equation:

$$\mathbf{H}\ \mathrm{q} = \mathbf{M}_q\ \mathrm{q},\ \ q = u, d, s, c, b \tag{2.8}$$

were $\mathbf{M}_q$ is the weight vector and $\mathbf{H}$ q is defined as:

$$\mathbf{H} \ \ = \ \ (\lambda^3, \lambda^8, \lambda^{15}, \lambda^{24}) \tag{2.9}$$

Using equation 2.8 we obtain that following weight vectors:

$$\mathbf{M}_u = (1, \frac{1}{\sqrt{3}}, \frac{1}{\sqrt{6}}, \frac{1}{\sqrt{10}}, \frac{1}{\sqrt{15}}) \tag{2.10}$$

$$\mathbf{M}_d = (-1, \frac{1}{\sqrt{3}}, \frac{1}{\sqrt{6}}, \frac{1}{\sqrt{10}}, \frac{1}{\sqrt{15}}) \tag{2.11}$$

$$\mathbf{M}_s = (0, -\frac{2}{\sqrt{3}}, \frac{1}{\sqrt{6}}, \frac{1}{\sqrt{10}}, \frac{1}{\sqrt{15}}) \tag{2.12}$$

$$\mathbf{M}_c = (0, 0, -\frac{3}{\sqrt{6}}, \frac{1}{\sqrt{10}}, \frac{1}{\sqrt{15}}) \tag{2.13}$$

$$\mathbf{M}_b = (0, 0, 0, -\frac{4}{\sqrt{10}}, \frac{1}{\sqrt{15}}) \tag{2.14}$$

As we know the weight vector of the product of representations for the $SU(3)^3$ subgroups of $SU(5)^3$ is the sum of three fundamental weights of SU(5). Equations 2.15 and 2.16 are the multiplets that have one b quark in such subgroups.

$$\begin{array}{|c|c|c|}\hline u & u & b \\ \hline \end{array}\ ,\ \begin{array}{|c|c|c|}\hline d & d & b \\ \hline \end{array}\ ,\ \begin{array}{|c|c|c|}\hline s & s & b \\ \hline \end{array}$$
$$\begin{array}{|c|c|c|}\hline u & d & b \\ \hline \end{array}\ ,\ \begin{array}{|c|c|c|}\hline u & s & b \\ \hline \end{array}\ ,\ \begin{array}{|c|c|c|}\hline d & s & b \\ \hline \end{array} \tag{2.15}$$

$$\begin{array}{|c|c|}\hline u & b \\ \hline d \\ \cline{1-1} \end{array}\ ,\ \begin{array}{|c|c|}\hline u & b \\ \hline s \\ \cline{1-1} \end{array}\ ,\ \begin{array}{|c|c|}\hline d & b \\ \hline s \\ \cline{1-1} \end{array} \tag{2.16}$$

By means of the weight diagrams we can draw the multiplets obtained from equations 2.15 and 2.16 as shown in Figure 2.1 and 2.2

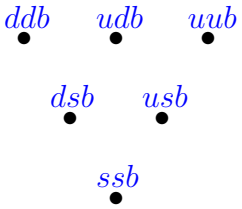

Figure 2.1: Baryons with one b quark from totaly symetric SU(3) subgroups of SU(5)

Using this procedure we can obtain all the b Baryons shonw on Figure 2.3. In the following section we will show that the SU(5) symmetry will be braken by means of a 1_{mQ} HQ expansion and this will allow us to calculate the mass of the baryons.

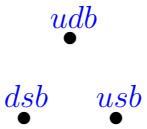

Figure 2.2: Baryons with one b quark from antisymetric SU(3) subgroups of SU(5)

2.3 SU(3) flavor symmetry

The mass spectrum of baryons containing a single heavy quark requires of approximate symmetries. In the heavy quark limit, hadrons containing a single heavy quark present a heavy quark spin-flavor symmetry [26]. For finite m_Q , this symmetry is broken by effects of order $1/m_Q$, and this symmetry braking combined with the $1/m_Q$ and $1/N_c$ expansions can be used to estimate the mass of b baryons as we will discuss in the next section (see Figure 2.3).

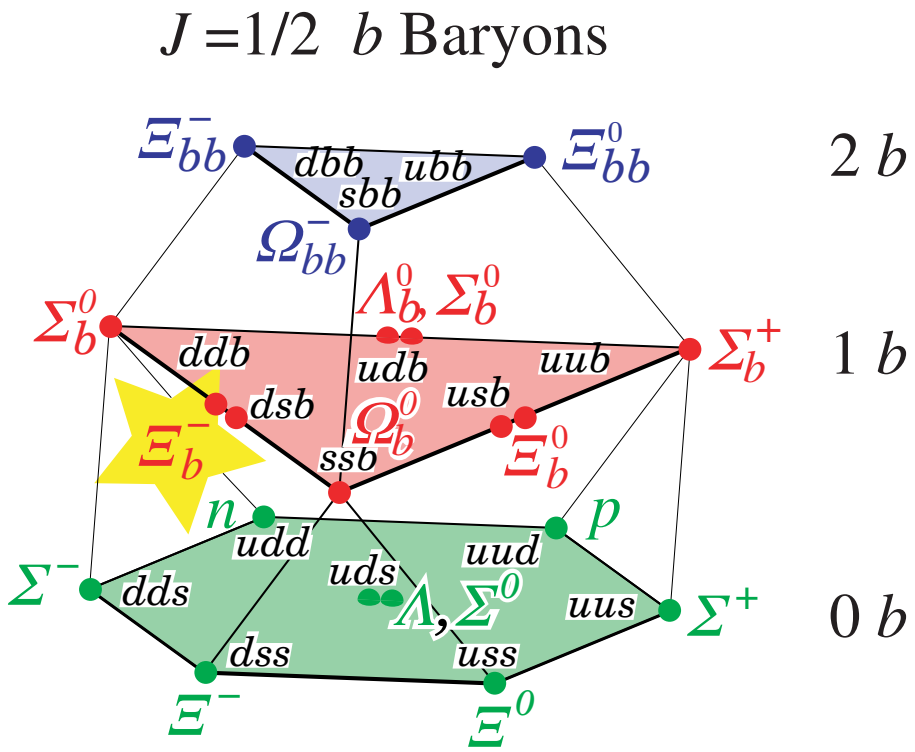

Figure 2.3: $J = 1/2$ bottom Baryons.

2.4 $1/m_Q$ and $1/N_c$ expansion

For finite $1/m_Q$, the spin-flavor symmetry is broken by effects of order $1/m_Q$. In the large-Nc limit, baryons with this flavor symmetry possess a larger spin-flavor symmetry [27]. For finite Nc , this symmetry is broken by effects of order $1/N_c$. SU(3) flavor breaking and the combined $1/m_Q$ and 1/Nc expansions for the masses of heavy quark baryons have established predictions for such values [28].

2.5 Heavy quark baryon masses in the $1/m_Q$ expansion

The masses of hadrons containing a single heavy quark have been studied in the $1/m_Q$ expansion of heavy quark effective theory. This procedure can lead to a estimation of the mass of a hadron containing a single heavy quark in a expansion of $1/m_Q$ [2, 29]:

$$M(H_Q) = m_Q + \bar{\Lambda} - \frac{\lambda_1}{2m_Q} - d_H \frac{\lambda_2}{2m_Q} + O\frac{1}{m_Q^2} \tag{2.17}$$

where the order unity contribution $\bar{\Lambda}$ is the mass of the light degrees of freedom in the hadron and the two $1/m_Q$ contributions are determined by the matrix elements:

$$\lambda_1 = \langle H_Q(\nu)|\bar{Q}_\nu(iD^2)Q_\nu|H_Q(\nu)\rangle \tag{2.18}$$

$$d_H\lambda_2 = \frac{1}{2}Z_Q\langle H_Q(\nu)|\bar{Q}_\nu g G_{\mu\nu}\sigma^{\mu\nu}Q_\nu|H_Q(\nu)\rangle \tag{2.19}$$

In the above equation, d_H is the Clebsch factor, $d_H = -4(J_l \cdot J_Q)$, and Z_Q is a renormalization factor with $Z_Q(\mu = m_Q) = 1$.

As an example, the baryons containing a single heavy quark Q with zero strangeness are the Λ_Q,Σ_Q, and Σ_Q^*. The HQET $1/m_Q$ expansion of these masses is given by:

$$\Lambda_Q = m_Q + \bar{\Lambda_T} - \frac{\lambda_{1T}}{2m_Q} + ... \tag{2.20}$$

$$\Sigma_Q = m_Q + \bar{\Lambda_S} - \frac{\lambda_{1S}}{2m_Q} - 4\frac{\lambda_2}{2m_Q} + ... \tag{2.21}$$

$$\Sigma_Q^* = m_Q + \bar{\Lambda_S} - \frac{\lambda_{1S}}{2m_Q} + 2\frac{\lambda_2}{2m_Q} + ... \tag{2.22}$$

Now the two expansions ($1/m_Q$ and $1/N_c$) give the following seven constraints that give the bottom baryon masses:

$$\begin{aligned}
\Sigma_b^* - \Sigma_b &\sim 23.8 \pm 1.6 \text{ Mev} \\
\Xi_b^* - \Xi_b^{'} &\sim 18.3 \pm 0.9 \text{ Mev} \\
\Omega_b^* - \Omega_b^{'} &\sim 12.8 \pm 2.2 \text{ Mev} \\
\frac{1}{6}[(\Sigma_b + 2\Sigma_b^*) - 2(\Xi_b^{'} + 2\Xi_b^*) + (\Omega_b + 2\Omega_b^*)] &= 4.43 \pm 1.5 \text{MeV}
\end{aligned} \tag{2.23}$$

where the errors represent the combined theoretical and experimental accuracy of each relation. There are two additional mass relations which are less accurate, with theoretical accuracies of about 4.8 and 5.1 MeV, respectively:

$$\begin{aligned}
\Lambda_b - \Xi_b &= 182.7 \pm 4.9 \text{ MeV} \\
-\frac{1}{3}(\Lambda_b + 2\Xi_b) + \frac{1}{18}[3(\Sigma_b + 2\Sigma_b^*) + 2(\Xi_b^{'} + 2\Xi_b^*) + (\Omega_b + 2\Omega_b^*)] &= 176.1 \pm 5.4 \text{ MeV}
\end{aligned} \tag{2.24}$$

Combined with the measured Λ_b mass, these seven constraints determine the seven masses $\Sigma_b^*, \Sigma_b^{'}, \Xi_b^*, \Xi_b^{'}, \Omega_b^*$ and $\Omega_b^{'}$. A more precise meassurment of masses and more precise theoritical estimations provide similar equations like 2.23 and 2.24, a more precise chromomagnetic mass spliting is provided in equations 2.25.

$$\begin{aligned}
\Sigma_b^* - \Sigma_b &= 15.8 \pm 3.3 \text{ Mev} \\
\Xi_b^* - \Xi_b^{'} &= 15.2 \pm 3.2 \text{ Mev} \\
\Omega_b^* - \Omega_b^{'} &= 14.5 \pm 3.3 \text{ Mev}
\end{aligned} \tag{2.25}$$

Now we can estimate the sextet masses of the bottom baryons and the Ξ_b by using the four equations 2.26:

$$\begin{aligned}
\frac{1}{6}[(\Sigma_b + 2\Sigma_b^*) - 2(\Xi_b^{'} + 2\Xi_b^*) + (\Omega_b + 2\Omega_b^*)] &= -4.43 \pm 1.5 \text{ MeV} \\
-\frac{5}{8}(\Lambda_b - \Xi_b) + \frac{1}{24}[3(\Sigma_b + 2\Sigma_b^*) - (\Xi_b^{'} + 2\Xi_b^*) - 2(\Omega_b + 2\Omega_b^*)] &= 37.5 \pm 1.6 \text{ MeV} \\
-\frac{1}{3}(\Lambda_b + 2\Xi_b) + \frac{1}{18}[3(\Sigma_b + 2\Sigma_b^*) + 2(\Xi_b^{'} + 2\Xi_b^*) + (\Omega_b + 2\Omega_b^*)] &= 172.6 \pm 5.3 \text{ MeV} \\
(\Lambda_b - \Xi_b) &= -182.7 \pm 5.0 \text{ MeV}
\end{aligned} \tag{2.26}$$

using the Λ_b mass and this equations the predicted sextet masses are summarised on Table 2.1.

Baryon	Mass(MeV)
Ξ_b	5805.7 ± 8.1
Σ_b	5824.2 ± 9.0
Σ_b^*	5840.0 ± 8.8
$\Xi_b^{'}$	5950.9 ± 8.5
Ξ_b^*	5966.1 ± 8.3
Ω_b	6068.7 ± 11.1
Ω_b^*	6083.2 ± 11.0

Table 2.1: Summary of predicted masses of b baryons.

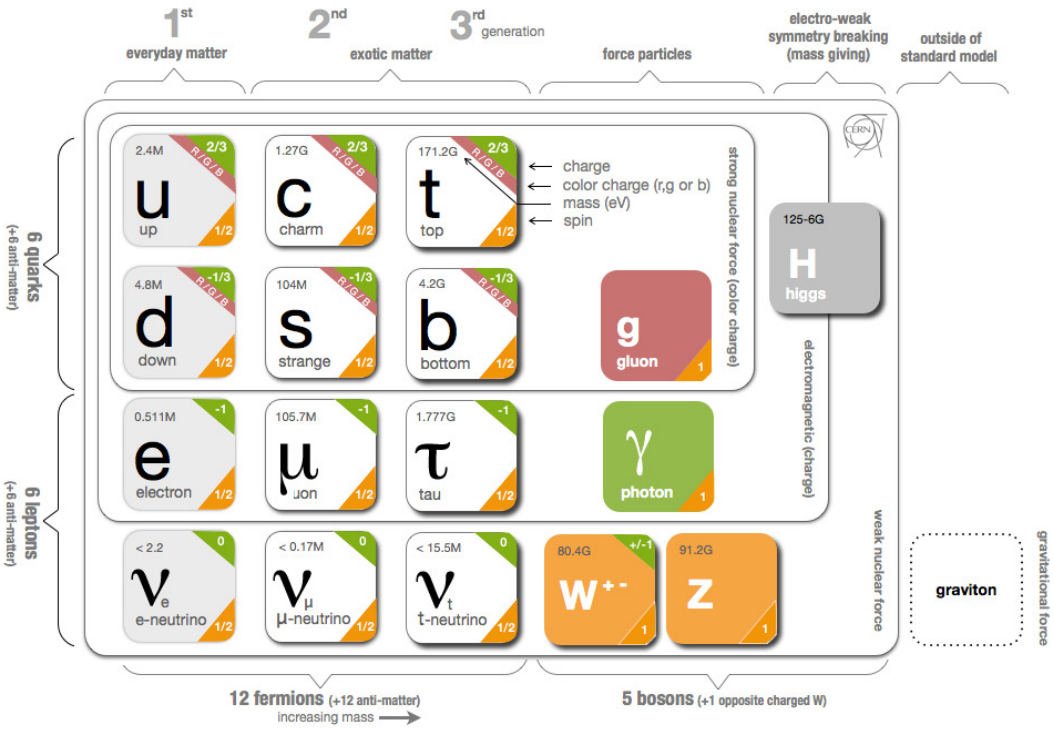

Figure 2.4: Leptons and Bosons in the SM

Chapter 3

Experimental apparatus

3.1 Tevatron

The Fermi National Accelerator Laboratory (Fermilab) had one of the most powerful accelerators at this moment: The Tevatron. This name comes from to the fact that this accelerator machine was the first to have enough power to reach the energy range of TeV. The energy in the center of mass was $\sqrt{s} = 1.96$ TeV. In the Figure 3.1 we present a sketch of the Fermilab accelerator facility. The Tevatron is the most important part, where two beams of protons and anti protons used to collide in two main points: CDF and DØ detectors. These two detectors are the place were the physics is happening, i.e. the place where we look for new physics and to confirm current predictions.

It is important to mention that many important contributions to physics have been done at this laboratory, for example, the discoveries of the bottom and top quarks. The main purpose of the two experiments mentioned above is to look for new discoveries that could enhance our knowledge of Nature. Tevatron was also working in the search for the Higgs boson and currently is contributing to the measurement of its spin and parity.

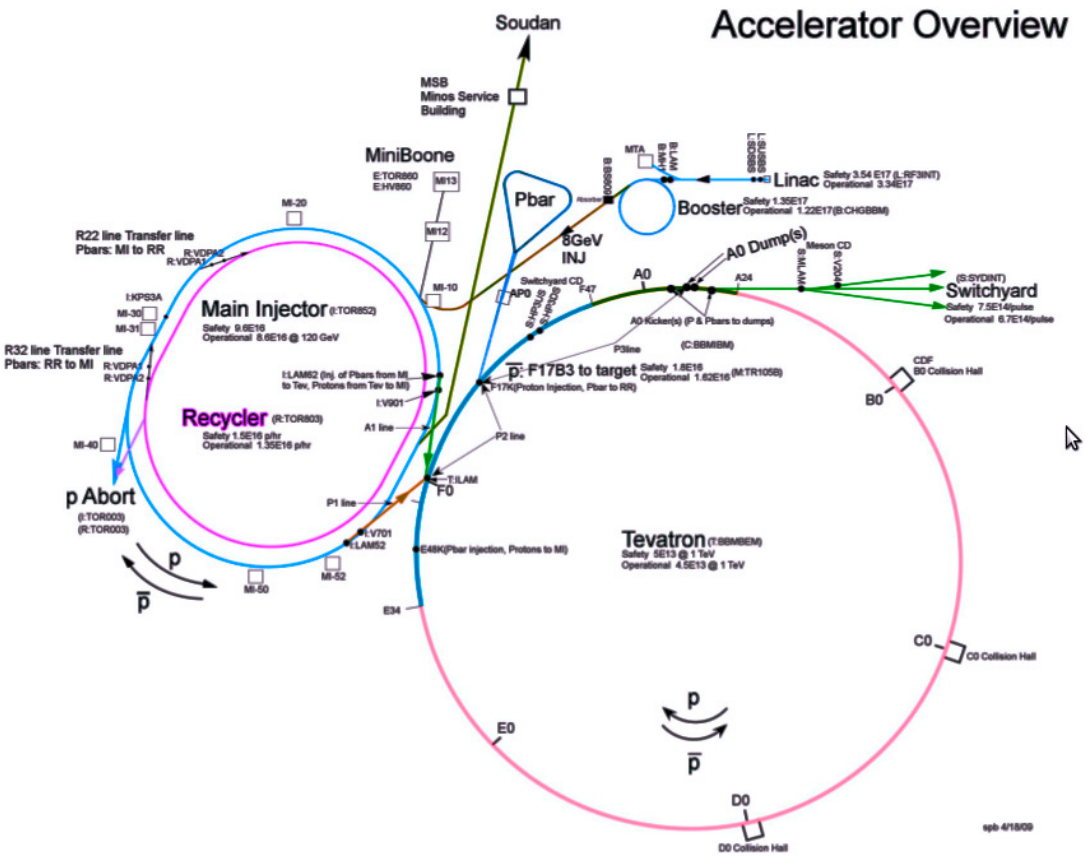

Figure 3.1: Tevatron accelerator at Fermilab.

3.2 The DØ Detector

As we can see in Figure 3.1 there are two detectors in Tevatron. DØ is the experiment where the CINVESTAV HEP Group collaborates at Fermilab and we explain the main structure of this detector in the next pages. The picture 3.2 is a general sketch of the DØ detector, and it is described in detail in reference [24]. In general, the detector can be divided in three main components: the tracking system, which itself is made of two sub detectors, the Silicon Micro-strip Tracker (SMT), and the Central Fiber Tracker (CFT); the calorimeter; and the muon system.

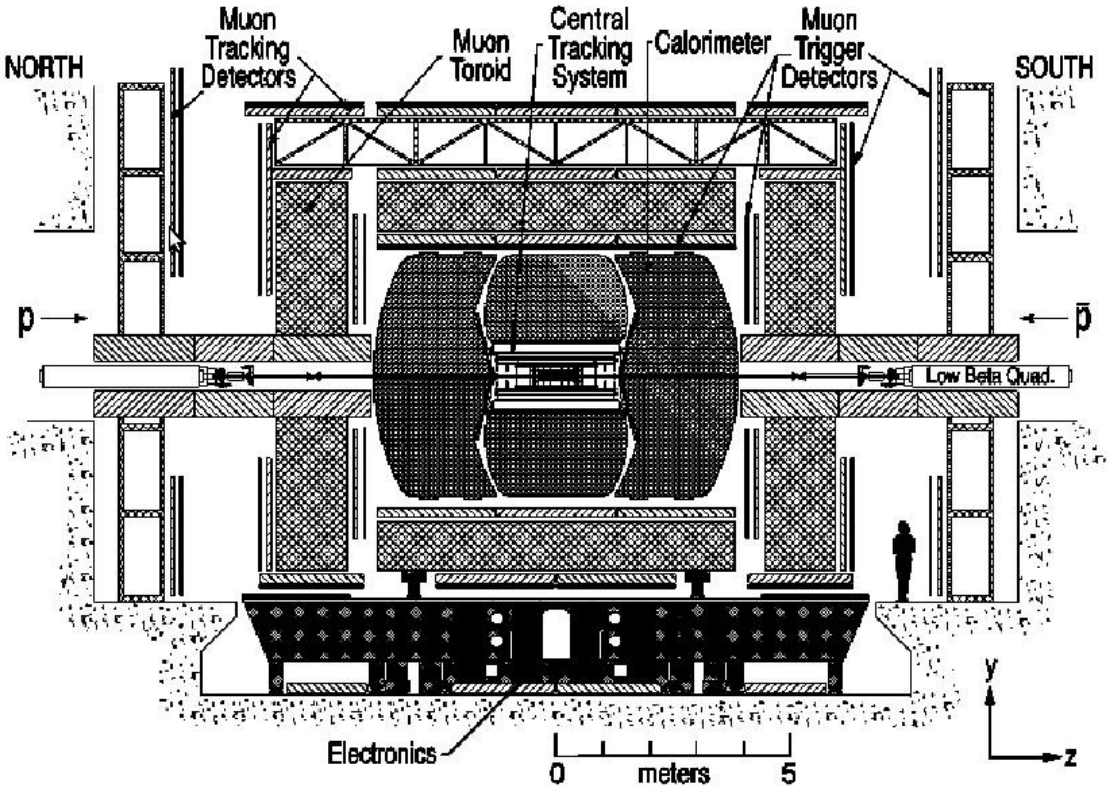

Figure 3.2: the DØ detector at Fermi-Lab

Figure 3.3 is one of the detector upgrade in which the main upgrade was the new central tracking system. This upgrade was at the beginning of the stage named run II[24].

For the next upgrade (RunIIb) the new hardware, named Layer 0 (L0), was an extension of the SMT. An axial view of the tracking system before the L0 is show in the Figure 3.4 a, and the axial view of the L0 can be seeing at Figure 3.4 b .

This implementation had the intention to maximize the signal to noise ratio (S/N). All these improvements mentioned above correspond to the actual state of the DØ Detector. Another very important system is the Central Fiber Tracker or CFT that together with

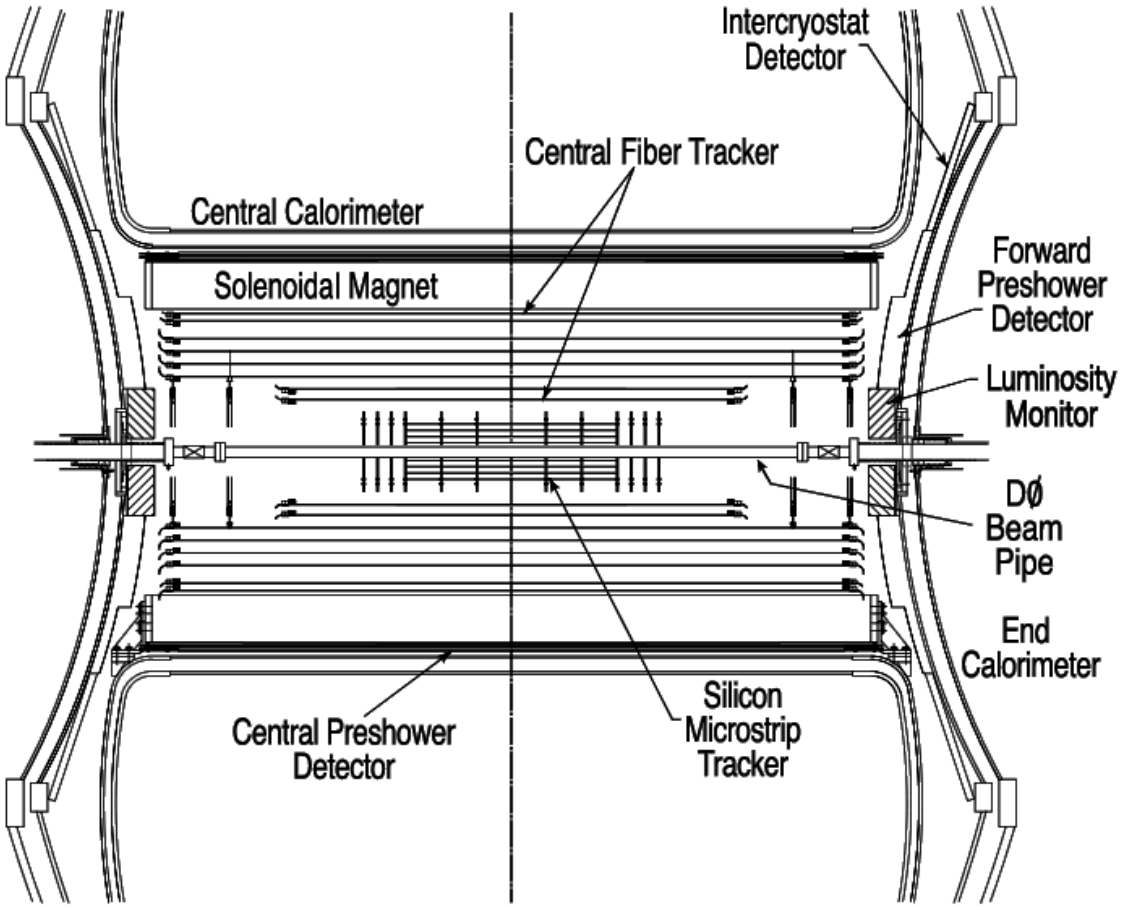

Figure 3.3: The central tracking system for the DØ detector.

the SMT form the central tracking system of the DØ detector, The two tracking detectors locate the primary interaction vertex with a resolution of about 35 μm along the beam line. The CFT system is shown in Figure 3.3.

The calorimeters were designed to provide energy measurements for electrons and photons, and jets in the absence of a central magnetic field (as was the case during the stage that we mentioned before, Run I), as well as assisting in identification of electrons, photons, jets, and muons and measure the missing transverse energy. In the detector there are three calorimeters: one central and two located at the ends as we can see in Figure 3.5.

All those components are immersed in a strong magnetic field provided for two kind of magnets: Solenoidal (superconducting) and Toroidal Magnets. Ffgure 3.6 shows an axial view of the magnetic fields in the DØ detector.

In the central toroid the magnetic field strength is around 1.8T and 1.9T at the end toroids. For the central field of the solenoid we have around 2.0 T. An other improvement in the detector was the new forward muon system, this is to have more coverage in the range of measurements for η. All of the above is a general view of the DØ detector, for more information please refer to [24].

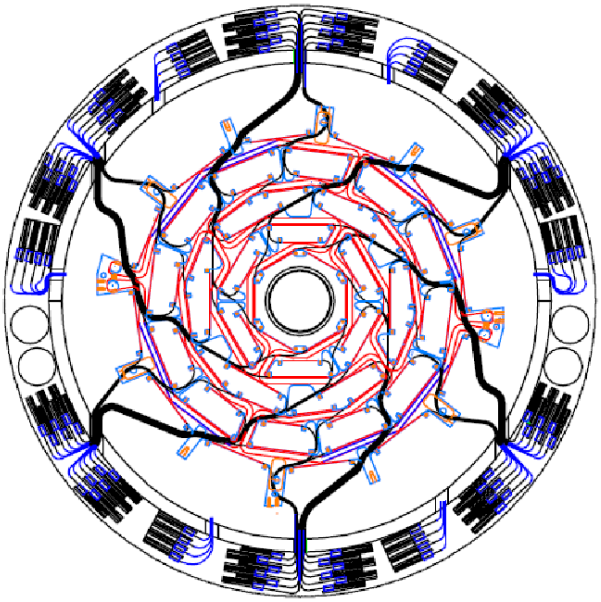

(a) without the L0 modification.

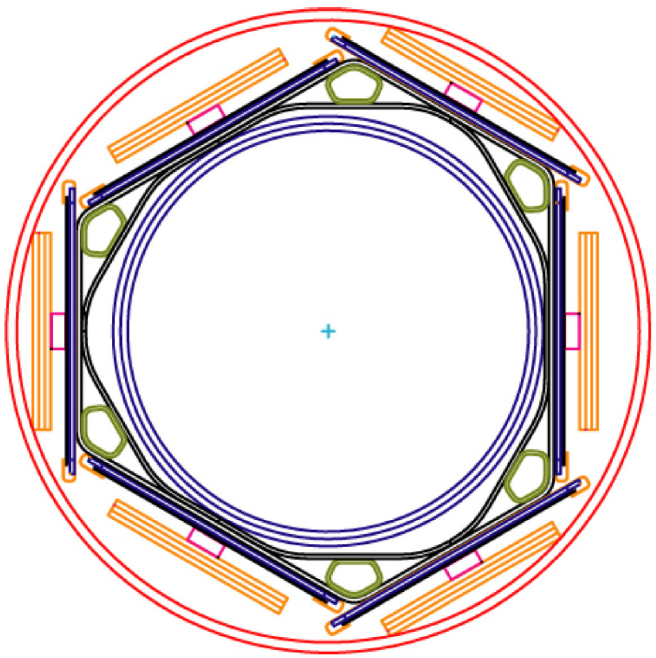

(b) Layer 0

Figure 3.4: The SMT system

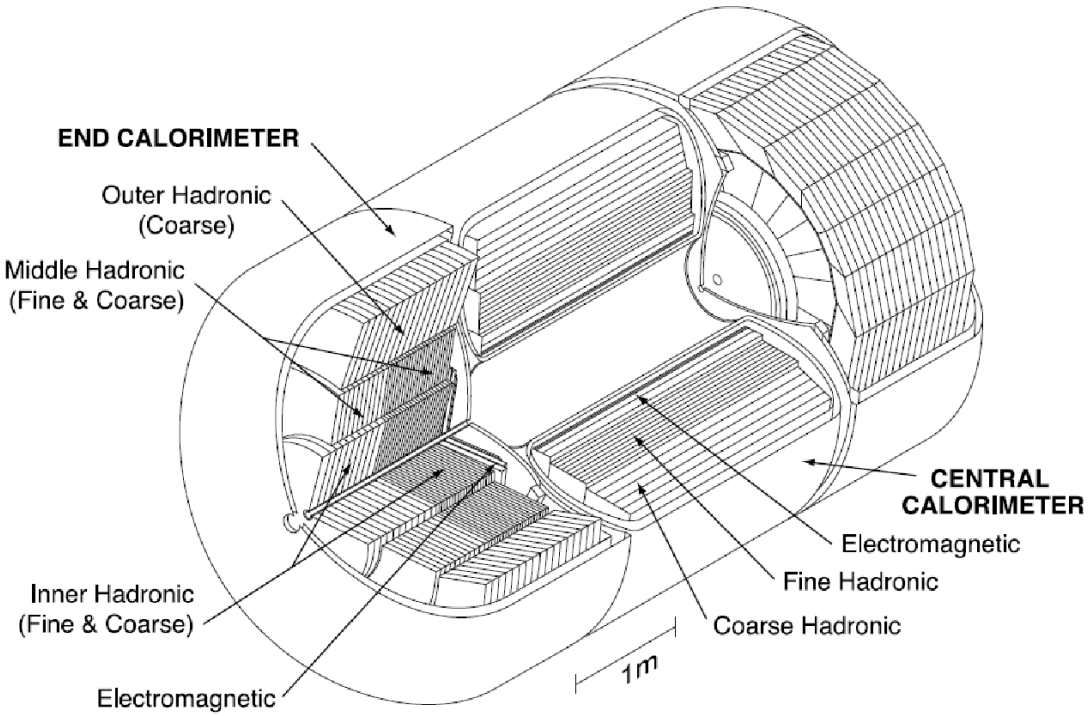

Figure 3.5: Calorimeter

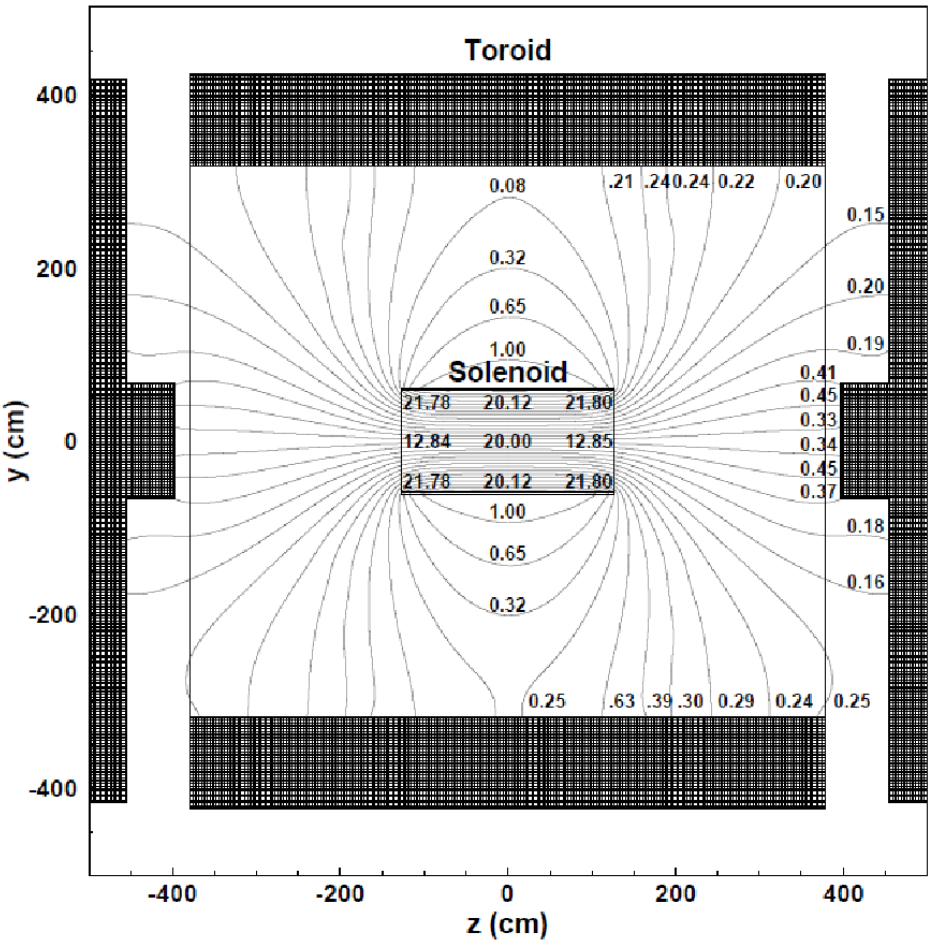

Figure 3.6: Magnetic Fields inside of DØ Detector

Chapter 4

Data and Monte Carlo Samples

4.1 Extended AATrack Reprocessing

The decays of both Ξ_b^- Ω_b^- baryons used in this search include multiple long-lived intermediate states:

$$\Xi_b^- \rightarrow J/\psi\Xi^-; \Xi^- \rightarrow \Lambda^0\pi^-; \Lambda^0 \rightarrow p\pi^- \quad (4.1)$$

$$\Omega_b^- \rightarrow J/\psi\Omega^-; \Omega^- \rightarrow \Lambda^0 K^-; \Lambda^0 \rightarrow p\pi^- \quad (4.2)$$

This decays are illustrated in Figure 4.2. The Ξ^- and Λ^0 baryons have decay lengths ($c\tau$) of around 2.5 cm, and 8 cm, respectively [20]. The charged hadron tracks in the final state can hence be produced with large impact parameters, which would fail the standard DØ track-finding requirements of IP$<$ 2.5 cm. In addition, the hadrons generally have very low momentum, due to the limited phase space available in these decays; again, the standard DØ tracking algorithm is inefficient for such particles. To boost the reconstruction efficiency of these baryon decays, the data are reprocessed, by fixing the thumbnails, allowing a modified tracking algorithm to be used (called Extended AATrack). The details of the new algorithm are outside the scope of this theses, but the main features are a loosening of the thresholds for IP from 2.5 $\rightarrow$ 10 cm (see Table 4.1 and Figure 4.1) and p_T (from 180 (450) MeV $\rightarrow$ 120 MeV for Run IIa (IIb)), enabling tracks with large impact parameter and low momentum to be reconstructed with considerably higher efficiency. The extended AATrack data was used successfully in the prior publication of the Λ_b^0 lifetime [17], which found an increase in the Λ^0 yield of a factor 3 (20) in Run IIa (IIb) with respect to the standard algorithm. Monte Carlo studies of Ξ_b^- events find that the efficiency for reconstructing all five tracks in the final state increases by approximately a factor six, demonstrating the need for this procedure.

For the present analysis, the so-called "2011" version of the Extended AATrack algorithm is used, which includes a bug fix involving track propagation to the DCA (distance of closest approach) [18]. This is the same version as used for the Λ_b^0 lifetime publication, but it differs from the "2007" version used for the original DØ Ξ_b^- and Ω_b^- analyses. The 2007 version was only used for Run IIa data, and was found to be unfeasible for the more

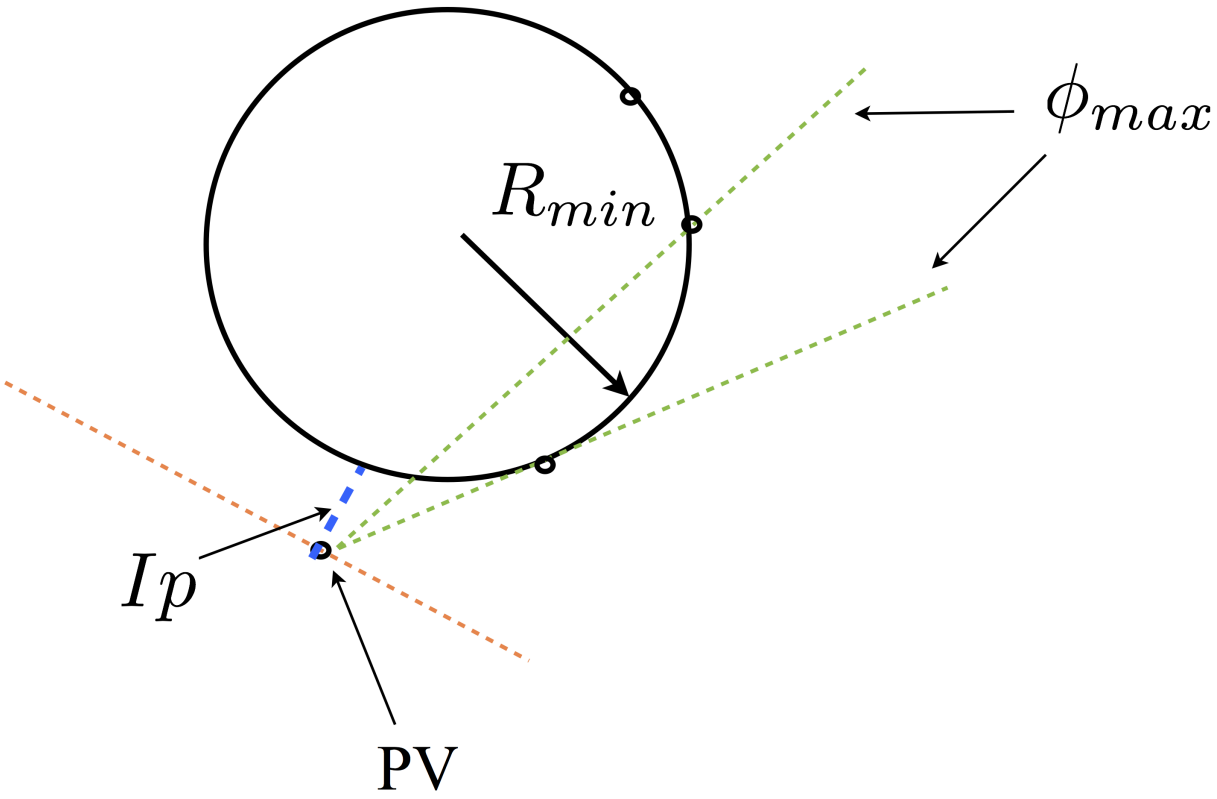

Figure 4.1: Parameters used to accept or reject a track. The standard values of this parameters has being modified for the extended AATrack reprocessing as mentioned in the text.

Parameter	Standard	Extended
ϕ_{max}	0.08	0.20
R_{min}	75 cm	20 cm
Ip	2.5 cm	10 cm

Table 4.1: Parameters for both Standard and Extended AATrack algorithm.

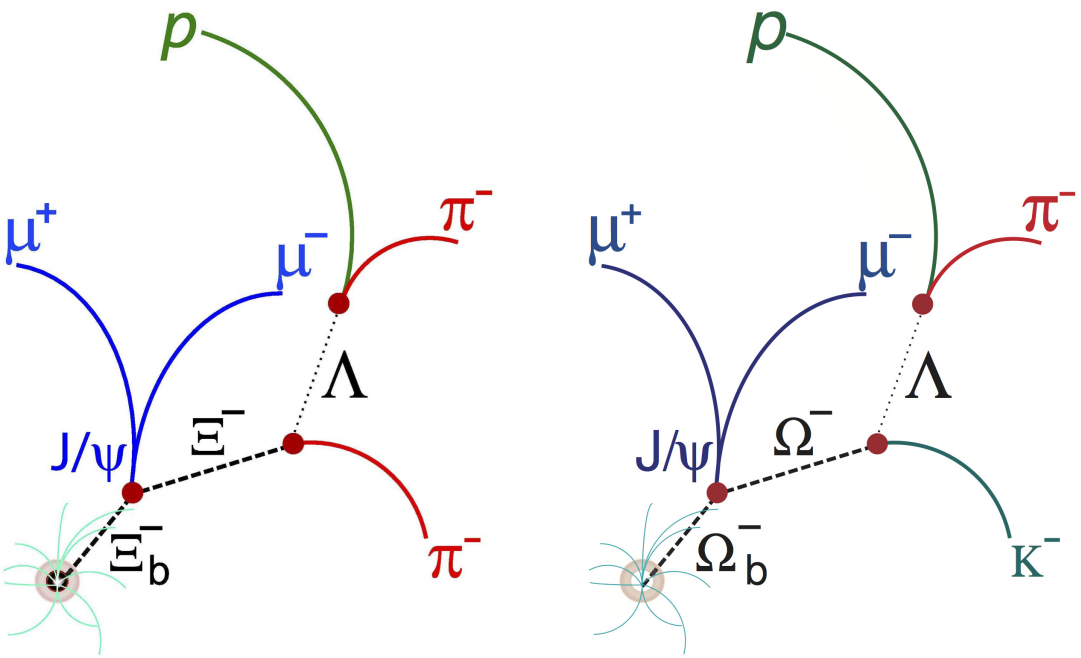

(a) Ξ_b^- decay chain.

(b) Ω_b^- decay chain.

Figure 4.2: Illustration of the sequential decay chains used to reconstruct Ξ_b^- and Ω_b^- baryons. The long-lived intermediate states require that the data be reprocessed with a modified tracking algorithm, as described in the text

complex events found in 10 the higher-luminosity Run IIb data. The 2007 data is used as a cross-check of the Run IIa performance, as described later. For completeness, we note that there was an intermediate version ("2009") which was available for both Run IIa and Run IIb samples, but not used in any publications (and was subsequently found to have introduced the DCA bug which necessitated the 2011 update). The events to be reprocessed with Extended AATrack are selected from a J/ψ skim, as described in Ref. [18]. The 15 requirements are similar to, but looser than, those subsequently applied during preselection, so are not listed here. The SAM dataset definitions for the samples used in this analysis are as follows:

jpsi_extendedAATrack_pass3_RunIIa_p20.18.02_lossless (16,979,843 events)
jpsi_extendedAATrack_pass2_RunIIb1_p20.16.06_lossless (22,543,636 events)
jpsi_extendedAATrack_pass4_RunIIb2_p20.18.02_lossless (59,101,860 events)
jpsi_extendedAATrack_pass5_RunIIb3_p20.18.02_lossless (37,911,199 events)
jpsi_extendedAATrack_pass6_RunIIb4_p20.18.02_lossless (46,472,146 events)

4.2 MC Samples

Monte Carlo simulation (MC) is essential for this analysis, mainly for the training of the multivariate selection discriminant, and to understand the reconstruction and selection efficiencies for different requirements. All samples are generated with pythia version 6.409, interfaced with EvtGen to model the decays of weakly-decaying heavy-flavor particles. As usual, the simulated events are passed through the appropriate geant detector simulator and then through DØgstar to simulate detector noise, pile-up, and other effects.

What is different for these MC samples is that they must be reprocessed using the Extended AATrack algorithm, prior to use, to properly reflect the analysis conditions. This is performed in exactly the same way as for the real data. Samples are generated for both Run IIa and Run IIb conditions; for Run IIb we use the "Run IIb3" version, p20.17.02, 5 that most accurately reflects the Run IIb environment. Both $\Xi_b^\pm \to J/\psi\Xi_b^\pm$ and $\Omega_b^- \to J/\psi\Omega^\pm$ samples are created, where the b baryon decays are enforced 100% of the time, using EvtGen. However, the subsequent decays of $\Xi^\pm$, $\Omega^\pm$ and Λ^0 occur in geant, and their branching ratios cannot be adjusted. The result is that around 50% of generated. MC events have the incorrect decay chain (dominated by $\Lambda^0 \to n\pi^0$), and are not used in the analysis. To properly include all possible b quark production mechanisms, including gluon splitting, the most realistic generation proceeds via generic qq ÌĎ production (i.e. MSEL=1, in pythia language). However, such samples have a very low generation efficiency, and for the Ω_b^- case the large-scale production of MSEL=1 events was found to be impossible. The alternative is to limit the initial state to b ÌĎb (MSEL=5). To evaluate the effect of this simplification, Ξ_b^- samples are generated with both qq ÌĎ and b ÌĎb conditions, allowing the analysis performance to be compared with the two different samples used for BDT training. This comparison has not yet been performed, but will proceed in parallel with the review. The different samples available are as follows:

- $\Xi_b^{\pm} \to J/\psi \Xi^{\pm}$
  - Run IIa, $q\bar{q}$, request IDs 198012-198021, 2M events.
  - Run IIb3, $q\bar{q}$, request IDs 196652-196691, 8M events.
  - Run IIb3, $b\bar{b}$, request IDs 199877-199916, 8M events.
- $\Omega_b^{\pm} \to J/\psi \Omega^{\pm}$
  - Run IIb3, $b\bar{b}$, request IDs 199837-199876, 8M events.

For all these samples, the mass and lifetimes of the b baryons are adjusted from their default pythia values, to best reflect the current experimental status. We set $M(\Xi_b^{\pm}) = 5.790$ GeV, $c\tau(\Xi_b^{\pm}) = 470\mu m$, $M(\Omega_b^{\pm}) = 6.050$ GeV, $c\tau(\Omega_b^{\pm}) = 340\mu m$.

4.2.1 MC *Weighting*

The MC samples do not include the effects of the DØ trigger. To account for this, all simulated events are reweighted to ensure that both the leading (highest p_T) and trailing (lowest p_T) muon have transverse momentum distributions that match the real data. Separate weight functions are applied for Run IIa and Run IIb, and are derived by comparing MC and background-subtracted data for the decay $B^+ \to J/\psi K^+$ [19], as performed in the recent $B_s^0 \to \mu^+\mu^-$ analysis. In addition, a second weighting is applied to the b baryon p_T to account for the fact that this version of pythia tends to generate b hadrons with too soft a momentum spectrum. This function is also taken from Ref. [19].

4.2.2 Matching Generated Particles with Reconstructed Tracks

To ensure that the reconstructed samples of MC events contain pure signal, without contamination from combina- torial background, we require that all five of the reconstructed tracks in the final state be "matched" to the correct generated particles. This is a two-step process. Firstly, the generated particles are each associated with a reconstructed track, by looping over the tracks and finding the one which most closely aligns with the particle properties (location, initial direction, curvature). The match must be reasonable, with a total χ^2 less than 100 units for the comparison, 40 and some particles fail this requirement. Secondly, each track in the reconstructed MC event must correspond exactly with the appropriate particle track as established in step 1. For example, the reconstructed proton track in the Ξ_b^- decay must correspond to the track matched to the generated proton, and so on. Overall, this requirement is around 95% efficient for true signal candidates (i.e. those where the reconstructed object is indeed from the correct generated particle). Since there are five tracks, the overall efficiency for the full 45 decay is of order 75-80% efficient.

Chapter 5

Event Selection

This analysis uses the full Run II data sample, collected by the DØ experiment from 2002-2011. For historical reasons, and due to significant changes to the detector, triggers, and collision environment, we analyse the Run IIa and Run IIb data samples separately; however, we do not subdivide into IIb1, IIb2 etc. In total, the dataset comprises an integrated luminosity of around $10.4 fb^1$, prior to the application of data quality (DQ) requirements. We remove all runs marked as bad by the DQ group for the following sub-systems: muon, SMT, CFT, CTT. No calorimeter information is used in event reconstruction, so runs marked as bad due to calorimeter issues are retained. The DQ requirements remove around 2.5% of the total event sample, at preselection. The analysis uses an inclusive trigger strategy, although the majority of events will satisfy single or dimuon triggers, due to the $J/\psi \to \mu^+\mu^-$ decay. We do not exclude events that may have impact parameter biases from the trigger requirements.

5.1 Preselection

5.1.1 J/ψ reconstruction

Events are considered for selection if they contain two muons, of opposite charge, consistent with originating at a common vertex. The two-muon system must have an invariant mass $2.80 < \mathrm{M}(\mu\mu) < 3.35$ GeV, and is used to reconstruct a $J/\psi \to \mu^+\mu^-$ candidate. The standard **jpsiFinder** tool is used, from the bana analysis package, which applies a number of requirements to improve the J/ψ purity. At least one muon must have reconstructed segments both inside (layer A) and outside (layers BC) the toroid magnet (nseg=3); For the second muon, we allow nseg=0 (no reconstructed segments, but individual hits in the muon system consistent with a muon), nseg=1 (layer-A hit only), and nseg=3 cases, but not nseg=2 (layer-BC hit only). This latter category only accounts for a small fraction (2.5%) of events, and has low purity, since real muons with hits outside the toroid should also be associated with layer-A hits. Both muons must be associated with central tracks, with at least one hit in both the CFT and SMT systems. The χ^2 of the $J/\psi \to \mu\mu$

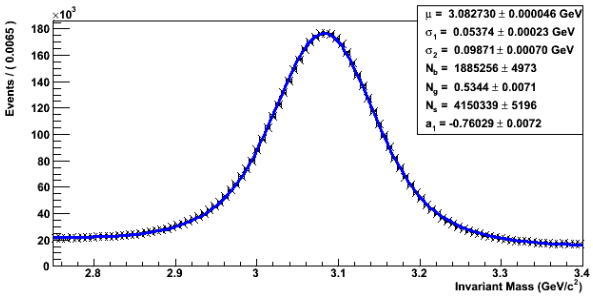

(a) Run IIa.

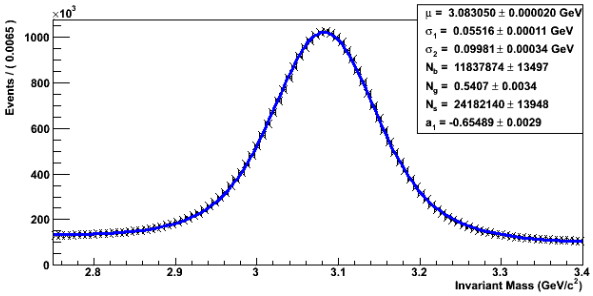

(b) Run IIb.

Figure 5.1: J/ψ mass distributions for Run IIa and IIb, before applying the baryon selection requirements. The yields are extracted from an unbinned maximum likelihood fit to the data, with a double Gaussian signal component, and first order polynomial background. To improve the fit, the mass window has been extended by 50 MeV on either side, relative to the actual analysis requirements.

two-track vertex fit must be less than 36, and we require $p_T(J/\psi) > 3.5$ GeV. Muons with reconstructed segments are required to have $p_T(\mu) > 1.5$ GeV. Muons without segments must fulfill $p_T(\mu) > 1.0$ GeV, but are also subject to additional quality requirements: they must have total momentum below 7 GeV, and the accompanying nseg=3 muon must have $p_T(\mu) > 2.5$ GeV. At this stage, prior to any further reconstruction requirements, there are a total of $4,150,339 \pm 5,196$ J/ψ signal candidates in Run IIa, and $24,182,140 \pm 13,948$ in Run IIb, as determined by fitting the invariant mass of the dimuon system. The distributions and fits are shown in Figure 5.1. These yields are important, because they establish the effective sample size for Run IIb relative to Run IIa, taking into account the evolution of the trigger list. The ratio of yields, $N_{IIb}/N_{IIa} = 5.8$ is somewhat smaller than the ratio of integrated luminosities of the two epochs, $9.1/1.3 = 7.0$, as expected from the effect of tightened prescales for low-pT muon triggers in the later running.

5.1.2 Ξ^- and Ω^- Reconstruction

For events satisfying the J/ψ requirements described above, Ξ^- and Ω^- candidates are reconstructed using the **cascadeFinder** tool in bana. Firstly, $\Lambda^0 \to p\pi$ candidates are formed, by combining pairs of opposite-charge tracks consistent with originating at a common vertex. One track is assigned the charged pion mass, and the other assigned the proton mass. There are two possible combinations for each pair, depending on whether the positively or negatively-charged track is assigned the pion mass: both are allowed at this stage, but only candidates satisfying $1.105 < \mathrm{M}(p\pi) < 1.125$ GeV are retained. In practice, the track with the higher p_T is almost always the proton, as demonstrated using Monte Carlo simulation (and verified independently in the recent Λ_b^0 lifetime analysis [17]); the discrimination offered by this signature is used later in the multivariate discriminant. Finally, we also require $p_T(\Lambda^0) > 0.4$ GeV

For each Λ^0 candidate, a third track is added and used to construct a Ξ^- (Ω^-) baryon candidate. The invariant mass must satisfy $1.308 < M(\Lambda^0\pi) < 1.335$ GeV ($1.662 < M(\Lambda^0 K) < 1.682$ GeV). For signal decays, the pion (kaon) from the Ξ^- (Ω^-) decay (denoted π_Ξ or K_Ω respectively) has the same charge as the pion from the Λ^0 decay: such events are called 'right-sign', and this charge correlation is enforced for our signal sample. The 'wrong-sign' candidates, where these two tracks have opposite charge, are retained in a separate sample which provides useful information for understanding the background behavior. The third track must be consistent with originating at a common vertex with the Λ^0 candidate, and inconsistent ($\chi^2 > 9$) with arising from the primary interaction vertex (PV), to reduce the combinatorial background from prompt tracks. All three tracks in the Ξ^- (Ω^-) decay chain must have at least one CFT hit, but no SMT hit requirements are imposed.

5.1.3 Ξ_b^- and Ω_b^- Reconstruction

The final stage in reconstruction is the combination of the J/ψ and Ξ^- (Ω^-) candidates to form $\Xi_b^- \to J/\psi\Xi^-$ ($\Omega_b^- \to J/\psi\Omega^-$) candidates. This proceeds in a similar manner to the above steps; namely, the two particles must be consistent with arising from a common vertex, and the combined object must have an invariant mass within the expected range, $5.20 < M(\Xi_b^-) < 6.38$ GeV ($5.20 < M(\Omega_b^-) < 7.00$ GeV). In this case, the Ξ_b^- (Ω_b^-) mass is determined using the known mass of the J/ψ meson ($M(J/\psi) = 3.097$ GeV, from the PDG [20]) as a constraint to correct the muon momenta.

At this stage, we apply some additional loose quality requirements to remove badly reconstructed events. The variable $\chi^2_{\mathrm{PV}\to}(X)$ for a particle X gives the chi-square of a fit assuming that the particle originates from the primary interaction vertex. This can be a useful variable when characterizing decays, with small values indicating a particle originated from the PV, and large values indicating it is probably the product of a secondary decay. However, we observe extremely long tails for the distributions of these variables (up to several million units in value), which are likely due to badly reconstructed events (for example, fake tracks, tracks distorted via decay-in-flight, or particles from a different

primary vertex). We exclude candidates which fail any one of the following $\chi^2_{\mathrm{PV}\rightarrow}(X)$ requirements:

$$\chi^2_{\mathrm{PV}\rightarrow}(\mu_{1,2}) < 1000, \quad (5.1)$$
$$\chi^2_{\mathrm{PV}\rightarrow}(\pi, \pi_\Xi, K_\Omega, p) < 85000, \quad (5.2)$$
$$\chi^2_{\mathrm{PV}\rightarrow}(J/\psi, \Xi, \Omega, \Lambda) < 4000, \quad (5.3)$$

where the requirement is applied separately to all particles in parentheses. The maximum values are chosen after inspection of the tails in data. We find that the expected performance in both Run IIa and Run IIb is slightly improved by the removal of these candidates.

Finally, we remove all events that contain in excess of 300 tracks. This empirically-motivated cut was initially tested to examine the difference in the behavior of background at low and high track multiplicities. In fact, we find that for events with fewer than 300 tracks, the Ξ^- signal yield (in data) is almost unchanged, while the background is significantly reduced (especially for Run IIb data). As such, we apply this cut to improve the signal significance. To avoid a large digression here, this cut is discussed in detail in Appendix A.

5.1.4 Preselection Yields and Distributions

At this preselection stage, there are a total of 3 776 (2 138) right-sign (wrong-sign) Ξ_b^- events remaining in the Run IIa signal sample, and 20 405 (15 724) in the Run IIb sample. The Ξ_b^- mass distributions for both epochs are shown in Fig. 5.2, with both right- and wrong-sign distributions plotted. For reference, the signal distributions from MC are also shown, with arbitrary normalization.

The corresponding Ω_b^- sample contains 3 488 (2 951) right-sign (wrong-sign) candidates in the Run IIa sample, and 24 159 (22 428) in the Run IIb sample. The mass distributions for right- and wrong-sign samples, and the MC sample, are shown in Fig. 5.3.

The corresponding Λ^0, Ξ^-, and Ω^- invariant mass distributions are shown in Figs. 5.4–5.5. For the Ξ^- and Ω^- cases, the wrong-sign distributions are also plotted, since they are by construction signal-free, and indicate the shape of the background under the peak. The yields of Λ^0 and Ξ^- signal candidates in the preselection sample are determined by fitting these distributions with an unbinned maximum likelihood method, giving the following numbers:

$$N(\Lambda^0, \text{IIa}) = 2291 \pm 115, \quad (5.4)$$
$$N(\Xi^-, \text{IIa}) = 1592 \pm 69, \quad (5.5)$$
$$N(\Lambda^0, \text{IIb}) = 6334 \pm 186, \quad (5.6)$$
$$N(\Xi^-, \text{IIb}) = 4182 \pm 163. \quad (5.7)$$

All fits use a first order polynomial function to model the background, and a double Gaussian function to model the signal, except for the Run IIb Ξ^- case in which a single Gaussian is found to be sufficient.

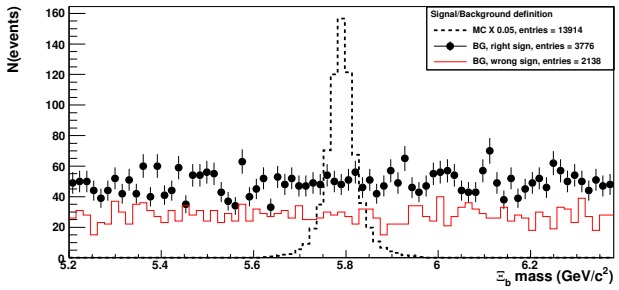

(a) Run IIa.

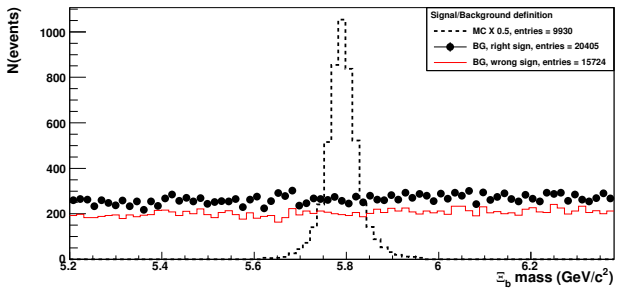

(b) Run IIb.

Figure 5.2: Ξ_b^- invariant mass distributions after preselection requirements have been applied, for right- and wrong-sign data samples, and Monte Carlo signal (with arbitrary normalization). The wrong-sign samples have fewer candidates because they contain no Ξ^- signal component (see Fig. 5.4 for an illustration of this).

For the Ω^- case, no clear signal is visible at the preselection level, due to the small signal purity. To demonstrate the presence of an Ω^- signal, we apply a few cuts, with variables and cut values chosen based on the performance plots from the BDT training (see Section 5.1.6). The applied cuts are $p_T(\Omega^-) > 1.5$ GeV, $ct(\Omega^-) < 5$ cm, Isolation$(\Omega^-)>$ 0.3, and the resulting mass distribution is also shown in Fig. 5.5. Clear peaks are visible for both Run IIa and Run IIb, with yields

$$N(\Omega^-, \text{IIa, with extra cuts}) = 141 \pm 29, \quad (5.8)$$
$$N(\Omega^-, \text{IIb, with extra cuts}) = 254 \pm 46. \quad (5.9)$$

To estimate the total Ω^- yields, without these additional three cuts, we use the MC simulation, and find an efficiency of $(79.8 \pm 0.4)\%$, giving overall yields of

$$N(\Omega^-, \text{IIa}) = 177 \pm 36, \quad (5.10)$$
$$N(\Omega^-, \text{IIb}) = 318 \pm 58. \quad (5.11)$$

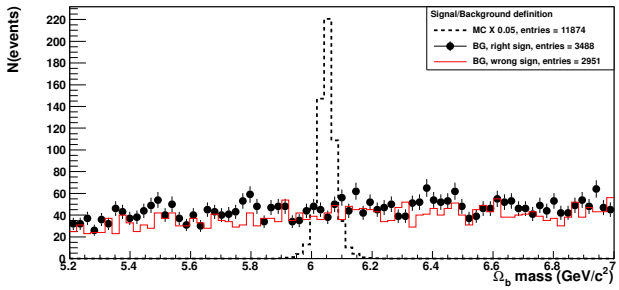

(a) Run IIa.

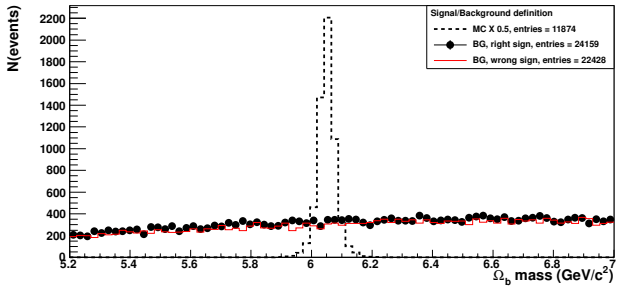

(b) Run IIb.

Figure 5.3: Ω_b^- invariant mass distributions after preselection requirements have been applied, for right- and wrong-sign data samples, and Monte Carlo signal (with arbitrary normalization).

5.1.5 Expected Ξ_b^- and Ω_b^- Signal Yields at Preselection

In order to optimize the search and establish a Ξ_b^- signal, we need some estimate of the number of signal events in the preselection sample. The Ξ_b^- yield will itself give a direct normalization for use in the Ω_b^- search. However, there is no reference channel for the Ξ_b^- case, and so we instead use the existing yield from the published analysis of Run IIa data to give a first estimate of the yield [1].

For the sake of brevity, the full discussion of the Ξ_b^- yield estimate at preselection has been moved to Appendix B. The conclusion is that we must use the data itself to estimate the Run IIa preselection yield, and then extrapolate this to predict the Run IIb yield as follows:

$$\begin{aligned} N(\Xi_b^-, \text{IIa}) &= 15 \pm 5, \\ N(\Xi_b^-, \text{IIb}) &= 25 \pm 9, \\ N(\Xi_b^-, \text{II}) &= 40 \pm 14, \end{aligned} \tag{5.12}$$

where we assume that the uncertainty on the IIa and IIb yields are 100% correlated (since the IIb yield is extrapolated from the IIa yield, which provides the dominant uncertainty).

The actual Run II Ξ_b^- preselection yield in the data is determined by dividing the measured yield after application of the BDT requirement, by the efficiency of the BDT requirement relative to the preselection (obtained from simulation). This is described in Section 5.2. The Ξ_b^- yield after BDT cuts is 27.4 ± 6.6 events, and the BDT efficiency is 0.604 (negligible uncertainty compared to the yield). This procedure gives a measured preselection yield of

$$N(\Xi_b^-, \text{II, observed}) \;=\; 45.4 \pm 10.9, \tag{5.13}$$

where the uncertainty is dominated by the measured yield from the mass fit.

This yield can be used to predict the corresponding Ω_b^- preselection yield. This conversion is reliable because almost all expected detector and reconstruction effects are common to these two topologically identical channels, and so the ratio $N(\Omega_b^-)/N(\Xi_b^-)$ is robust against variations from such effects. The Ω_b^- yield depends on the relative ratio of production rates $\times$ decay branching fractions, and also on the ratio of reconstruction efficiencies for the two channels:

$$N(\Omega_b^-, \text{II}) \;=\; N(\Xi_b^-, \text{II}) \cdot \frac{\sigma(p\bar{p} \to \Omega_b^-) \cdot \mathcal{B}(\Omega_b^- \to J/\psi \Omega^-) \cdot \mathcal{B}(\Omega^- \to \Lambda^0 K^-)}{\sigma(p\bar{p} \to \Xi_b^-) \cdot \mathcal{B}(\Xi_b^- \to J/\psi \Xi^-) \cdot \mathcal{B}(\Xi^- \to \Lambda^0 \pi^-)} \cdot \frac{\varepsilon(\Omega_b^-)}{\varepsilon(\Xi_b^-)} \tag{5.14}$$

The first term is the Ξ_b^- yield of 45.4 ± 10.9. The final term is the ratio of selection efficiencies determined from Monte Carlo simulation. The Ω^- has a proper lifetime around half the size of the Ξ^- (2.5 cm versus 5 cm), so the decays are more likely to reside within the SMT, giving an increased reconstruction efficiency. The Q-values for the two b baryon decays are very close (since in both cases the decays are driven by $b \to c$ transitions) and any residual variations in trigger efficiency from differences in the J/ψ kinematics are neglected. The efficiency ratio determined from Monte Carlo is $\varepsilon(\Omega_b^-)/\varepsilon(\Xi_b^-) = (4\,023/918\,215)/(9\,954/3\,931\,532) = 1.73 \pm 0.03$, where the numerator in each set of parentheses is the number of signal candidates reconstructed at the preselection level, and the denominator is the total number of signal candidates generated.

The second term in Eq. (5.14) is the relative ratio of production rates $\times$ decay branching fractions for the two channels. This has been measured by both CDF [15] and DØ [14], as described in Section 6.1. The CDF measurement is 0.27 ± 0.12, the DØ measurement is $0.80^{+0.35}_{-0.39}$; a weighted average yields a ratio 0.32 ± 0.11, with the two measurements having a χ^2 of 1.69 for one degree of freedom. Hence they are in reasonable agreement, despite the factor of three difference, due to the rather large uncertainties.

Using the CDF ratio, the expected Ω_b^- preselection yield is 21.2 ± 10.7. Using the DØ ratio, the corresponding preselection yield is 62.8 ± 34.2 events. Since these numbers are only used in choosing the optimal BDT cut for the Ω_b^- search, we estimate the sensitivity of the search performance to the input value of the preselection signal yield. This is done by separately optimizing the BDT for both possible values of the preselection yield, and examining the difference in the significance distribution versus BDT output for the two cases. In fact the signal significance for both options is found to be maximal in the same range of BDT requirements, as described later. Hence the final Ω_b^- search performance is largely insensitive to the assumptions about the relative abundances of the two decays.

5.1.6 Multivariate Discriminant

The preselection is designed to be as efficient as possible, with the main signal losses coming from irreducible tracking inefficiencies and muon identification requirements. To give the best possible signal significance in the final analysis, we make use of multivariate selection techniques using the Toolkit for Multivariate Analysis (TMVA) package [21].

We test a number of different discriminants, covering the built-in options in TMVA, and choose the BDT (boosted decision tree) algorithm, which consistently gives the best performance.

The overall approach is to develop and test the multivariate discriminant using the Ξ_b^- channel, and then once the final decisions have been made (e.g. choice of input variables) to convert into an Ω_b^- search with minimal changes.

5.1.7 Signal and Background Samples

In order to train the MVA discriminant, we require representative event samples for both signal and background. We find that the best performance (in terms of background rejection versus signal efficiency) is achieved by training a single discriminant for Run IIa and Run IIb samples.

For the Ξ_b^- case, we use the Run IIb $q\bar{q} \to \Xi_b^-$ Monte Carlo as a signal model (as described in Section 4.2) including full matching. For background we use the Run IIb data, combining the wrong-sign sample and the right-sign sample in the sideband regions ($5.200 < M(\Xi_b^-) < 5.615$ GeV or $5.965 < M(\Xi_b^-) < 6.380$ GeV).

In preliminary tests, we investigated the possibility of training a separate Run IIa discriminant. However, the training samples were found to be too small, especially the for background model, and the discriminant suffered from severe overtraining and poor performance. Using the 'IIb-trained' discriminant described above gave significantly better performance. Similarly, we tried training using only the sideband data for background, but the addition of the wrong-sign sample gave a noticeable improvement.

For the Ω_b^- case, we use the Run IIb $b\bar{b} \to \Omega_b^-$ Monte Carlo as a signal model, since the corresponding generic $q\bar{q}$ production process has too small an efficiency to be generated reliably. For background we use the Run IIb data, combining the wrong-sign sample and the right-sign sample in the sideband regions ($5.350 < M(\Omega_b^-) < 5.875$ GeV or $6.225 < M(\Omega_b^-) < 6.750$ GeV).

5.1.8 Choice of Input Variables

The b baryon decays investigated are rich in their topology, containing five final-state charged particles, and three intermediate states, two of which are long-lived. As such, there are a large number of possible variables that can help discriminate signal and background events. On the other hand, it is desirable to avoid using more variables than are needed, since this can lead to issues with the BDT training, and gives more opportunity for mismodelling of variables to negatively impact the performance.

This section first describes the development of the BDT discriminant for the Ξ_b^- channel. The BDT for Ω_b^- will then use the same technique, with training samples and variables suitably redefined to account for the different particles in the decay.

The set of Ξ_b^- input variables considered can be separated into the following categories.

- Particle transverse momenta (9 variables):
  $p_T(\Xi_b^-)$, $p_T(\Xi^-)$, $p_T(\Lambda^0)$, $p_T(J/\psi)$, $p_T(\pi_\Xi)$, $p_T(\pi_\Lambda)$, $p_T(p)$, $p_T(\mu_1)$, $p_T(\mu_2)$.

- Isolation variables (9 variables). The isolation I of a particle X is defined as $I(X) = p_T(X)/[\sum_t^{dR<0.5} p_T(t)]$ where t are all reconstructed tracks within a cone of solid angle $dR = \sqrt{d\eta^2 + d\phi^2} = 0.5$ of the particle X:
  $I(\Xi_b^-)$, $I(\Xi^-)$, $I(\Lambda^0)$, $I(J/\psi)$, $I(\pi_\Xi)$, $I(\pi_\Lambda)$, $I(p)$, $I(\mu_1)$, $I(\mu_2)$.

- Cosine of pointing angles (3 variables). For any long-lived particle, the transverse pointing angle θ is defined as the angle between the momentum vector and the displacement vector (i.e. the vector pointing from the production vertex to the decay vertex), projected onto the transverse plane:
  $\cos(\theta_{\Xi_b^-})$, $\cos(\theta_{\Xi^-})$, $\cos(\theta_{\Lambda^0})$.

- Goodness of the vertex fit (χ^2_V) for intermediate particles (4 variables):
  $\chi^2_V(\Xi_b^-)$, $\chi^2_V(\Xi^-)$, $\chi^2_V(\Lambda^0)$, $\chi^2_V(J/\psi)$.

- Lifetime variables for intermediate states (8 variables): transverse decay length L_{xy}, and significance $L_{xy}^{\rm sig} = L_{xy}/\sigma(L_{xy})$; Lifetime $\tau = L_{xy} \cdot M/p_T$, and significance $\tau^{\rm sig} = \tau/\sigma(\tau)$:
  $L_{xy}(\Xi^-)$, $L_{xy}^{\rm sig}(\Xi^-)$, $\tau(\Xi^-)$, $\tau^{\rm sig}(\Xi^-)$, $L_{xy}(\Lambda^0)$, $L_{xy}^{\rm sig}(\Lambda^0)$, $\tau(\Lambda^0)$, $\tau^{\rm sig}(\Lambda^0)$.

- Transverse impact parameter (IP) significance (i.e IP divided by the uncertainty) (8 variables):
  $\mathrm{IP}^{\rm sig}(\Xi^-)$, $\mathrm{IP}^{\rm sig}(\Lambda^0)$, $\mathrm{IP}^{\rm sig}(J/\psi)$, $\mathrm{IP}^{\rm sig}(\pi_\Xi)$, $\mathrm{IP}^{\rm sig}(\pi_\Lambda)$, $\mathrm{IP}^{\rm sig}(p)$, $\mathrm{IP}^{\rm sig}(\mu_1)$, $\mathrm{IP}^{\rm sig}(\mu_2)$.

- The consistency of particles with originating from the PV, $\chi^2_{\rm PV\to}$, (8 variables):
  $\chi^2_{\rm PV\to}(\Xi^-)$, $\chi^2_{\rm PV\to}(\Lambda^0)$, $\chi^2_{\rm PV\to}(J/\psi)$, $\chi^2_{\rm PV\to}(\pi_\Xi)$, $\chi^2_{\rm PV\to}(\pi_\Lambda)$, $\chi^2_{\rm PV\to}(p)$, $\chi^2_{\rm PV\to}(\mu_1)$, $\chi^2_{\rm PV\to}(\mu_2)$.

- Intermediate masses (2 variables): $M(\Xi^-)$, $M(\Lambda^0)$.

- Ratio of transverse momenta of proton and pion from Λ^0 decay (1 variable):
  $p_T(p)/p_T(\pi)$.

Here μ_1 and μ_2 are defined respectively as the highest and lowest p_T muons from the J/ψ decay. While none of these variables are directly related to the Ξ_b^- lifetime, several of them are correlated to this variable; in particular, the impact parameter (and $\chi^2_{\rm PV\to}$) of the muons and Ξ^-, and the pointing angle of the Ξ_b^- baryon. If this same selection is used to perform the lifetime analysis, the effect of including such variables in the discriminant will be evaluated with Monte Carlo, and a correction factor applied to the lifetime measurement, if needed.

We start with the full list of 52 variables listed above. We perform the BDT training, and determine the maximum expected Ξ_b^- signal significance for this 52-variable case. To better estimate the optimal cut point, we redefine the significance to be SIG$'$ = $S/\sqrt{(S+B/2)}$, where the factor 1/2 in the expected background accounts for the fact that our signal region is very wide ($\pm 5\sigma$) and the true significance from the mass fit will effectively only be exposed to half the background. This is an approximation, but we find that reasonable alternatives do not significantly impact the choice of best BDT cut. We then remove the ten variables ranked lowest by the BDT training, and repeat the training and evaluation of maximum expected signal significance. This method is repeated for 52, 42, 32, and 22 input variables. The results are reported in Table 5.1, which shows the expected number of signal events S, the number of background B expected in the signal region, and the corresponding metric SIG$'$, at the maximum value of this significance. For this study, the signal preselection yields of 15 and 25 events are assumed, for Run IIa and Run IIb respectively. The expected background yields in the signal region at preselection are determined by integrating the background fit model within the $\pm 5\sigma$ signal region, yielding 1029 (5489) preselection background events in Run IIa (Run IIb).

N(variables)	Run IIa			
	$\mathrm{BDT}_{\mathrm{min}}$	S	B	$S/\sqrt{(S+B/2)}$
52	0.100	11	18	2.46
42	0.130	10	12	2.50
32	0.130	9	10	2.41
22	0.160	6	11	1.77

N(variables)	Run IIb			
	$\mathrm{BDT}_{\mathrm{min}}$	S	B	$S/\sqrt{(S+B/2)}$
52	0.110	17	13	3.51
42	0.130	15	7	3.49
32	0.120	14	11	3.17
22	0.140	10	20	2.24

Table 5.1: Comparison of Ξ_b^- BDT performance using different numbers of input variables, using the procedure defined in the text. For each epoch, $\mathrm{BDT}_{\mathrm{min}}$ is the optimal cut value for the BDT output discriminant, S and B are the expected signal and background yields after applying this cut, and $S/\sqrt{(S+B/2)}$ is the corresponding maximal significance.

As can be seen from Table 5.1, the performance is fairly stable versus the number of variables (except for the 22 variable case), degrading slightly as variables are removed. We choose the 42 variable BDT, denoted $\mathrm{BDT}^{42}_{\Xi_b}$, as a compromise between the best

performance and the convenience of fewer variables.

This same list of variables is then used to train the Ω_b^- BDT, with suitable redefinitions (e.g. $p_T(\Xi^-) \to p_T(\Omega^-)$), and the final output of the discriminant is denoted $\mathrm{BDT}^{42}_{\Omega_b}$. The performance for both channels is described in the next section.

5.1.9 BDT Performance for both Channels

The distributions of the Ξ_b^- and Ω_b^- BDT^{42} output for signal and background, are shown in Fig. 5.6, for the Run IIb samples. The consistency of the distributions for the training and testing sub-samples indicates that any possible overtraining effects are small.

Also shown in Fig. 5.6 are the performance curves of the discriminants, in terms of background rejection $(1 - \varepsilon_{\mathrm{BG}})$ and signal efficiency $\varepsilon_{\mathrm{sig}}$. As expected from the distinctive decay signature, excellent rejection can be obtained (99.8%) while retaining a relatively high signal efficiency ($\sim$65% for the Ξ_b^-, $\sim$80% for the Ω_b^-).

The individual distributions of signal and background events for the 42 input variables, for both channels, are given in Appendix C. Also shown is the ranking of these variables for the Ξ_b^- case. The correlations between variables, for both signal and background samples, and for both channels, are shown in Appendix D.

5.1.10 Optimal BDT Requirements

We choose the minimum BDT^{42} requirement to be the value that maximizes the expected signal significance. Figure 5.7 shows the expected signal and background yields, and this significance, as a function of the BDT^{42} cut, zoomed into the region of interest. For the Ξ_b^- case we examine Run IIa and Run IIb separately, and find that the same optimal cut $\mathrm{BDT}^{42}_{\Xi_b} > 0.130$ is optimal for both. For convenience, we here repeat the signal and background preselection yields used in generating these scans:

$$\begin{aligned} N(\Xi_b^-,\,\mathrm{IIa}) &= 15, \\ N(\Xi_b^-,\,\mathrm{IIb}) &= 25, \\ N(\mathrm{BG},\,\mathrm{IIa}) &= 1029, \\ N(\mathrm{BG},\,\mathrm{IIb}) &= 5489, \end{aligned} \tag{5.15}$$

where the background counts here correspond to the expectations for the full $\pm 5\sigma$ signal region. The expected background yields at the final $\mathrm{BDT}^{42}_{\Xi_b} > 0.130$ cut are 12 (7) for Run IIa (IIb). The corresponding expected signal yields after the BDT cut are 9.0 (15.1) for Run IIa (IIb). For the Full Run II sample, this corresponds to a signal efficiency of 60.3%, and a background efficiency of 0.29%.

For the Ω_b^- BDT, we find the optimal cut for the two possible assumptions of the preselection yield (discussed in Section 5.1.5), i.e. either 21.2 or 62.8 Ω_b^- signal candidates at preselection. Figure 5.7 shows the two significance scans, illustrating the lack of sensitivity to the input preselection yield - we choose a cut $\mathrm{BDT}^{42}_{\Omega_b} > 0.100$, which is near optimal for

both cases, and hence relatively robust against the input assumptions. The corresponding expected preselection background yields in the relevant mass region are

$$\begin{aligned} N(\text{BG, IIa}) &= 390, \\ N(\text{BG, IIb}) &= 2544, \end{aligned} \tag{5.16}$$

where these counts here correspond to a narrower mass range $\pm 3\sigma$. The chosen width of the region used to define the background yields doesn't affect the optimal BDT cut from the scan (for an illustration, compare the two significance curves for the upper plots in Fig. 5.7, which use different mass ranges).

After the final cut $\text{BDT}^{42}_{\Omega_b} > 0.130$, the expected background yield in the $\pm 3\sigma$ region is 12 events (5 for Run IIa, 7 for Run IIb). The corresponding background yields in the full blinded region ($\pm 5\sigma$) are 7.6 for Run IIa, 10.7 for Run IIb, and 18.3 for the full Run II sample. The signal yields after the BDT cut, for the full Run II sample, are 16.5 (48.7) when assuming the CDF (DØ) ratio $f_{\Omega_b/\Xi_b} = 0.27(0.80)$. The expected yields for Run IIa and IIb are given separately in Eq. (5.21). For the Full Run II sample, the performance corresponds to a signal efficiency of 77.6%, and a background efficiency of 0.41%.

5.2 Ξ_b^- Results

5.2.1 Ξ_b^- Run IIa Results

The Run IIa invariant mass distribution $M(\Xi_b^-)$, after application of the BDT requirement ($\text{BDT}^{42}_{\Xi_b} > 0.130$), is shown in Fig. 5.8. We expect 9 signal events and 12 background events, for a total of 21; on unblinding the signal region we observe 20 events. The distribution is fitted using an unbinned maximum likelihood fit, to the sum of a double Gaussian signal model, and an exponential background model. This fit determines the Ξ_b^- signal yield to be 5.1 ± 3.5, reasonably consistent with, but lower than, the expected yield. The shape parameters of the signal peak (i.e. the two widths, and their relative contributions to the overall normalization) are fixed from those obtained from simulation, with exactly the same cuts applied. Figure 5.8 also shows this fit to the MC, which finds

$$\begin{aligned} \sigma_1(\text{IIa}) &= 62.1 \pm 2.0 \text{ MeV}, \\ \sigma_2(\text{IIa}) &= 23.7 \pm 0.6 \text{ MeV}, \\ f_1(\text{IIa}) &= 0.312 \pm 0.023, \end{aligned} \tag{5.17}$$

where f_1 s the fraction of the signal model in the Gaussian with width σ_1. The invariant mass of the Ξ_b^- is measured to be 5.782 ± 0.045 (stat.) GeV, which is consistent with the existing measurements, as summarized in Table 1.1, albeit with a large uncertainty.

For now, we use the log likelihood ratio method to estimate the signal significance of the Ξ_b^- peak, by comparing the total likelihood with and without the signal included in the fit, and taking into account the reduction in the number of degress of freedom for the latter fit. This method gives a significance of 1.8σ.

5.2.2 Ξ_b^- Run IIb Results

The Ξ_b^- mass distributions for Run IIb are also shown in Fig. 5.8. After requiring $\mathrm{BDT}^{42}_{\Xi_b} > 0.130$, we expect 15 signal events and 7 background events, and observe a total of 38 events. The data are fitted using the same approach as for Run IIa, using a double Gaussian plus exponential model, with the signal parameters fixed from the MC fit to the following values

$$\begin{aligned} \sigma_1(\mathrm{IIb}) &= 61.7 \pm 1.8 \text{ MeV}, \\ \sigma_2(\mathrm{IIb}) &= 23.4 \pm 0.7 \text{ MeV}, \\ f_1(\mathrm{IIb}) &= 0.346 \pm 0.025, \end{aligned} \tag{5.18}$$

From the fit, we obtain a signal yield of 22.4 ± 5.7 events, meaning that the observed background is 15.6 ± 5.7. As such, both the signal and background are above the expectations, each by between one and two standard deviations. The Ξ_b^- mass is measured to be 5.813 ± 0.009 (stat.) GeV, slightly above the world-average value. The statistical significance of the peak is 6.1σ, established from the log-likelihood ratio of fitting hypotheses with and without the signal.

5.2.3 Ξ_b^- Combined Run II Results

We combine the data samples for the Run IIa and IIb epochs, following the BDT selection, and refit the distribution to extract the total Run II results. The signal shape is again set from Monte Carlo, by combining Run IIa and Run IIb MC samples in the same proportion as the signal yields observed in data (i.e. 1 Run IIa event for every 5.1/22.4 Run IIb events). In fact, the proportions of Run IIa and IIb simulated samples are not important, since the shape parameters from each epoch are found to be consistent, as shown in Eqs. (5.17–5.18).

Figure 5.9 shows the full Run II $M(\Xi_b^-)$ distribution, along with the results of the unbinned likelihood fit. For this sample, we expect 24 signal and 19 background events, and observe 27.4 ± 6.6 signal events, and $58 - 27.4 = 30.6 \pm 6.6$ background events. The signal significance of the peak is 5.9σ, meaning that the Run IIb significance is slightly lowered by the addition of the Run IIa data. The mass of the Ξ_b^- baryon is measured to be 5.813 ± 0.010 (stat.) GeV.

5.3 Ω_b^- Results

For the Full Run II sample, we expect 18.3 background events in the signal region, and a signal yield of 16 ± 8 (using the lower CDF ratio $f_{\Omega_b/\Xi_b} = 0.27$) or 49 ± 27 (using the higher DØ value of $f_{\Omega_b/\Xi_b} = 0.80$), for a total expected yield of 34 (67) events. A total of 36 events are observed in the signal region upon unblinding. This is consistent with the expectations of 34 events using the CDF value of f_{Ω_b/Ξ_b}.

The invariant mass distribution for the Ω_b^- channel is shown in Fig. 5.10 for the full Run II sample, after applying the final cut $\mathrm{BDT}^{42}_{\Omega_b} > 0.100$. The corresponding distribution for

the simulated sample (after application of the same BDT cut) is also shown in Fig. 5.10; this is fitted to a double Gaussian function to fix the signal shape parameters that will be used in the fit to the data, following unblinding. These parameters are as follows:

$$\begin{aligned} \sigma_1 &= 47.6 \pm 1.6 \text{ MeV}, \\ \sigma_2 &= 20.4 \pm 0.6 \text{ MeV}, \\ f_1 &= 0.289 \pm 0.028. \end{aligned} \tag{5.19}$$

We fit the data using the same method as for the Ξ_b^- case, i.e., an unbinned maximum likelihood fit, using a double Gaussian signal model and an exponential background shape. The fit finds the following signal parameters:

$$\begin{aligned} N^{\text{observed}}(\Omega_b^-, \text{ Run II}) &= 12.6 \pm 4.6 \text{ events}, \\ M^{\text{observed}}(\Omega_b^-, \text{ Run II}) &= 6129 \pm 13 \text{ MeV}. \end{aligned} \tag{5.20}$$

While the yield is within the expected range, the mass is significantly higher (around 80 MeV) than the values reported by CDF and LHCb, but lower than the published DØ value by 36 MeV (see Table 1.1). As such, it is difficult to justify interpreting the peak as a true signal, rather it looks like an upward fluctuation of the background.

Taking the ratio of fit likelihoods with and without the signal component, we evaluate the statistical significance of the peak to be 3.7σ. The likelihood profile versus mass is shown in Fig. 5.10.

5.3.1 Separate Run IIa and Run IIb Ω_b^- Results

The estimate of the Ω_b^- signal yield at preselection is made assuming that the ratio of reconstruction efficiencies for the two channels (measured in simulation) is the same for all epochs. To first order this is expected to be the case, due to the topologically similar decays. Any higher order effects will be negligible compared to the large relative uncertainties on the expected yield, driven by the precision of the Ξ_b^- yield and the ratio f_{Ω_b/Ξ_b}.

On this basis, we repeat the calculation of Eq. (5.14) separately for Run IIa (using the observed Ξ_b^- yield of 5.1 ± 3.5) and Run IIb (using the observed Ξ_b^- yield of 22.4 ± 5.7). The expected signal yields for the two epochs are then as follows

$$\begin{aligned} N(\Omega_b^-, \text{ IIa}, f_{\Omega_b/\Xi_b} = 0.27) &= 3.1 \pm 2.5, \\ N(\Omega_b^-, \text{ IIb}, f_{\Omega_b/\Xi_b} = 0.27) &= 13.4 \pm 6.9, \end{aligned} \tag{5.21}$$

with the corresponding expected background yields in the blinded signal region determined to be

$$\begin{aligned} N(\text{BG, IIa}) &= 7.6, \\ N(\text{BG, IIb}) &= 10.7. \end{aligned} \tag{5.22}$$

The final mass distributions for the two epochs are shown in Fig. 5.11. For Run IIa, the signal region contains a total of 16 events (10 expected), with the fit reporting the following values:

$$\begin{aligned} N^{\text{observed}}(\Omega_b^-, \text{ Run IIa}) &= 7.4 \pm 3.4 \text{ events}, \\ M^{\text{observed}}(\Omega_b^-, \text{ Run IIa}) &= 6128 \pm 15 \text{ MeV}. \end{aligned} \tag{5.23}$$

This sub-sample is clearly driving the significance of the peak for the full Run II sample. The yields are within expectations, but the reported mass is again too high to interpret the peak as due to a genuine Ω_b^- signal. The peak significance is evaluated to be 3.1σ.

For Run IIb, the signal region contains a total of 20 events (24 expected), with the fit results as follows:

$$\begin{aligned} N^{\text{observed}}(\Omega_b^-, \text{ Run IIb}) &= 5.6 \pm 3.3 \text{ events}, \\ M^{\text{observed}}(\Omega_b^-, \text{ Run IIb}) &= 6135 \pm 25 \text{ MeV}. \end{aligned} \tag{5.24}$$

In this case, the likelihood ratio gives a statistical significance of 2.3σ. The likelihood profiles versus the peak mass parameter are shown in Fig. 5.12, and the results are summarized in Table 5.2.

	Run IIa	Run IIb	Run II
$N^{\text{exp}}(\text{sig})$	3.1 ± 2.5	13.4 ± 6.9	16 ± 8
$N^{\text{obs}}(\text{sig})$	7.4 ± 3.4	5.6 ± 3.3	12.6 ± 4.6
$M^{\text{obs}}(\Omega_b^-)$ (MeV)	6128 ± 15	6135 ± 25	6129 ± 13

Table 5.2: Summary of the Ω_b^- results in Run IIa, IIb, and the full Run II sample. The expectations are based on the CDF measurement of the production rate times branching fraction ratio for the Xi_b^- and Ω_b^- baryons.

5.4 Cross-Checks

5.4.1 Ξ_b^- Mass Dependence of BDT

One concern when using multivariate analyses is the possibility that the final discriminant has some dependence on the variables of interest in the measurement: in this case the Ξ_b^- and Ω_b^- masses are particularly important. The background sample in the BDT training uses sidebands for the correct-sign candidates, and so may preferentially reject events in these sideband regions, giving an effective background enhancement in the signal region that could be be interpreted as a signal.

Any possible BDT discriminant dependence on the mass must originate from an underlying correlation between the input variables and the mass. We measure all 42 of these

correlation coefficients for the Ξ_b^- channel, for both signal and background samples, and find that their magnitudes are all less than 7%, excepting a physically meaningful correlation of 11% between $M(\Xi^-)$ and $M(\Xi_b^-)$ for signal candidates. This information is tabulated in Appendix E.

As an independent cross-check of the mass-dependence of the BDT for background events, we scan over a range of BDT cuts for the Ξ_b^- channel, and examine the $M(\Xi_b^-)$ distribution for the wrong-sign events as the BDT cut is tightened. The results are shown in Appendix F, and do not indicate any significant peaking behavior in the signal region, just gradual smooth variations of the overall background shape.

5.4.2 BDT Performance

In choosing from the various BDT options (i.e. 52, 42, 32, or 22 variable versions), we were guided mainly by the expected signal and background yields, in order to maximize the expected significance. However, there are other unbiased metrics that can also be used to guide this choice, once the signal has been established. In particular, one can examine the expected and observed yields as a function of the BDT cut, to assess how well the performance of the BDT matches the expectations, and hence how well the input variables are modelled by the training samples.

Figure 5.13 shows this scan over Run IIb data for the BDT[42] discriminant, for both the signal yield and the total yield. There is a clear systematic underestimation of the expected signal yield, by up to 10–20 events for the loosest cuts. The total yield is even higher above expectations, indicating that the background yield in the signal region is also systematically larger than expected from extrapolation of the sidebands.

Ultimately, once the Ω_b^- channel is unblinded, we will repeat this cross-check in that channel, and also for the ratio of yields in the two channels, which should benefit from the cancelation of many possible detector and reconstruction effects and give better agreement between the expected and observed BDT dependence.

5.4.3 Comparison with Previous DØ Ω_b^- Result

Having unblinded the data, we can compare the outcome from the new Ω_b^- analysis of Run IIa data with the previous published measurement (denoted as 'PRL2008'). There are several changes between the two analyses. A different version of the extended tracking algorithm was used in the two cases; data quality cuts are applied in the new analysis, but were not in place for PRL2008; the preselection requirements are similar, but the new analysis places slightly tighter mass window constraints on the intermediate particles with respect to PRL2008; finally, a different BDT approach is used, using different training samples, a different list of variables, and different optimisation methods.

The PRL2008 analysis selected a total of 78 events after all requirements. Of these, 32 events are not even present in the data sample after the new extended tracking algorithm is applied. Of the remaining 46 events, just one fails the preselection requirements, while

11/45 of the preselected events fail the data quality requirements, and just 7/34 of these pass the BDT cut.

These results are summarised in Tables 3–4 in Appendix| H. The former lists the 71/78 events from PRL2008 that fail the final requirements of the new analysis, showing at which stage of the selection chain they fail (the order is: BANA, preselection, data quality, BDT). The second table shows the 34 PRL2008 events that pass the quality requirements, and shows the BDT output value of each candidate from the new analysis (the final selection criterion is BDT$>$ 0.100). The seven events passing this BDT requirement are shown in blue.

Table 4 also shows information on the reconstructed Ω_b^- masses, from both PRL2008 and the new analysis, and their difference. Note that this is just a comparison of the event numbers - the specific tracks used to build the b baryon candidates may differ between the two analyses, since the track reconstruction has been re-performed. The shifts are typically of order 20 MeV between the two versions, with some outlisers having even larger differences. For scale, the mass resolution is around 30 MeV for this channel. This is more easily interpreted as a plot, shown in Fig. 5.14, where the masses of the 78 PRL2008 events (green triangles) are compared with the new masses for the common 46 events in the sample (black circles). The lost 32 events are also shown, with their PRL2008 masses, as blue triangles. The sharp peak in PRL2008 (13 events in a single bin), interpreted as the Ω_b^- signal, is no longer present in the new data. This is partly due to the common events having their masses spread out away from the peak (2 events lost from peak bin), and partly due to the missing events, which also happen to peak at the same mass (5 events lost), leaving only 6 events in this bin for the new analysis.

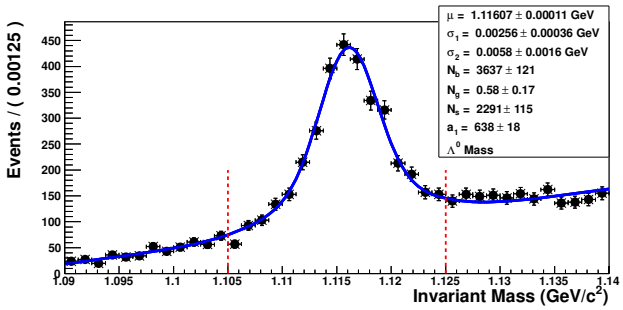

(a) $M(\Lambda^0)$ (Run IIa).

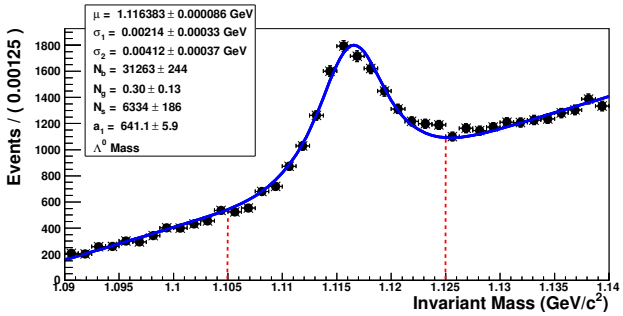

(b) $M(\Lambda^0)$ (Run IIb).

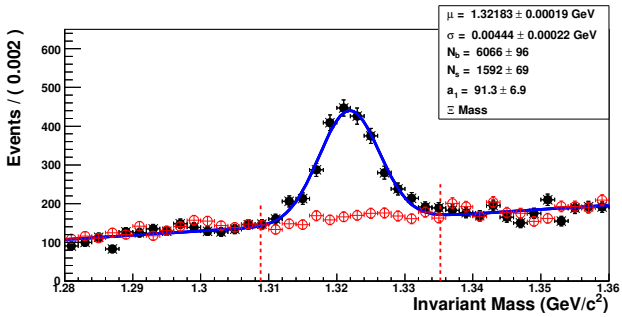

(c) $M(\Xi^-)$ (Run IIa).

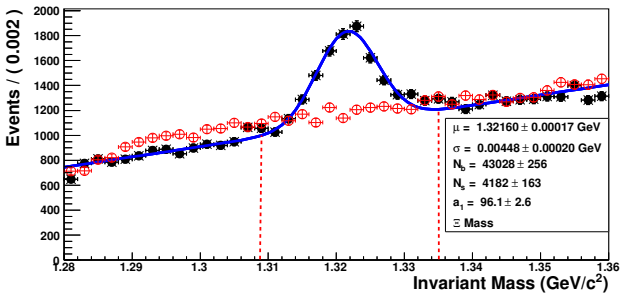

(d) $M(\Xi^-)$ (Run IIb).

Figure 5.4: Λ^0 and Ξ^- invariant mass distributions after preselection requirements have been applied (filled circles). Also shown are the results of fits to the data to extract the yields (solid lines). For the Ξ^- case, the wrong-sign distribution is also plotted (empty circles). The dashed vertical lines demarcate the mass windows used to define the preselection sample. The relative increase in background for the Run IIb sample is clearly visible, and is expected from the increased instantaneous luminosity.

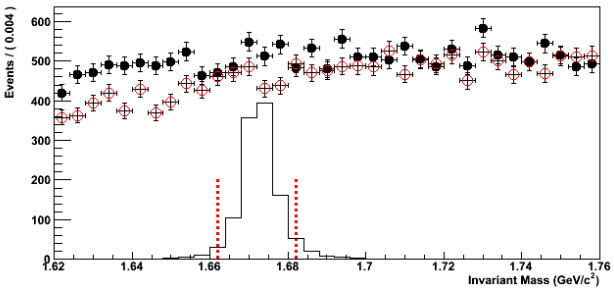

(a) $M(\Omega^-)$ (Run IIa, preselection).

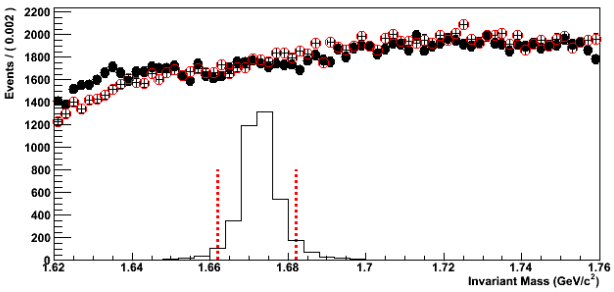

(b) $M(\Omega^-)$ (Run IIb, preselection).

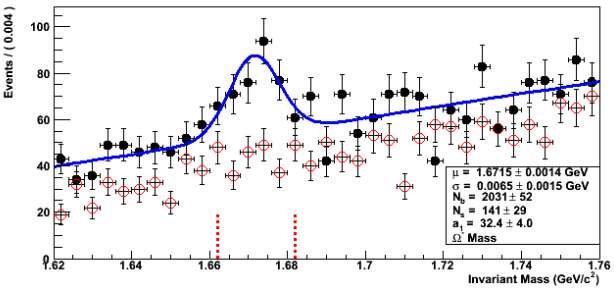

(c) $M(\Omega^-)$ (Run IIa, preselection and extra cuts).

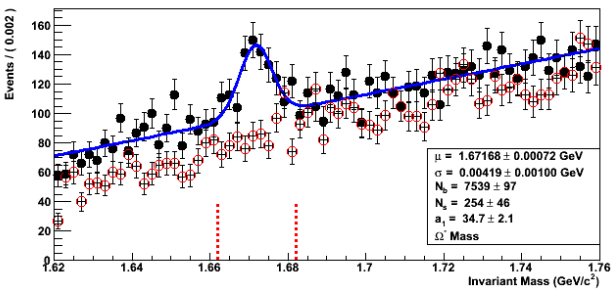

(d) $M(\Omega^-)$ (Run IIb, preselection and extra cuts).

Figure 5.5: Ω^- invariant mass distributions for right-sign (filled circles) and wrong-sign (empty circles) candidates. The top two plots show the distributions after preselection requirements have been applied, and include overlaid histograms of the MC simulation to indicate the Ω^- signal shape. The bottom two plots show the distributions with a few additional cuts to demonstrate the signal presence (described in text). Also shown are the results of fits to the data to extract the yields where possible (solid lines). The dashed vertical lines demarcate the mass windows used to define the preselection sample.

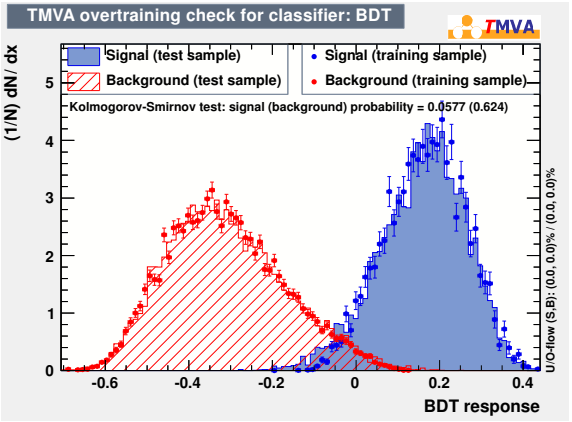

(a) Ξ_b^- BDT^{42} output (Run IIb).

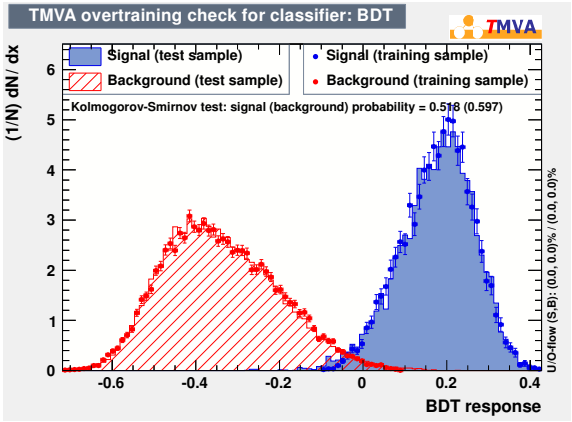

(b) Ω_b^- BDT^{42} output (Run IIb).

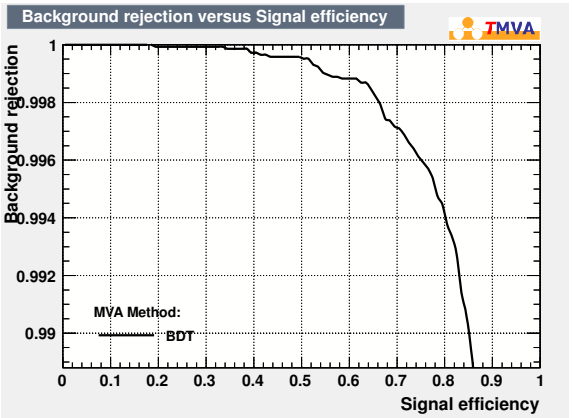

(c) Ξ_b^- BDT performance curve (Run IIb).

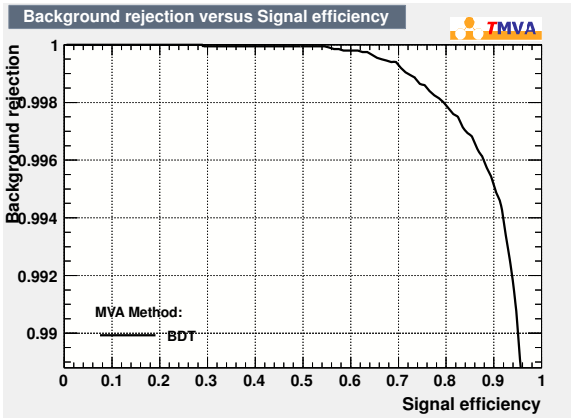

(d) Ω_b^- BDT performance curve (Run IIb).

Figure 5.6: TMVA plots demonstrating the performance of the BDT^{42} discriminants for both channels, for the Run IIb samples used in training. Top row: BDT output distributions for signal and background samples showing the consistency of the training and testing sample distributions. Bottom row: Background rejection versus signal efficiency curves, zoomed into the region of interest.

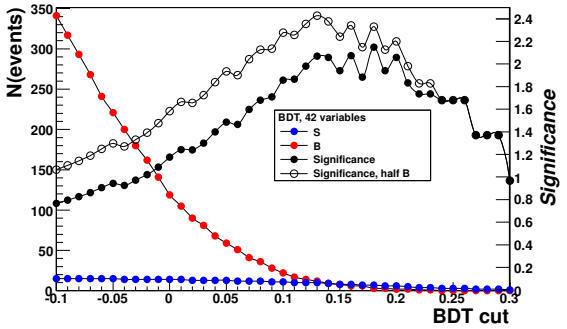

(a) Ξ_b^- (Run IIa).

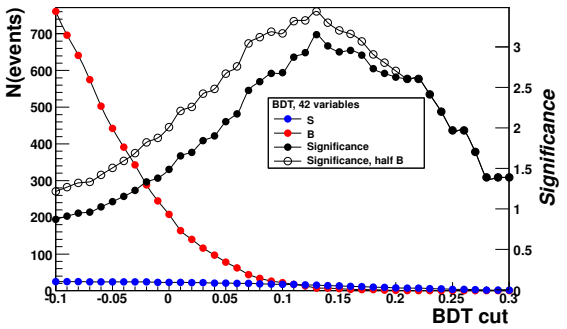

(b) Ξ_b^- (Run IIb.)

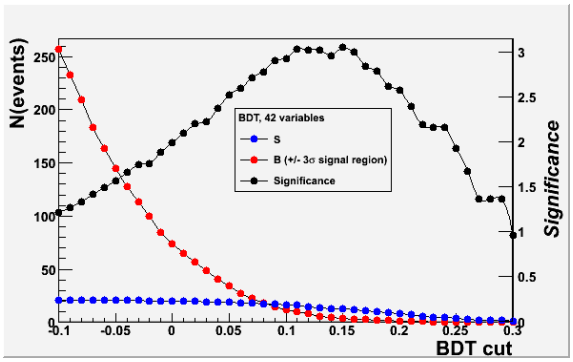

(c) Ω_b^- (Full Run II sample, assuming 21.2 signal candidates at preselection.)

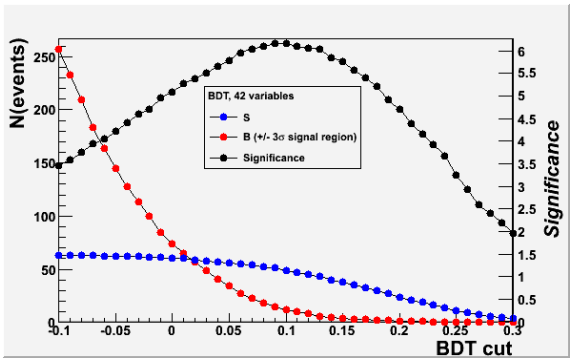

(d) Ω_b^- (Full Run II sample, assuming 62.8 signal candidates at preselection.)

Figure 5.7: Expected signal and background yields, and signal significance, as a function of the minimum BDT[42] cut, for both channels, with Run IIa and Run IIb examined separately for the Ξ_b^- case. For the Ω_b^- case, we examine two possible input assumptions of the number of signal events after preselection cuts are applied (see Section 5.1.5).

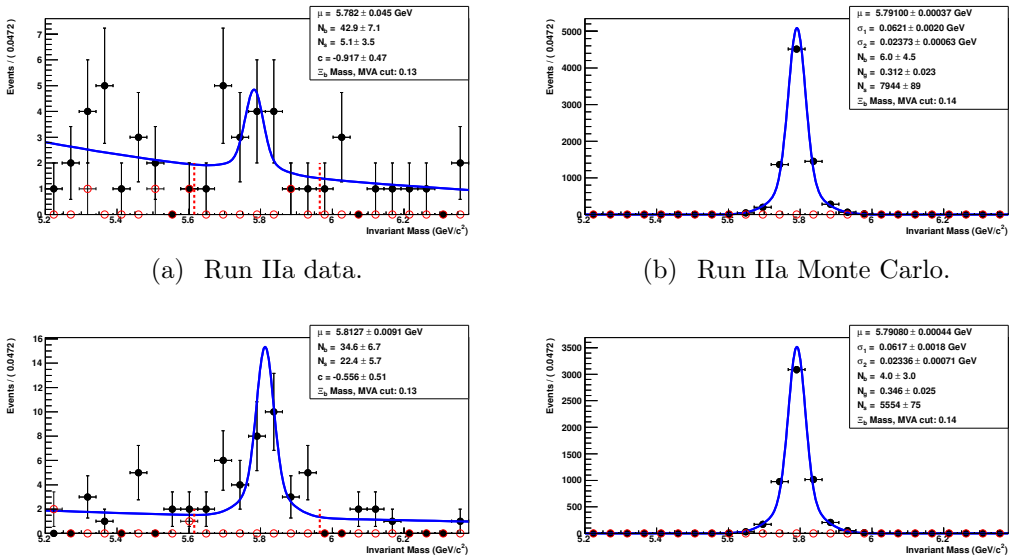

(a) Run IIa data. (b) Run IIa Monte Carlo.

(c) Run IIb data. (d) Run IIb Monte Carlo.

Figure 5.8: $M(\Xi_b^-)$ distribution after application of all selection requirements, for data (left) and Monte Carlo (right), with Run IIa (top) and Run IIb (bottom) shown separately. Also shown are the projections of the unbinned maximum likelihood fits (double Gaussian for signal, exponential for background). The results from the MC are used to fix the signal model in the fit to data.

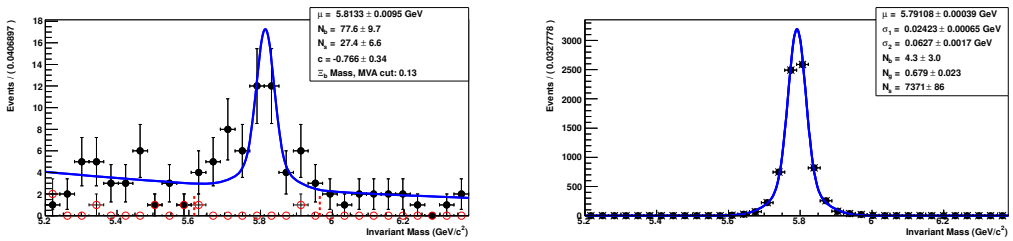

(a) Combined Run II data. (b) Combined Run II Monte Carlo.

Figure 5.9: $M(\Xi_b^-)$ distribution after application of all selection requirements, for the combined Run II sample, for data (left) and Monte Carlo (right). The MC sample is created by combining Run IIa and IIb samples in proportion to the signal yields measured from data.

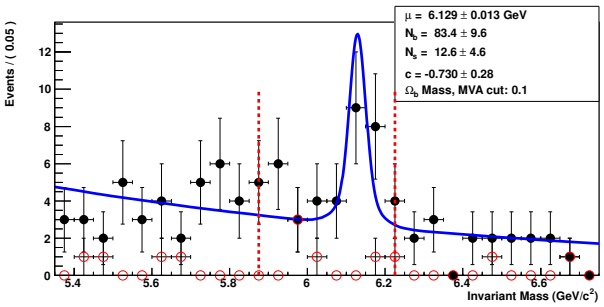

(a) Combined Run II data.

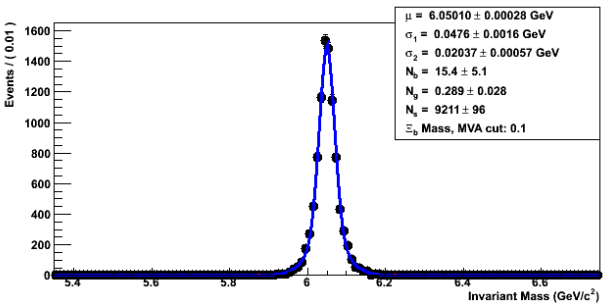

(b) Combined Run IIb Monte Carlo.

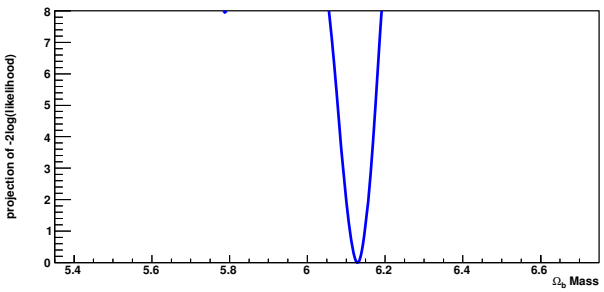

(c) Combined Run II likelihood profile.

Figure 5.10: $M(\Omega_b^-)$ distribution after application of all selection requirements, for the combined Run II sample, for data (a) and Monte Carlo (b). The hollow circles in the data plot indicate the distribution for wrong-sign events. Also shown is the likelihood profile for the data fit, versus the Ω_b^- fitted mass.

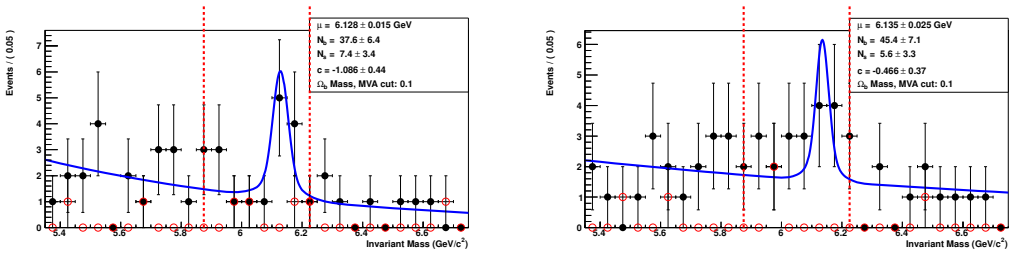

(a) Run IIa data. (b) Run IIb data.

Figure 5.11: $M(\Omega_b^-)$ distribution after application of all selection requirements, for the Run IIa sample (left) and Run IIb sample (right).

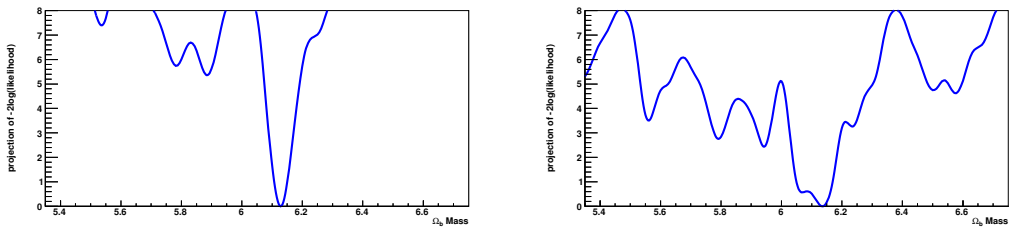

(a) Run IIa data. (b) Run IIb data.

Figure 5.12: Likelihood profiles versus the fitted Ω_b^- mass, for the Run IIa sample (left) and Run IIb sample (right).

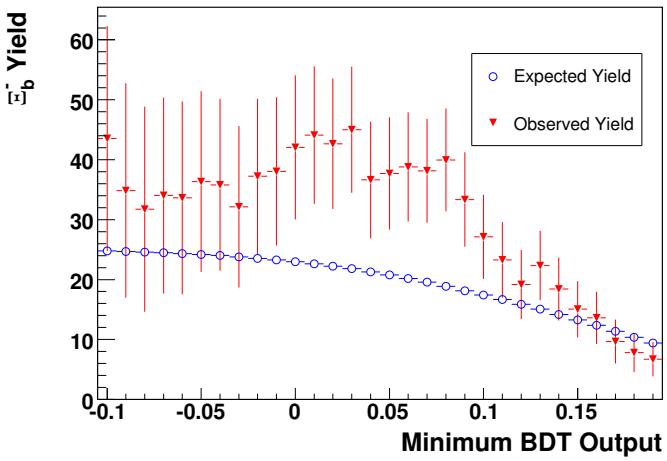

(a) Expected and observed signal yields.

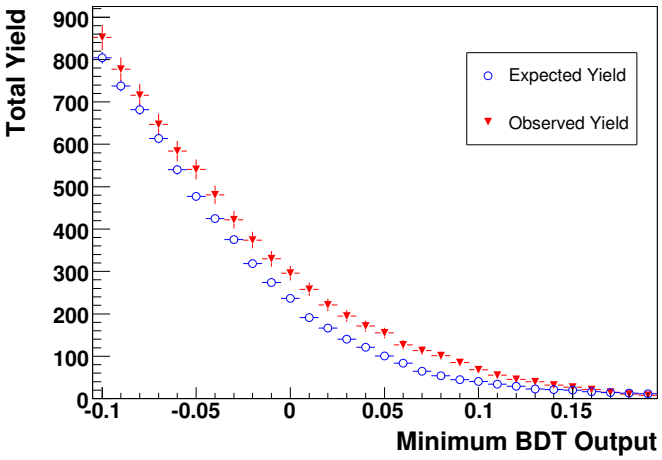

(b) Expected and observed total yields.

Figure 5.13: Cross-check applied to the unblinded Run IIb data, in which the BDT[42] requirement is varied, and the expected and observed yields are determined for each cut. Note that this uses a binned fit, so lacks the full power and reliability of the default (unbined) fit used in this analysis.

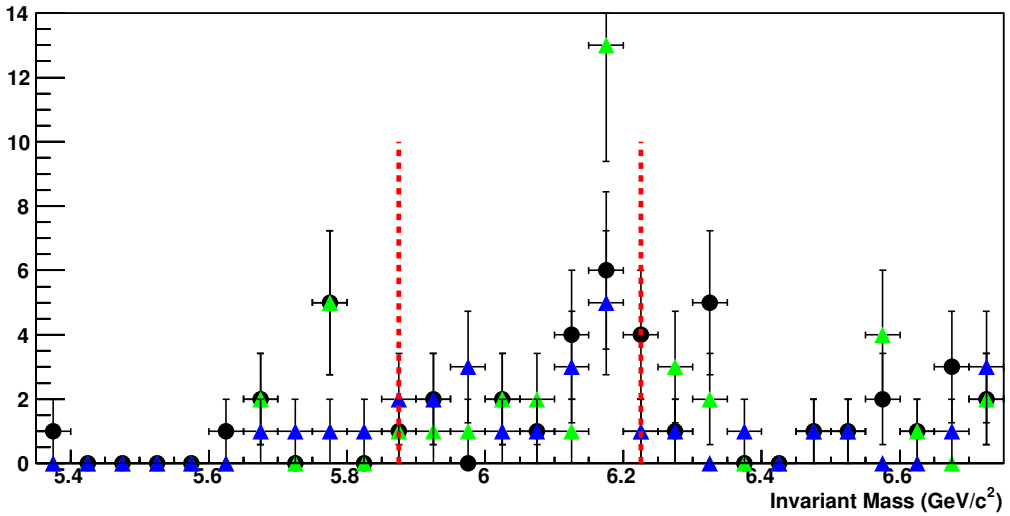

(a)

Figure 5.14: Comparison of the reconstructed Ω_b^- masses, for the 78 events from PRL2008 (green triangles, PRL2008 masses), the 46 events from PRL2008 reconstructed with the new tracking algorithm (black circles, new masses), and the 32 events failing the new tracking algorithm (blue triangles, PRL2008 masses).

Chapter 6

Measurement of the forward-backward asymmetry in the Λ_b and $\bar{\Lambda}_b$ production in $p\bar{p}$ collisions at $\sqrt{s} = 1.96$ TeV

6.1 Introduction

In the quark-parton model, hadroproduction of particles carrying a heavy quark Q (Q=b,c) proceeds through a gluon-gluon fusion, gg $\rightarrow$ QQ or quark-antiquark annihilation, qq $\rightarrow$ QQ [30] followed by the hadronization of the heavy quarks. At the parton level, in the leading-order QCD, Q and Q quarks are produced symmetrically. Next-to- leading order QCD may introduce a small 1% asymmetry in Q and Q momenta due to interferences of contributing amplitudes. However, the hadronization process may change the direction of the particle carrying the Q quark relative to the Q quark direction and thus generate a significant asymmetry. Heavy baryon production rates are several orders of magnitude smaller than the heavy meson production rates. Contrary to the case of B mesons, there has been few studies of b baryon production. Production of heavy baryons is sensitive to effects of non-perturbative final state interactions of a QCD string connecting a Q quark and a remnant of the projectile. The case of the ground-state b baryon Λ_b^0 and its antiparticle has been recently discussed by Rosner [31]. Figure 6.1 adapted from Ref [41] illustrates the mechanism that is expected to contribute to the Λ_b^0 baryon production and that favors production of Λ_b^0 by protons and $\bar{\Lambda}_b^0$ by antiprotons.

In this Article we present a study of the forward-backward production asymmetry of Λ_b^0 and Λ_b^0 particles using a sample of the fully reconstructed decay chain $\Lambda_b^0 \rightarrow J/\psi\Lambda, J/\psi \rightarrow \mu^+\mu, \Lambda \rightarrow p\pi$ and its charge conjugate (c.c). The forward category corresponds to a particle sharing valence quarks with the beam at the same sign of rapidity, defined as $y = ln((E + p_z)/(Ep_z))/2$. In $p\bar{p}$ collisions, the forward direction means a Λ_b^0 particle emitted with $y > 0$ or Λ_b^0 emitted at $y < 0$. In $p\bar{p}$ collisions, Λ_b^0 particles ($\bar{\Lambda}_b^0$) belong to the forward (backward) category. To facilitate a comparison with existing related measurements, we present a measurement of the ratio of the backward to forward production cross sections, $R = \sigma(B)/\sigma(F)$ as well as the asymmetry $A = (\sigma(F)\sigma(B))/(\sigma(F) + \sigma(B))$ as functions of the rapidity. The data sample corresponds to an integrated luminosity of $10.4fb^1$ collected with the DØ detector in $p\bar{p}$ collisions at the Fermilab Tevatron collider.

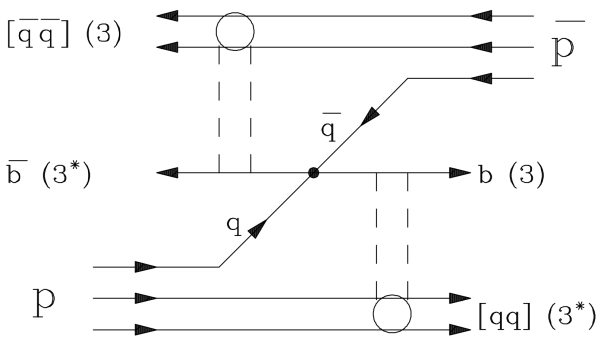

Figure 6.1: Diagram of Λ_b^0 production adapted from Ref [30] illustrating the interaction of final state quarks b and b with spectator systems through QCD strings.

6.2 Data sample

The DØ detector consists of a central tracking system, calorimetry system and muon detectors, as detailed in Ref [33]. The central tracking system comprises a silicon microstrip tracker (SMT) and a central fiber tracker (CFT), both located inside a 1.9 T superconducting solenoidal magnet. The tracking system is designed to optimize tracking and vertexing for pseudorapidities $|\eta| < 3$, where $\eta = ln[tan(\theta/2)]$, and θ is the polar angle with respect to the proton beam direction. The SMT can reconstruct the pp interaction vertex (PV) for interactions with at least three tracks with a precision of $40\mu m$ in the plane transverse to the beam direction. The muon detector, positioned outside the calorimeter, consists of a central muon system covering the pseudorapidity region of $|\eta| < 1$ and a forward muon system covering the pseudorapidity region of $1 < |\eta| < 2$. Both central and forward systems consist of a layer of drift tubes and scintillators inside 1.8 T toroidal magnets and two similar layers outside the toroids [34].

6.3 Event reconstruction and candidate selection

Candidate events are required to include a pair of oppositely charged muons accompanied by a pair of oppositely charged tracks forming a vertex (DV) consistent with a decay $\Lambda \to p\pi$ or $\bar{\Lambda} \to \bar{p}\pi^+$. One muon is required to be detected in the muon chambers inside and outside the toroid magnet. The other muon may be detected only inside the toroid or just as a track-like object in the calorimeter. Each muon candidate is required to match a track found in the central tracking system. To form Λ_b^0 (and c.c) candidates, muon pairs in the invariant mass range $2.9 < M(\mu^+\mu) < 3.3$ GeV, consistent with J/ψ decay, are combined with Λ candidates formed from pairs of oppositely charged particles consistent with originating from a common vertex. The particle with the higher momentum is assigned a proton mass. The Λ candidate is required to have an invariant mass between 1.107 GeV and 1.125 GeV and a transverse momentum greater than 1.8 GeV. The separation of the ÎŻ decay vertex from the DV in the transverse plane must be greater than

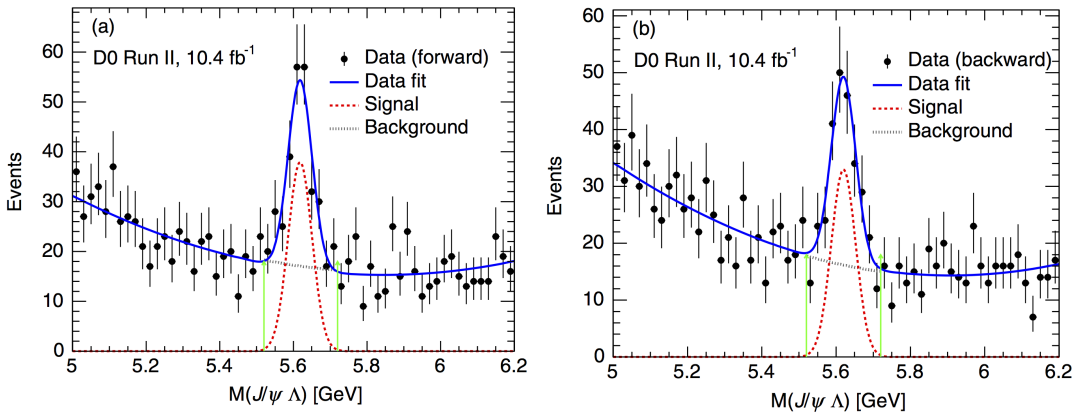

(a) (b)

Figure 6.2: Invariant mass distribution of $\Lambda_b^0 \to J/\psi\Lambda$ and $\bar{\Lambda}_b^0 \to J/\psi\bar{\Lambda}$ candidates in the rapidity range $0.5 < y < 1.0$ in (a) forward and (b) backward category. The fit of a Gaussian signal with a second-order Chebyshev polynomial background is superimposed. The vertical green lines define the signal region.

0.5 cm and less than 25 cm. The dimuon invariant mass is constrained in the kinematic fit to the world-average $J\psi$ mass [35] and the $J/\psi\Lambda$ system is constrained to a common vertex DV. The trajectories of the Λ_b^0 decay products are adjusted according to the decay and kinematic fit. The adjusted track parameters are used in the calculation of the Λ_b^0 candidate invariant mass. The allowed mass range is $5.0 < M(J/\psi\Lambda) < 6.2$ GeV. The number of candidates that satisfy the above conditions is 59535. To suppress the large background from prompt J/ψ production we require a significant separation of DV from the primary vertex PV. To reconstruct the PV, tracks are selected that do not originate from the candidate Λ_b^0 decay, and a constraint is applied to the average beam-spot position

in the transverse plane. We define the signed decay length of a Λ_b^0 baryon, L_{xy}, as the vector pointing from the PV to the DV, projected on the transverse plane. We require L_{xy} to be greater than three times its uncertainty. The total number of accepted Λ_b^0 candidates is 8107. The mass distributions for candidates in the rapidity range $0.5 < \mathrm{y} < 1.0$ in the forward and backward categories are shown in Figure 6.2. Binned maximum-likelihood fits of a Gaussian signal and a second-order Chebyshev polynomial background yield the forward (backward) signal with a mean mass of $M(\Lambda_b^0) = 5618.1 \pm 4.3$ MeV(5619.9 ± 4.7), consistent with each other and with the world-average value of Λ_b^0 mass [35]. The width depends on rapidity and varies between 30 and 50 MeV. In this example the fitted widths are $32.5 \pm 5.1(32.8 \pm 5.1)$ MeV. We define the signal region as the mass range within ± 2.5 times the mass resolution from the world-average value. In Figure 6.3 we show the distribution of the Λ_b^0 candidate p_T Vs y and of the reconstructed Λ candidates in the signal region. The average p_T value for signal events is 11.3 GeV.

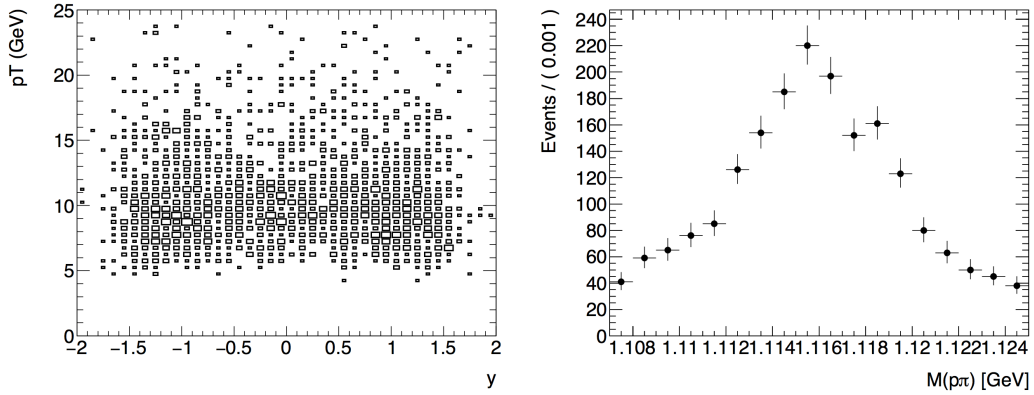

Figure 6.3: (a) Distribution of the Λ_b^0 candidate transverse momenta vs rapidity in the signal region. (b) Invariant mass distribution of $\Lambda \to p\pi^-$ (and c.c) candidates in the signal region.

Generator	Request numbers	Label	N_{gen}	N_{reco}	N_{sel}
Pythia, MSEL = 1	204992 - 205001	PythiaQCD	11,034,692	69,637	30,772
	205032 - 205041				
	205192 - 205241				
MC@NLO+Herwig	204892 - 204896	MC@NLO	841,487	961	267

Table 6.1: MC samples. N_{gen} and N_{reco} are the number of generated and reconstructed events. N_{sel} is the number of reconstructed decays which satisfy the final selection criteria.

6.4 Monte Carlo samples

Monte-Carlo (MC) simulations are obtained at LO with Pythia [36] and at NLO with MC@NLO [42], using parton distribution functions sets CTEQ6L1 and CTEQ6M1 [38], respectively. Pythia generates $b\bar{b}$ quark pairs flavour excitation, $qg \to bg$, and gluon splittings, $g \to b\bar{b}$ (MSEL = 1). On the other hand, MC@NLO is interfaced with Herwig [39] for parton showering and hadronization. After hadronization, b hadrons are decayed with the EvtGen [40] package. In this particular study, Λ_b^0 (c.c.) is always forced to decay to $J/\psi\Lambda$ (c.c.), $J/\psi \to \mu^+\mu$, using the phase space (PHSP) and vector to lepton-lepton (VLL) models in EvtGen. The detector response is simulated with Geant3 [41] and multiple pp ÌĎ interactions (pile-up) are modeled by overlaying hits from random real bunch crossings (called ZB-overlay). Run-IIb3 DØ software release p20.17.02 was used to create these simulations. Unless stated otherwise, events with muons from J/ψ meson decay, which are too soft ($p_T(\mu^\pm) < 1.0$) or too forward ($|\eta(\mu^\pm)| > 2.5$) to be reconstructed, are discarded before the detector simulation step. After requiring a Λ_b^0 (or c.c.) in the event and the previous requirements, DØmess efficiency is on the order of $\sim$ 10-4 ($\sim$ 10-5) for generation with Pythia MSEL = 1 (MC@NLO). MC (thumbnails) files have been reprocessed with the extended AA-Track reconstruction as done with data (J/ψ skim) [1] Table 6.1 summarizes the generated MC samples, containing Λ_b^0 or $\bar{\Lambda}_b^0$ (or both).

During data taking, the polarities of the magnets were regularly reversed. In order to study in detail the effects induced by the magnets, independent samples were simulated with specific polarities of the solenoid (S) and toroid (T), both in positive (P) and negative (N) configurations, and corresponding ZB-overlay. By default, DØ MC simulations (including samples in Table 6.1) use the SPTP configuration and the entire sample of ZB-overlay. Table 6.2 summarizes the generated MC samples with specific magnets polarities.

[1] After the reprocessing and AADST conversion, some MC events (or parts of the event) are unreadable. For the moment and for simplicity, we just skip the whole AADST file. The problem is less frequent in the newest releases

Generator	Request numbers	N_{gen}	N_{reco}	N_{sel}	N_{sel}/N_{gen}
SPTP	205112 - 205116	974,863	4167	1,977	0.00203 ± 0.00005
SPTN	205117 - 205121	1,030,413	4659	2,245	0.00218 ± 0.00005
SNTP	205122 - 205126	1,034,662	4634	2,163	0.00209 ± 0.00005
SNTN	205127 - 205131	1,030,977	4592	2,159	0.00209 ± 0.00005

Table 6.2: MC samples with specific polarities of the magnets.

6.5 Detector effects

We study the effects of the event selection and reconstruction efficiency on the rapidity distribution of Λ_b^0 and $\bar{\Lambda}_b^0$ baryons by comparing the distributions of generated and reconstructed particles in the forward and backward category in events simulated with Pythia. As seen in Figure 6.4, the procedure of simulating detector response, event reconstruction and candidate selection does not introduce a significant forward-backward asymmetry. The ratio of the backward to forward detection efficiencies is constant to an accuracy of 3%.

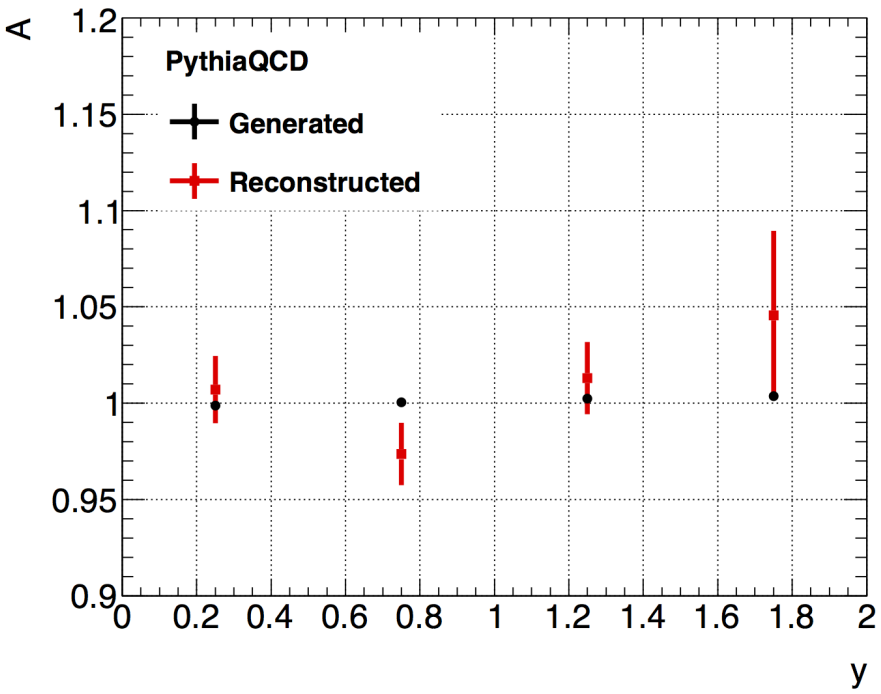

Figure 6.4: Rapidity dependence of the asymmetry from Pythia for all simulated events (black points) and for reconstructed events (red points).

6.6 Measurement of forward-backward asymmetry

The p_z distributions and rapidity distributions of Λ_b^0 and $\bar{\Lambda}_b^0$ candidates in the signal region are shown in Figure 6.5 a and b. The measured difference between the average values of pz Λ_b^0 and $\bar{\Lambda}_b^0$ candidates in the signal region is 2.2 ± 0.7 GeV. In addition to this average shift, there is an excess of the number of reconstructed Λ_b^0 candidates. As mentioned before, it can be explained as the effect of the loss of Λ particles due to inelastic interactions of antiprotons with matter. This asymmetry in the absolute yield cancels out in the comparison of the forward and backward rates, as seen in Figure 6.5 c. Background consists of random pairs of J/ψ mesons from b hadrons and Λ candidates. We assume that background is well represented by all events, independent of the decay length, in the Λ_b^0 sidebands. The same distributions for the background sample are shown in Figure 6.5 d-f. The distributions of p_z and rapidity for background show no forward-backward asymmetry. The difference between the mean values is $\Delta p_z = 0.12 \pm 0.12$ GeV. Again, there is a 2% excess of the rate of the Λ_b^0 candidates over $\bar{\Lambda}_b^0$. The excess cancels out in the forward - backward rates. The production rates of forward and backward Λ_b^0 and $\bar{\Lambda}_b^0$ particles are extracted from fits to the invariant mass distributions of forward and backward candidates in four rapidity bins in the range $0.1 < y < 2$, as defined in Table IV. We reject the region $y < 0.1$ where the asymmetry may be diluted by the forward-backward migration due to the limited polar angle resolution. In the fits, the signal is described by a Gaussian function with free mass and width parameters. The background is described by a second-order Chebychev polynomial. Most of the systematic uncertainties in the production cross sections of Λ_b^0 and $\bar{\Lambda}_b^0$ particles that arise from uncertainties in the kinematic acceptance and detection efficiency of final-state particles cancel out in the measurements of the asymmetry A and ratio R. The remaining uncertainties are due to the signal and background shapes in the mass fits and in the relative efficiency of the forward and backward particle reconstruction. The uncertainty in the signal shape is estimated by constraining the width parameters for the forward and backward categories to be equal. The sensitivity to the background shape is estimated by increasing the lower mass cut to 5.2 GeV, thus excluding the mass range where feed-down from multi-body b baryon decays may be present. The estimate of the uncertainty in the detection efficiency is based on the average deviation from unity, as seen in Figure 6.4. Adding the above uncertainties in quadrature results in the total systematic uncertainty of ± 4.

The fitted signal yields and the resulting forward-backward asymmetry A and backward-to-forward ratio R are presented in Table IV. The asymmetry as a function of rapidity is shown in Figure 6.6. There is a wide range of model predictions for this asymmetry. The "Heavy Quark Recombination" (HQR) model [43], as shown in Figure 6.6, predicts a modest asymmetry, reaching $\sim 2.5\%$ near $y = 2$. While Pythia predicts no asymmetry, the MC@NLO generator predicts a large asymmetry, reaching 100% near $y = 2$. Our results are consistent with perfect symmetry within the large uncertainties, although they show a trend of the asymmetry A increasing with rapidity that could be interpreted as the effect of the longitudinal momentum imparted on a Λ_b^0 or $\bar{\Lambda}_b^0$ particle by the beam

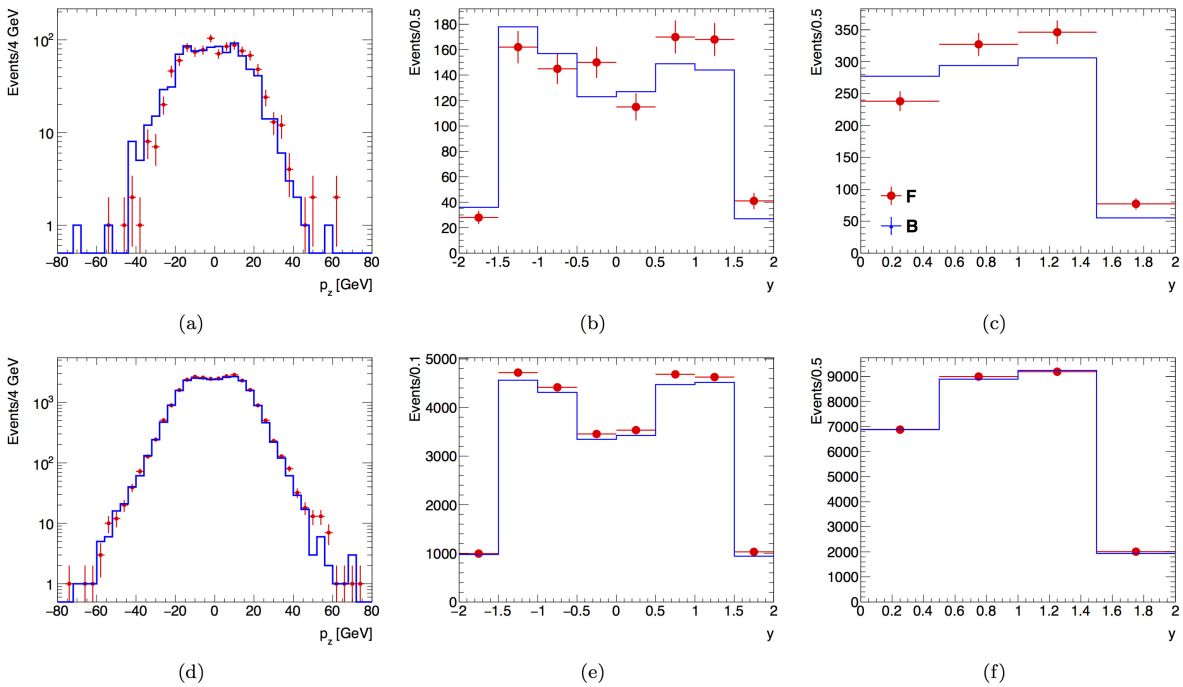

Figure 6.5: Comparison of distributions of Λ_b^0 and $\bar{\Lambda}_b^0$ candidates in the signal region: (a) p_z distributions of Λ_b^0 (red points) and $\bar{\Lambda}_b^0$ candidates (blue histogram), (b) rapidity distribution of Λ_b^0 (red points) and $\bar{\Lambda}_b^0$ candidates (blue histogram), (c) rapidity loss distributions of the forward (red points) and backward (blue histogram) candidates (see text for the definitions). Same comparison is shown (bottom plots, d-f) for candidates in the Λ_b^0 sidebands.

remnant. Assuming a linear confinement potential with string tension of 0.18 GeV2, Rosner [31] made an approximate prediction of $\Delta y = 1.4/p_T$ for the string drag effect on the Λ_b^0 rapidity. We have simulated this effect by adding the above amount to the rapidity of the forward particle in the generated Pythia events , while leaving the rapidity of the backward particle unchanged. As seen in Figure 6.6, our result is in a good agreement with this prediction. We find our results in disagreement with the large asymmetry predicted by MC@NLO. Such an asymmetry would result from clusters formed by a b quark and ud diquarks having a small mass, just sufficient to coalesce into a single particle. The asymmetry integrated over rapidity is $A = 0.04 \pm 0.06 \pm 0.02$

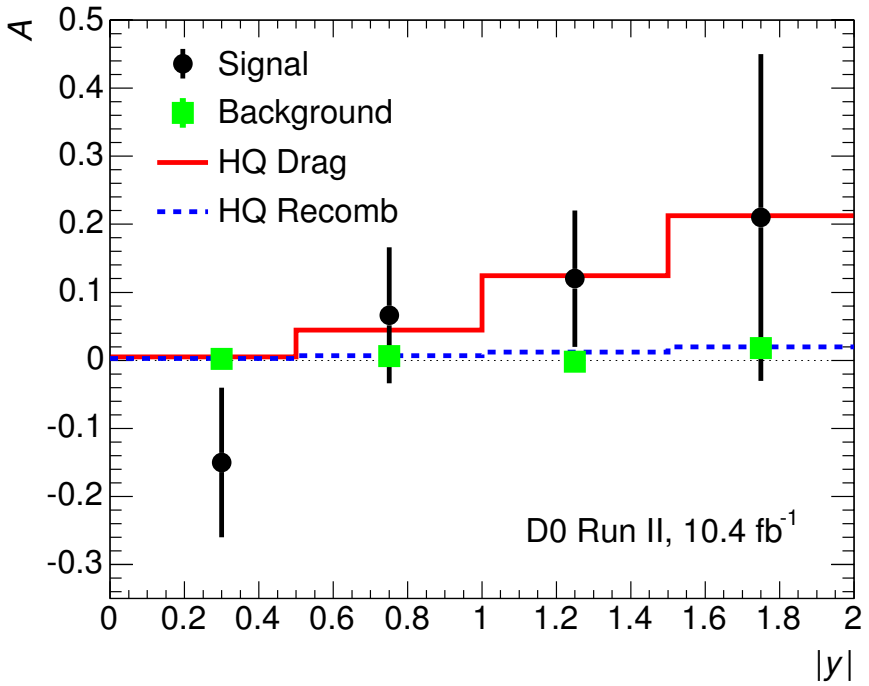

Figure 6.6: Measured forward-backward asymmetry A versus rapidity $|y|$ compared to predictions of the Heavy Quark Recombination model [43] and a simulated effect of the longitudinal momentum shift due to beam drag (see Ref [31] and text). The background asymmetry is obtained from $J/\psi\Lambda$ candidates in the Λ_b^0 mass sidebands (uncertainties are small compared to the symbol size). Measurements are placed at the centers of the rapidity intervals defined in Table 6.4

The results for the backward-to-forward ratio R for the same rapidity intervals are shown in Figure 6.7. Also shown are the results for the ratio of cross sections $\sigma(\bar{\Lambda}_b^0)/\sigma(\Lambda_b^0)$ for the five rapidity bins reported by CMS [44] and a single measurement of this ratio by the LHCb Collaboration [45]. All results are presented as functions of the âĂIJrapidity lossâĂİ defined as the difference between the rapidity of the beam and the rapidity of the particle. The DØ and CMS results are consistent within large uncertainites. They are also

Source	Uncertainty (%)
Signal shape	2.0
Background shape	2.0
Detection efficiency	3.0
Total	4.0

Table 6.3: Systematic uncertainties (in %) on the measurement of the backward-to-forward ratio R.

$\|y\|$	ϵ (%)	$\langle p_T \rangle$ (GeV)	$N(B)$	$N(F)$	$A \pm$ (stat) $\pm$ (syst)	$R \pm$ (stat) $\pm$ (syst)
0.1-0.5	0.70 ± 0.01	10.2 ± 0.1	125 ± 18	92 ± 17	$0.15 \pm 0.11 \pm 0.03$	$1.36 \pm 0.32 \pm 0.06$
0.5-1.0	1.01 ± 0.01	10.0 ± 0.1	135 ± 19	154 ± 22	$0.07 \pm 0.10 \pm 0.02$	$0.88 \pm 0.18 \pm 0.04$
1.0-1.5	0.97 ± 0.01	9.7 ± 0.1	123 ± 16	158 ± 23	$0.12 \pm 0.10 \pm 0.02$	$0.78 \pm 0.15 \pm 0.04$
1.5-2.0	0.32 ± 0.01	9.8 ± 0.2	22 ± 9	33 ± 10	$0.21 \pm 0.24 \pm 0.02$	$0.67 \pm 0.34 \pm 0.03$

Table 6.4: Efficiencies ϵ, averaged values of background-subtracted transverse momenta $\langle p_T \rangle$, backward and forward fitted yields for the signal$N(B)$ and $N(F)$, forward-backward asymmetries A, and cross-section ratios R in four intervals of rapidity. Uncertainties on $\langle p_T \rangle$, $N(B)$ and $N(F)$ are statistical only. Uncertainties on ϵ arise from the statistical precision of the simulated event samples..

consistent with the $\sigma(\bar{\Lambda}_b^0)/\sigma(\Lambda_b^0)$ ratio measured by LHCb in the forward rapidity range at the LHC. Together, they show a trend of R to fall with increasing rapidity (decreasing rapidity loss). The average R, integrated over the full range of rapidity is consistent with unity. For DØ, the result is $R = 0.93 \pm 0.11 \pm 0.04$, to be compared with the value of $1.02 \pm 0.07 \pm 0.09$ reported by CMS.

As a cross-check, we have obtained the backward-to-forward ratio using candidates (i) with y > 0, (ii) y < 0, (iii) Λ_b^0 only, and (iv) Λ_b^0 only. The results are summarised in Table V. Within large statistical uncertainties they are consistent with the standard results. Using the same data set, DØ has studied the forward-backward asymmetry in the production of $B^{\pm}$ mesons. The $B^{\pm}$ data show no rapidity dependence. The measured forward-backward asymmetry in the production of $B^{\pm}$ mesons, where the forward category corresponds to the B meson, carrying a b quark produced with y > 0, and the B^+ meson produced at y < 0, integrated over rapidity, is $AFB(B^{\pm}) = [0.24 \pm 0.41(\text{stat}) \ \pm 0.19(\text{syst})\ ]\%$ [32].

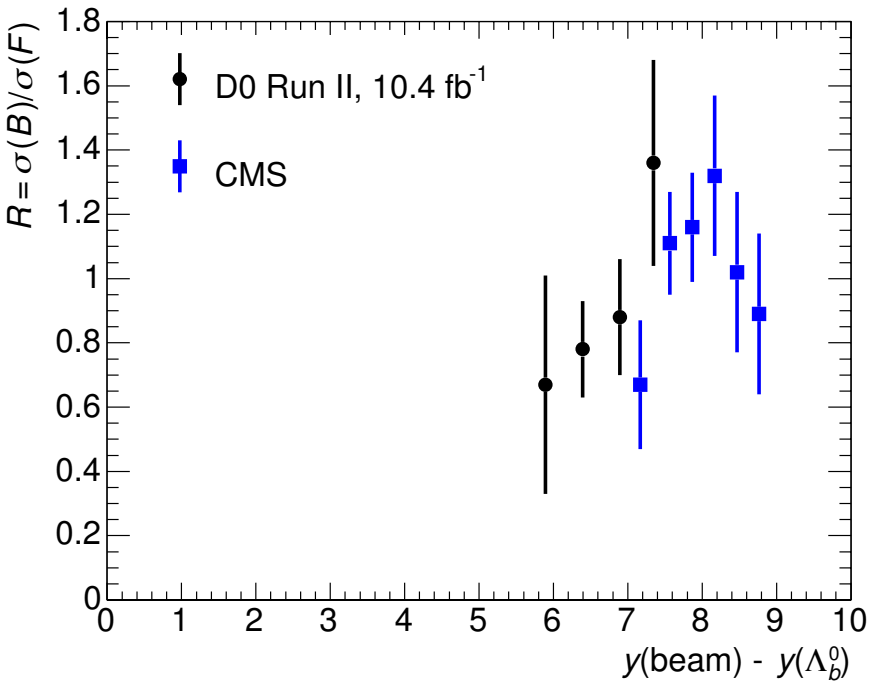

Figure 6.7: Measured ratio of the backward to forward production cross sections versus rapidity loss compared to the Λ_b^0 to $\bar{\Lambda}_b^0$ production cross section ratio at CMS taken from Table II of Ref. [44], and at LHCb [45].

6.7 Summary

In summary, we have presented a measurement of the forward-backward asymmetry in the production of Λ_b^0 and $\bar{\Lambda}_b^0$ baryons as a function of rapidity. Together with related results from the LHC, the data show a tendency of forward particles, sharing valence quarks with beam remnants, to be emitted at larger values of rapidity (smaller rapidity loss) than their backward counterparts. It is the first indication of the universality of the production of heavy baryons in hadron-hadron collisions. Our measured ratio of the backward-to-forward production rate at the average transverse momentum of 11.4 GeV, averaged over rapidity in the range $0.1 < y < 2.0$ is $R = 0.93 \pm 0.11(\text{stat}) \pm 0.04(\text{syst})$. The forward-backward asymmetry is $A = 0.04 \pm 0.06 \pm 0.02$ We thank W. K. Lai and A. .K. Leibovich for providing predictions of the Heavy Quark Recombination model for the DØ kinematic range

Chapter 7

Conclusions and Perspectives

We have performed searches for the Ξ_b^- and Ω_b^- baryons in the complete Run II data sample, using multivariate techniques. The Run IIa analysis gives a signal yield of 5.1 ± 3.5 Ξ_b^- events, with the peak having a statistical significance of 1.8σ, and a mass measurement of 5.782 ± 0.045 (stat.) GeV. The Run II sample finds 27.4 ± 6.6 Ξ_b^- events, with a significance of 5.9σ, and a mass of 5.813 ± 0.010 (stat.) GeV.

For the Ω_b^- channel, we observe a small peaking structure with 3σ significance, largely driven by the Run IIa data. The peak mass is 6129 ± 13 MeV, significantly above the known Ω_b^- mass. We therefore do not interpret this excess as an Ω_b^- signal, rather an upward fluctuation of the background. Given the observed Ξ_b^- yields, a non-observation of the Ω_b^- baryon is consistent with expectations.

The following is a list of studies to be performed on this analysis.

- Cross-checks
  - Repeat the Ξ_b^- BDT training, testing, and application using the simplified $b\bar{b}$ Monte Carlo sample to model the signal, rather than the current generic $q\bar{q}$ sample. Determining any effects of this simplification is important, since the Ω_b^- search uses $b\bar{b}$ MC model, and we currently assume that both models can be equally trusted to report the correct reconstruction efficiencies..
  - Investigate the systematic uncertainties on the Ξ_b^- and Ω_b^- mass and yield measurement, and on the statistical significance.
  - Generate pseudoexperiment ensembles to properly evaluate signal significances.
- Ξ_b^- Lifetime measurement:
  - Remove events satisfying only IP-biased triggers.
  - Determine decay-time efficiency using simulation and apply correction if necessary.
  - Perform Ξ_b^- and Ω_b^- lifetime fits using the full Run II sample.
  - Validate and test fits using MC closure tests.

Regarding the AFB analysis we have presented a measurement of the forward-backward asymmetry in the production of Λ_b^0 and $\bar{\Lambda}_b^0$ baryons as a function of rapidity. Together with related results from the LHC, the data show a tendency of forward particles, sharing valence quarks with beam remnants, to be emitted at larger values of rapidity (smaller rapidity loss) than their backward counterparts. It is the first indication of the universality of the production of heavy baryons in hadron-hadron collisions. Our measured ratio of the backward-to-forward production rate at the average transverse momentum of 11.4 GeV, averaged over rapidity in the range $0.1 < y < 2.0$ is $R = 0.93 \pm 0.11(\text{stat}) \pm 0.04(\text{syst})$. The forward-backward asymmetry is $A = 0.04 \pm 0.06 \pm 0.02$ We thank W. K. Lai and A. .K. Leibovich for providing predictions of the Heavy Quark Recombination model for the DØ kinematic range.

Bibliography

[1] V. M. Abazov *et al.* [DØ Collaboration], "Direct observation of the strange b baryon Ξ_b^-," Phys. Rev. Lett. **99**, 052001 (2007) [arXiv:0706.1690 [hep-ex]].

[2] E. E. Jenkins, "Model-Independent Bottom Baryon Mass Predictions in the $1/\mathrm{N}(c)$ Expansion," Phys. Rev. D **77**, 034012 (2008) [arXiv:0712.0406 [hep-ph]].

[3] R. Lewis and R. M. Woloshyn, "Bottom baryons from a dynamical lattice QCD simulation," Phys. Rev. D **79**, 014502 (2009) [arXiv:0806.4783 [hep-lat]].

[4] M. Karliner, B. Keren-Zur, H. J. Lipkin and J. L. Rosner, "The Quark Model and b Baryons," Annals Phys. **324**, 2 (2009) [arXiv:0804.1575 [hep-ph]].

[5] X. Liu, H. -X. Chen, Y. -R. Liu, A. Hosaka and S. -L. Zhu, "Bottom baryons," Phys. Rev. D **77**, 014031 (2008) [arXiv:0710.0123 [hep-ph]].

[6] J. -R. Zhang and M. -Q. Huang, "Heavy baryon spectroscopy in QCD," Phys. Rev. D **78**, 094015 (2008) [arXiv:0811.3266 [hep-ph]].

[7] D. Ebert, R. N. Faustov and V. O. Galkin, "Spectroscopy and Regge trajectories of heavy baryons in the relativistic quark-diquark picture," Phys. Rev. D **84**, 014025 (2011) [arXiv:1105.0583 [hep-ph]].

[8] T. Aaltonen *et al.* [CDF Collaboration], "Observation and mass measurement of the baryon Ξ_b^-," Phys. Rev. Lett. **99**, 052002 (2007) [arXiv:0707.0589 [hep-ex]].

[9] T. A. Aaltonen *et al.* [CDF Collaboration], "Mass and lifetime measurements of bottom and charm baryons in $p\bar{p}$ collisions at $\sqrt{s} = 1.96$ TeV," Phys. Rev. D **89**, 072014 (2014) [arXiv:1403.8126 [hep-ex]].

[10] R. Aaij *et al.* [LHCb Collaboration], "Measurement of the Λ_b^0, Ξ_b^- and Ω_b^- baryon masses," Phys. Rev. Lett. **110**, 182001 (2013) [arXiv:1302.1072 [hep-ex]].

[11] R. Aaij *et al.* [LHCb Collaboration], "Measurement of the Ξ_b^- and Ω_b^- baryon lifetimes," arXiv:1405.1543 [hep-ex].

[12] R. Aaij *et al.* [LHCb Collaboration], "Precision Measurement of the Mass and Lifetime of the Ξ_b Baryon", Phys. Rev. Lett. **113**, 242002 (2014)

[13] T. Aaltonen *et al.* [CDF Collaboration], "Observation of the Ξ_b^0 Baryon," Phys. Rev. Lett. **107**, 102001 (2011) [arXiv:1107.4015 [hep-ex]].

[14] V. M. Abazov *et al.* [DØ Collaboration], "Observation of the doubly strange b baryon Ω_b^-," Phys. Rev. Lett. **101**, 232002 (2008) [arXiv:0808.4142 [hep-ex]].

[15] T. Aaltonen *et al.* [CDF Collaboration], "Observation of the Ω_b^- Baryon and Measurement of the Properties of the Ξ_b^- and Ω_b^- Baryons," Phys. Rev. D **80**, 072003 (2009) [arXiv:0905.3123 [hep-ex]].

[16] T. Dorigo, "Type-I Error or Mass Bias? An Investigation on the Omega(b) Discovery," arXiv:0910.2136 [hep-ex].

[17] V. M. Abazov *et al.* [DØ Collaboration], "Measurement of the Λ_b lifetime in the exclusive decay $\Lambda_b \to J/\psi\Lambda$," Phys. Rev. Lett. **99**, 142001 (2007) [arXiv:0704.3909 [hep-ex]]. DØ Note 6277.

[18] Common Samples Group, Extended AATrack web page `http://www-d0.fnal.gov/Run2Physics/cs/extaa/extaa2.html`

[19] V. M. Abazov *et al.* [DØ Collaboration], "Search for the rare decay $B_s \to \mu\mu$," Phys. Rev. D **87**, 072006 (2013) [arXiv:1301.4507 [hep-ex]]. DØ Note 6371.

[20] J. Beringer et al. (Particle Data Group), Phys. Rev. D **86**, 010001 (2012) and 2013 partial update for the 2014 edition.

[21] Hoecher *et al*, Toolkit for Multivariate Data Analysis with ROOT, version 4.1.0 `http://tmva.sourceforge.net/`, 2010.

[22] See internal DØ talk by Andres Garcia during B group meeting on 18 October 2012, slide 18.

[23] Private communication by G. Borissov, DØ collaboration member and author of the tracking and alignment code.

[24] Abazov et al, *The Upgraded DØ Detector* , Nuclear Instruments and Methods in Physics Research, **A565**, 2006, 463-357

[25] D.B. Lichtemberg *Unitary symmetry and elementary particles*, Academic Press, 1970

[26] N. Isgur and M. B. Wise, Phys. Lett. B **232**, 113 (1989); **237**, 527 (1990).

[27] R. Dashen and A. V. Manohar, Phys. Lett. B **315**, 425 (1993); **315**, 438 (1993).

[28] E. E. Jenkins, Phys. Rev. D **54**, 4515 (1996).

[29] E. E. Jenkins, Phys. Rev. D **55**, R10 (1997).

[30] P. Nelson, S. Dawson and R. K. Ellis, Nucl. Phys. **B303**, 607 (1988)

[31] J. L.Rosner, Phys. Rev. D **90**, 014023 (2014).

[32] V. M. Abazov *et al.* (DØ Collaboration), Measurement of the Forward-Backward Asymmetry in the Production of $B^{\pm}$ Mesons in $p\bar{p}$ Collisions at $\sqrt{s} = 1.96$ TeV. Phys. Rev. Lett. **114**, 051803 (2015)

[33] V. M. Abazov *et al.* (DØ Collaboration), Nucl. Instrum. Methods Phys. Res. A **565**, 463 (2006).

[34] V. M. Abazov *et al.* (DØ Collaboration), Nucl. Instrum. Methods Phys. Res. A **552**, 372 (2005).

[35] K. A. Olive *et al.* Chin. Phys. C **38**, 090001 (2014).

[36] T. Sjöstrand *et al.*, Comp. Phys. Commun. **135**, 238 (2001).

[37] S. Frixione and B.R. Webber, J. High Energy Phys. 06 (2002) 029; S. Frixione, P. Nason, and B.R. Webber, J. High Energy Phys. 08 (2003) 007.

[38] J. Pumplin *et al.*, J. High Energy Phys. 07 (2002) 012; D. Stump *et al.*, J. High Energy Phys. 10 (2003) 046.

[39] G. Corcella, J. High Energy Phys. 01 (2001) 010.

[40] D.J. Lange, Nucl. Instrum. Meth. Phys. Res. A **462**, 152 (2001).

[41] R. Brun and F. Carminati, CERN Program Library Long Writeup No. W5013, 1993 (unpublished).

[42] S. Frixione and B.R. Webber, J. High Energy Phys. 06 (2002) 029; S. Frixione, P. Nason , and B.R. Webber, J. High Energy Phys. 08 (2003) 007.

[43] W. K. Lai and A. K. Leibovich, Λ_c^+/Λ_c^- and $\Lambda_b^0/\bar{\Lambda}_b^0$ production asymmetry at the LHC from heavy quark recombination, Phys. Rev. D **91**, 054022 (2015); (private communications).

[44] S. Chatrchyan *et al.* (CMS Collaboration), Phys. Lett. B714 (2012) 136.

[45] (LHCb Collaboration) aLHCb-CONF-2012-031.

Apendix A $N(\text{tracks}) < 300$ Requirement

As mentioned in Section 5.1.3, one of the requirements at preselection is that all events containing in excess of 300 tracks are removed from consideration. This is an unusual cut, because in general one would expect events with different multiplicities to have a similar probability of containing a signal candidate, assuming that the trigger efficiencies for $J/\psi \to \mu\mu$ decays are not heavily impacted by the instantaneous luminosity. However, we observe that applying this cut has a very small effect on the yields of Ξ^- candidates in data, for events containing a J/ψ meson; we infer that any change in the $\Xi_b^- \to J/\psi\Xi^-$ yield is similarly small.

Figures 1 and 2 shows the invariant mass distributions for Λ^0 and Ξ^- candidates, for Run IIa and Run IIb samples, before and after applying the $N(\text{tracks})$ cut. The reductions in yields are as follows:

- Λ^0(IIa): 2407 $\to$ 2291 (0.5% signal reduction);
- Λ^0(IIb): 6894 $\to$ 6334 (8.1% signal reduction);
- Ξ^-(IIa): 1622 $\to$ 1592 (1.8% signal reduction);
- Ξ^-(IIb): 4220 $\to$ 4182 (0.9% signal reduction).

The corresponding reduction in the background, in the training sample of sidebands plus wrong-sign events, is

- BG(IIa): 5743 $\to$ 4687 (18% background reduction);
- BG(IIb): 54162 $\to$ 28909 (46% background reduction).

A.1 Why are there so few signal candidates in high-multiplicity events?

The most likely explanation for the stability of the signal, and the large reduction in background, is that the overall signal efficiency for events with more than 300 tracks is highly suppressed. In other words, these signal candidates have already been lost at some earlier point in the reconstruction, and hence the efficiency of the $N(\text{tracks}) < 300$ requirement *with respect to the pre-cut sample* is very large.

In turn, a plausible reason for the low reconstruction efficiency of the signal events in high track-multiplicity events is as follows. In the track reconstruction, limits are placed on the number of non-unique hits that can be used to define a track: any hit that it used in more than one track is called a 'shared hit', and there are several requirements limiting the number of shared hits allowed for a track. These criteria include tests like $N_{\text{shared}} < \frac{2}{3}N_{\text{total}}$, and ($N_{\text{shared}} < \frac{1}{5}N_{\text{total}}$ or $N_{\text{total}} - N_{\text{shared}} \geq 4$). Clearly, as the overall track multiplicity increases, the fraction of shared hits rises, and these requirements become less efficient for any particular track. This effect will be more pronounced for high luminosity data, but

will also be worsened by the application of the extended tracking algorithm, which adds a new set of tracks to those found by the default tracking system. Finally, this inefficiency will be far worse for signal channels with multiple tracks in the final state, such as these five-track b baryon decays.

A.2 Modelling the effect of this cut

While this effect will reduce the overall efficiency for reconstructing b baryons, it is in a sense a 'stable' inefficiency, which was already present in the earlier publications, and so will not significantly change the performance of this new analysis with respect to the previous ones. If we accept this as an irreducible loss in the signal yield, then the only remaining issue is to model its effect, in subsequent conversions of the signal yields into physically meaningful production fractions times branching ratios.

However, this raises a second problem, namely that the MC simulation cannot model the $N(\text{tracks})$ distribution observed for data, even with the proper zero bias overlays included. Figure 3 compares the track multiplicity for data and MC, for both Run IIa and Run IIb, and clearly demonstrates a stunning underestimation of the number of tracks in the simulation. This type of mismodelling has been observed in previous analyses, and it doesn't appear to adversely affect the agreement of other variables (e.g. kinematics, lifetimes, or even track isolation), but clearly the MC cannot be used to estimate the efficiency of the $N(\text{tracks}) < 300$ cut.

The comparison in Fig. 3 is not really fair, since the MC sample comprises pure Ξ_b^- signal events, while the data will be dominated by other sources. In particular, the signal events in data will be triggered with muon triggers, while many background events will have passed jet triggers that tend to preferentially accept higher multiplicity events. However, there is still clear mismodelling. The likely reason [23] is that the ZB events from data are overlaid onto the simulated collisions by adding the hits at the same coordinates as found in data, before running the track reconstruction algorithm. This is not quite right, since the MC uses a different (simplified) detector geometry that doesn't take into account all the alignment effects in the real detector. Hence a particular track from ZB data might not be reconstructed in MC, due to having too poor a fit quality.

Instead of using the simulation to measure the efficiency of this cut, with respect to the sample with all other requirements applied, we use the yield of Ξ^- (and ultimately Ω^-) candidates from data, in events containing a J/ψ candidate passing our cuts. This relies on two assumptions, stated here for completeness: (1) the track multiplicity distribution for events containing $\Xi_b^- \to J/\psi\Xi^-$ candidates is the same as for a generic event containing $J/\psi + \Xi^-$ candidates (but which might not be from Ξ_b^- decay); (2) The efficiency to reconstruct a Ξ_b^- baryon by combining the J/ψ and Ξ^- candidates is independent of the track multiplicity. This second assumption is very likely to be true, since the ineficiency of the track multiplicity cut is introduced at the track reconstruction level, not in the combination of daughters into parents. Furthermore, note that this analysis doesn't aim to measure any absolute efficiencies, rather it uses relative efficiencies, and so in fact we

only require that the above assumptions are equally valid for the topologically identical decays of Ξ_b^- and Ω_b^- baryons.

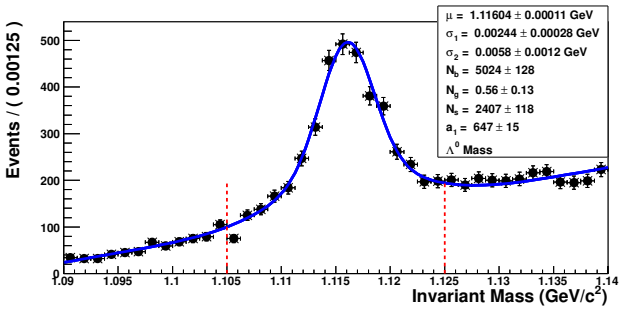

(a) $M(\Lambda^0)$ (Run IIa, before $N(\text{tracks}) < 300$ cut).

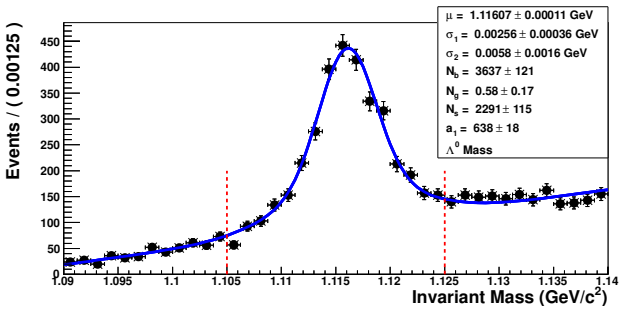

(b) $M(\Lambda^0)$ (Run IIa, after $N(\text{tracks}) < 300$ cut).

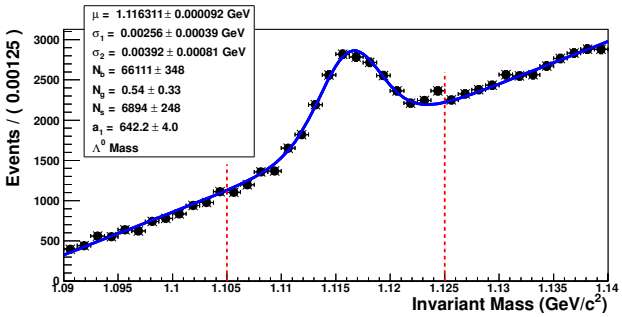

(c) $M(\Lambda^0)$ (Run IIb, before $N(\text{tracks}) < 300$ cut).

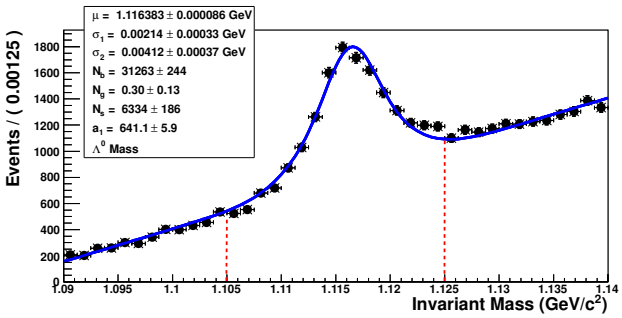

(d) $M(\Lambda^0)$ (Run IIb, after $N(\text{tracks}) < 300$ cut).

Figure 1: Λ^0 invariant mass distributions before and after applying the $N(\text{tracks}) < 300$ requirement (filled circles). Also shown are the results of fits to the data to extract the yields (solid lines). The dashed vertical lines demarcate the mass windows used to define the preselection sample. The yields before and after the cut are compared in the text.

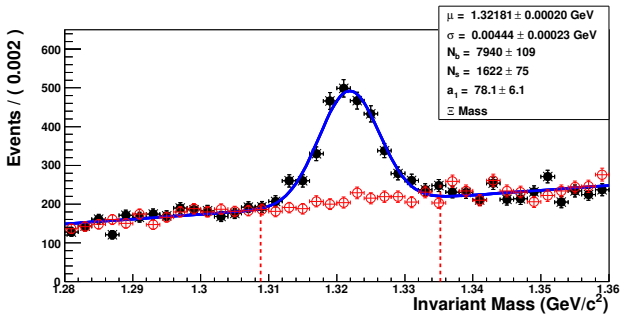

(a) $M(\Xi^-)$ (Run IIa, before $N(\text{tracks}) < 300$ cut).

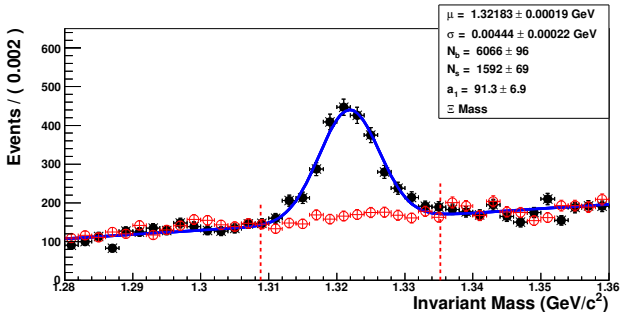

(b) $M(\Xi^-)$ (Run IIa, after $N(\text{tracks}) < 300$ cut).

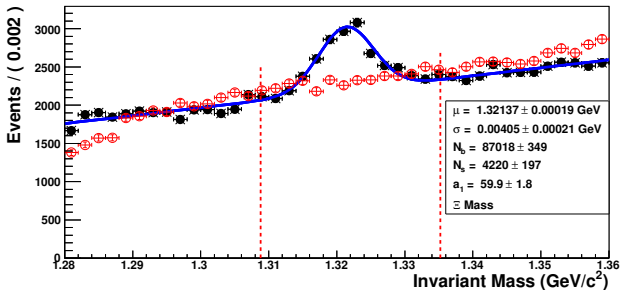

(c) $M(\Xi^-)$ (Run IIb, before $N(\text{tracks}) < 300$ cut).

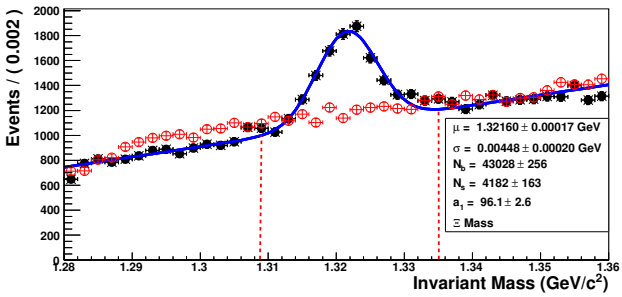

(d) $M(\Xi^-)$ (Run IIb, after $N(\text{tracks}) < 300$ cut).

Figure 2: Ξ^- invariant mass distributions before and after applying the $N(\text{tracks}) < 300$ requirement (filled circles). Also shown are the results of fits to the data to extract the yields (solid lines), the wrong-sign distribution is also plotted (empty circles). The dashed vertical lines demarcate the mass windows used to define the preselection sample. The yields before and after the cut are compared in the text.

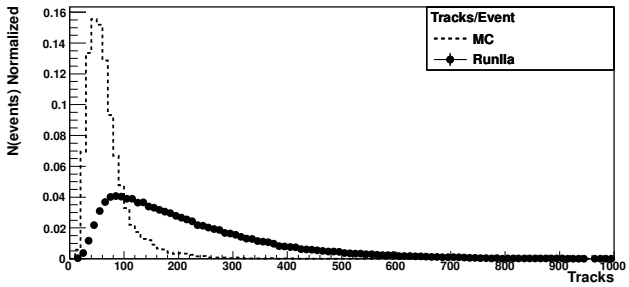

(a) Run IIa.

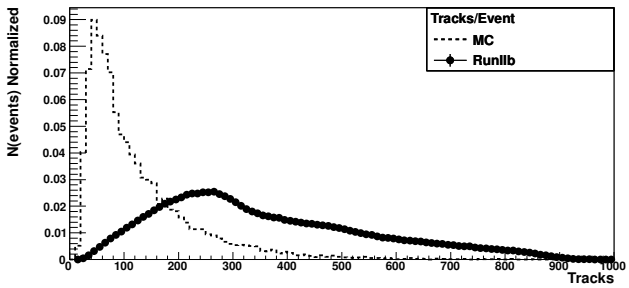

(b) Run IIb.

Figure 3: Number of tracks per event, comparing data (black markers) and MC simulation (dashed line), for both Run IIa and Run IIb. The mismodelling is clear, with far fewer tracks in a typical MC event than are observed in real data.

Apendix B Estimating the Ξ_b^- preselection yields

In order to optimize the search and establish a Ξ_b^- signal, we need some estimate of the number of signal events in the preselection sample. The Ξ_b^- yield will itself give a direct normalization for use in the Ω_b^- search. However, there is no reference channel for the Ξ_b^- case, and so we instead use the existing yield from the published analysis of Run IIa data to give a first estimate of the yield [1].

The published DØ analysis reported $15.2 \pm 4.4^{+1.9}_{-0.4}$ Ξ_b^- events in the Run IIa sample. To estimate the corresponding expected yield at preselection, we use the ratio of efficiencies for the published selection requirements ('PRL cuts') and the preselection requirements, as determined from the Run IIa MC simulation, i.e.

$$N(\Xi_b^-, \text{preselection}) \;=\; N(\Xi_b^-, \text{PRL cuts}) \cdot \frac{\varepsilon(\Xi_b^-, \text{preselection})}{\varepsilon(\Xi_b^-, \text{PRL cuts})} \cdot \varepsilon^{\text{DQ}}, \qquad (1)$$

where ε^{DQ} is the efficiency of the data quality requirements (0.95 for Run IIa), which weren't included in the PRL selection. The ratio of selection efficiencies from MC ensures the cancellation of effects due to, for example, the determination of integrated luminosity, muon ID efficiency, and track reconstruction efficiency. From the Run IIa MC sample, the PRL and preselection cuts give signal yields of 2 930 and 13 980, respectively, giving an efficiency ratio of 4.8. Substituting the numbers into Eq. (1), the estimated Run IIa preselection yield is 69 ± 22, with the uncertainty dominated by the quoted PRL yield.

Both the PRL and the preselection requirements include the $N(\text{tracks}) < 300$ cut, but the efficiency of this cut may be different for the 2007 (PRL) and 2011 (this analysis) versions of the extended tracking algorithm. In particular, the 2011 version merges the track lists determined from the default and extended tracking algorithms, while the 2007 version only retains the tracks from the extended algorithm. As such, the 2007 data has a lower mean track multiplicity, and so the signal loss from hit 'saturation' should be smaller (see Appendix A for a discussion of this effect). To quantify this, we apply the PRL cuts to the Run IIa 2011 data, and obtain a signal yield of 10.8 ± 4.1 events [22], significantly less than the 15.2 ± 4.4 events from the 2007 sample. We ascribe this difference to the overall change in the tracking algorithm, including, but not necessarily limited to, the lower efficiency of the $N(\text{tracks}) < 300$ cut. As the 2011 sample is used in this present analysis, we rescale the expected preselection yield (and uncertainty) to account for the observed reduction in the PRL cuts yield from 15.2 to 10.8 events, giving an expected preselection yield in Run IIa of 49 ± 16 events.

When the Run IIa data is examined, after training a preliminary multivariate discriminant (see next section) the observed yield is significantly lower than that expected from the above prediction, corresponding to an actual preselection yield of 15 events (around 2σ below the above expectation). While a small effect might be expected from possible Monte Carlo mismodelling, the most likely explanation is that the original signal peak was enhanced by an underlying background fluctuation. Regardless of the source of this discrepancy, having examined the Run IIa data we now have a direct extraction of the

signal yield, and we use this value instead for optimizing the event selection.

To extrapolate into the Run IIb period and estimate a preselection signal yield for this epoch, we use the following relation:

$$N(\Xi_b^-,\,\mathrm{IIb}) \;=\; N(\Xi_b^-,\,\mathrm{IIa}) \cdot \frac{N^{\mathrm{IIb}}(J/\psi)}{N^{\mathrm{IIa}}(J/\psi)} \cdot \frac{F^{\mathrm{IIb}}(J/\psi \text{ from } \Xi_b^-)}{F^{\mathrm{IIa}}(J/\psi \text{ from } \Xi_b^-)} \cdot \frac{\varepsilon^{\mathrm{IIb}}(\Xi_b^-|J/\psi)}{\varepsilon^{\mathrm{IIa}}(\Xi_b^-|J/\psi)}. \quad (2)$$

The first fraction is simply of the number of J/ψ candidates reconstructed in the Run IIa ($4\,150\,339 \pm 5\,196$) and Run IIb ($24\,182\,140 \pm 13\,948$) data samples, as given in Section 5.1.1. In the second fraction, the quantity $F^{\mathrm{IIx}}(J/\psi \text{ from } \Xi_b^-)$ is the fraction of reconstructed J/ψ mesons that are produced from Ξ_b^- decays. One can imagine a scenario where the trigger conditions changed so as to enhance, for example, the relative acceptance of prompt J/ψ compared to those from b hadron decay. There is no evidence of any significant shift in the J/ψ properties from Run IIa to Run IIb, so we assume that this term is exactly unity for the purposes of the estimation.

The third term is the ratio of preselection efficiencies from MC, for the IIa and IIb ($q\bar{q}$) samples, given that the J/ψ is properly reconstructed. We know from previous analyses that the track reconstruction efficiency for low-momentum particles produced away from the PV diminished over time, as the detector aged, and so expect this ratio to be significantly less than one. For Run IIa, the efficiency from MC is $13\,980/236\,742 = 5.91\%$, for Run IIb the value is $10\,687/651\,063 = 1.64\%$, giving a ratio of 0.28. We allow for possible epoch-dependent mismodelling of the single track reconstruction efficiency in MC, with MC/data efficiency ratios determined for Run IIa and Run IIb using $B^+ \to J/\psi K^+$ and $B^0 \to J/\psi K^{*0}(892)$ decays [19]. The ratios are determined to be 0.879 ± 0.006 for Run IIa and 0.884 ± 0.004 for Run IIb, giving an overall effect for the three hadron tracks of $(0.884/0.879)^3 = 1.017 \pm 0.014$. This is completely consistent with unity, and so we neglect this effect.

Based on the findings presented in Appendix A, namely that the Ξ^- yield reduction in data due to the $N(\mathrm{tracks}) < 300$ cut is consistent for Run IIa and Run IIb samples, we do not apply any additional correction to account for this cut.

Putting in the numbers, Eq. (2) becomes

$$\begin{aligned} N(\Xi_b^-,\,\mathrm{IIb}) &= 15 \times 5.8 \times 1.0 \times 0.28 \\ &= 25 \pm 9, \end{aligned} \quad (3)$$

where the uncertainty is completely dominated by the Run IIa yield measurement. This number is the expected preselection yield in Run IIb, which will be used in the optimization of the multivariate event selection.

Apendix C Distributions of BDT Input Variables

The individual variables used in the $\mathrm{BDT}^{42}_{\Xi_b}$ discriminant are listed in order of importance in Table 1. The importance is derived by counting how often the variables are used to make a decision, and weighting each decision by the separation-gain squared it achieves and by the number of events in the node [21].

Ranking	variable	category	particle	importance
1	$\tau(\Xi^-)$	lifetime	Ξ^-	1.233e-01
2	$\tau(\Lambda^0)$	lifetime	Λ^0	1.103e-01
3	$\cos(\theta_{\Xi^-})$	pointing angle	Ξ^-	8.197e-02
4	$L_{xy}(\Xi^-)$	lifetime	Ξ^-	5.517e-02
5	$\tau^{\rm sig}(\Lambda^0)$	lifetime	Λ^0	5.345e-02
6	$p_T(\Xi_b^-)$	momentum	Ξ_b^-	5.319e-02
7	$p_T(\pi_\Xi)$	momentum	π_Ξ	3.604e-02
8	$M(\Lambda^0)$	mass	Λ^0	3.042e-02
9	$M(\Xi^-)$	mass	Ξ^-	2.914e-02
10	$\chi^2_{\rm PV\to}(p)$	PV consistency	p	2.905e-02
11	$\tau^{\rm sig}(\Xi^-)$	lifetime	Ξ^-	2.434e-02
12	$\chi^2_{\rm PV\to}(\Xi^-)$	PV consistency	Ξ^-	2.243e-02
13	$\chi^2_{\rm PV\to}(\pi_\Lambda)$	PV consistency	π_Λ	2.229e-02
14	$p_T(\mu_2)$	momentum	μ_2	2.224e-02
15	${\rm IP}^{\rm sig}(\mu_2)$	IP significance	μ_2	1.961e-02
16	$I(J/\psi)$	isolation	J/ψ	1.924e-02
17	$\cos(\theta_{\Xi_b^-})$	pointing angle	Ξ_b^-	1.714e-02
18	$p_T(p)/p_T(\pi)$	momentum	Λ^0	1.711e-02
19	$I(\Xi^-)$	isolation	Ξ^-	1.650e-02
20	${\rm IP}^{\rm sig}(\mu_1)$	IP significance	μ_1	1.617e-02
21	$\chi^2_{\rm PV\to}(\mu_2)$	PV consistency	μ_2	1.552e-02
22	${\rm IP}^{\rm sig}(\pi_\Xi$	IP significance	π_Ξ	1.477e-02
23	$L_{xy}(\Lambda^0)$	lifetime	Λ^0	1.378e-02
24	$p_T(\pi_\Lambda)$	momentum	π_Λ	1.371e-02
25	$p_T(\Xi^-)$	momentum	Ξ^-	1.347e-02
26	$\cos(\theta_{\Lambda^0})$	pointing angle	Λ^0	1.342e-02
27	$\chi^2_V(J/\psi)$	vertex fit	J/ψ	1.271e-02
28	$\chi^2_V(\Lambda^0)$	vertex fit	Λ^0	1.255e-02
29	${\rm IP}^{\rm sig}(p)$	IP significance	p	1.179e-02
30	$I(\mu_2)$	isolation	μ_2	1.098e-02
31	$\chi^2_V(\Xi^-)$	vertex fit	Ξ^-	9.835e-03
32	$\chi^2_{\rm PV\to}(\mu_1)$	PV consistency	μ_1	9.530e-03
33	$I(\mu_1)$	isolation	μ_1	8.831e-03
34	$\chi^2_V(\Xi_b^-)$	vertex fit	Ξ_b^-	6.958e-03
35	$p_T(\Lambda^0)$	momentum	Λ^0	5.258e-03
36	${\rm IP}^{\rm sig}(\Xi^-)$	IP significance	Ξ^-	5.045e-03
37	$I(\Lambda^0)$	isolation	Λ^0	4.957e-03
38	$I(p)$	isolation	p	4.954e-03
39	$p_T(J/\psi)$	momentum	J/ψ	4.678e-03
40	${\rm IP}^{\rm sig}(J/\psi)$	IP significance	J/ψ	4.144e-03
41	${\rm IP}^{\rm sig}(\pi_\Lambda$	IP significance	π_Λ	2.452e-03
42	$I(\pi_\Lambda)$	isolation	π_Λ	1.553e-03

Table 1: Ranked list of input variables used in the BDT[42] discriminant. The variable definitions are given in the text.

The individual distributions of signal and background events, for each input variable, are given in Figs. 4–7 for the Ξ_b^- channel, and in Figs. 8–11 for the Ω_b^- channel.

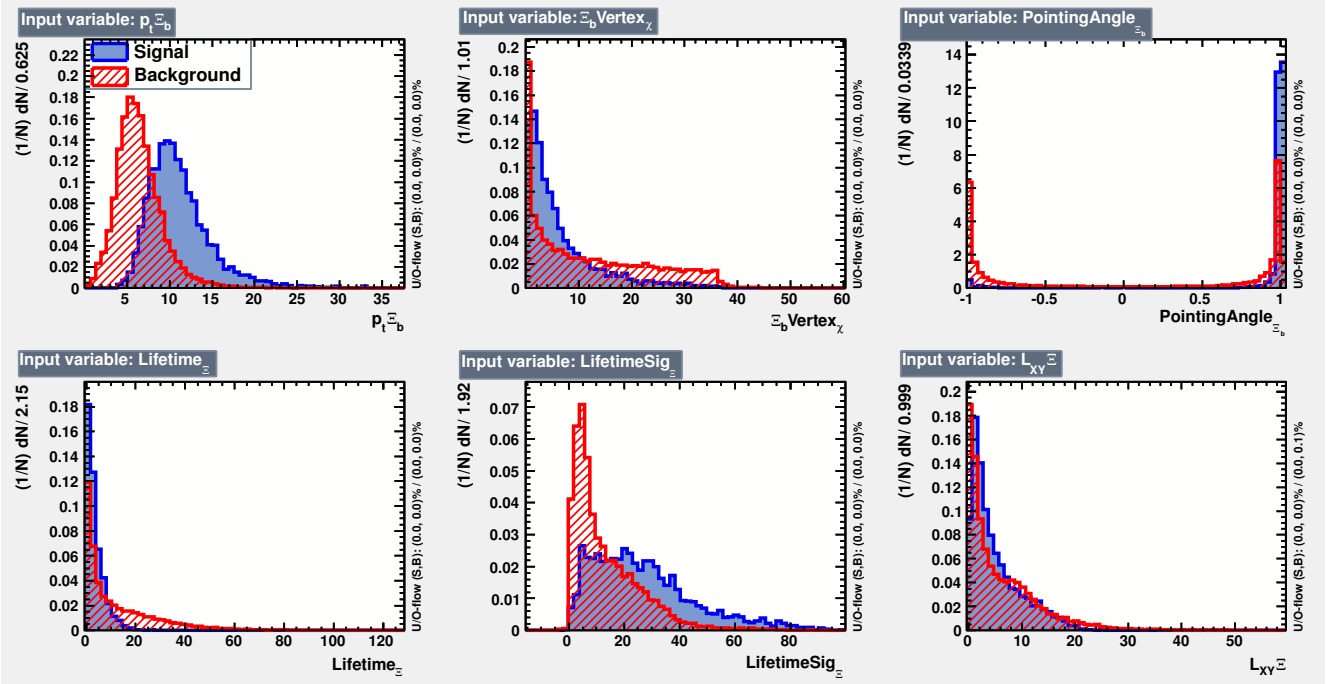

(a) variables 1–6

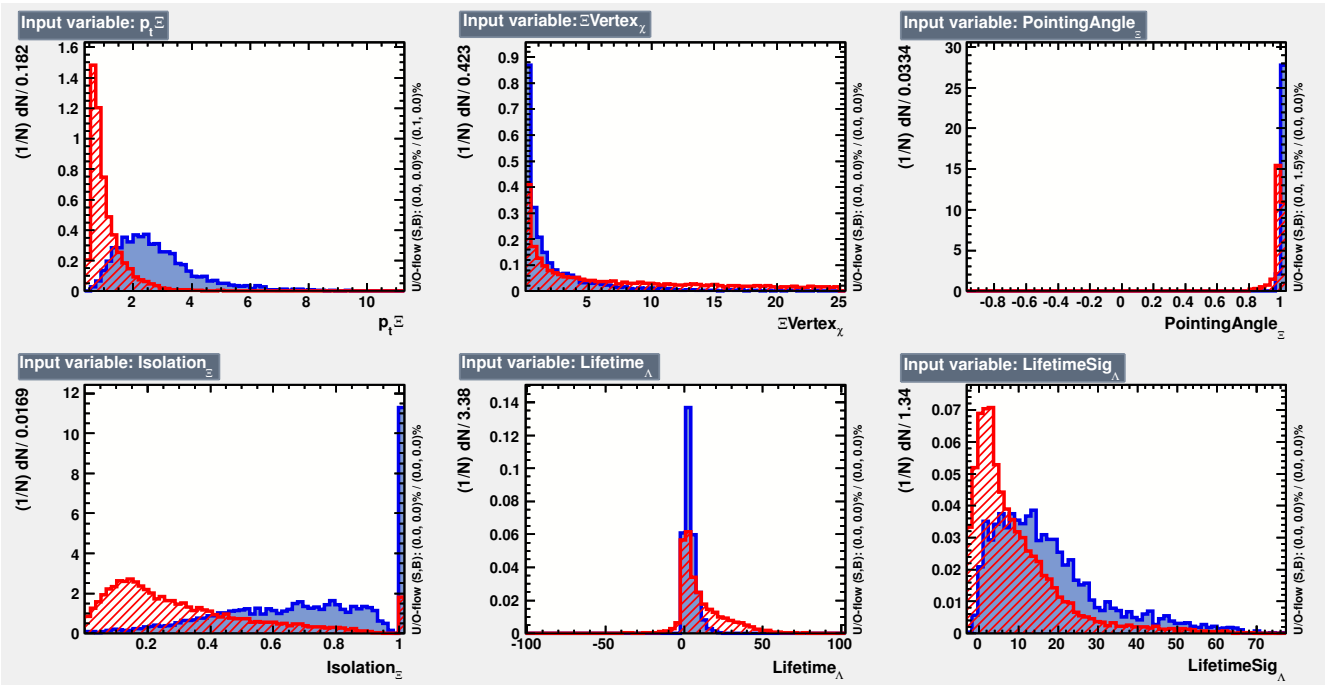

(b) variables 7–12

Figure 4: Ξ_b^- Signal and background distributions for input variables 1–12 included in the BDT[42] discriminant.

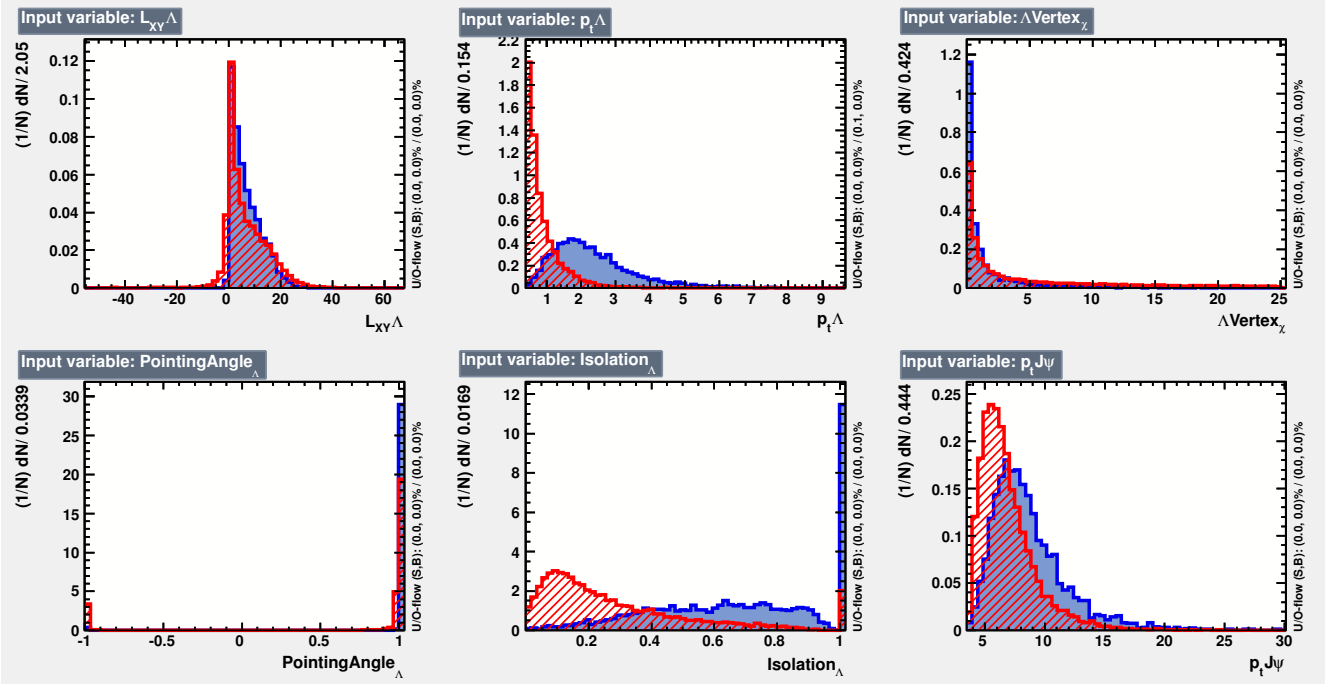

(a) variables 13–18

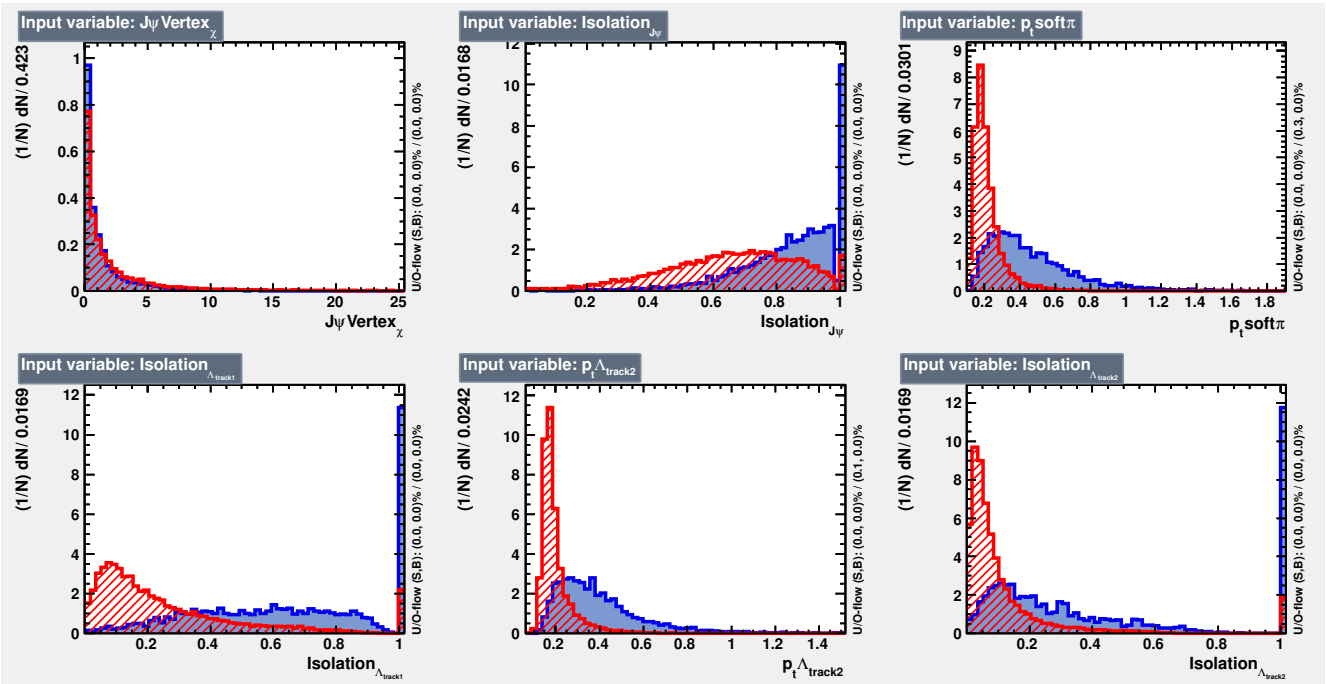

(b) variables 19–24

Figure 5: Ξ_b^- Signal and background distributions for input variables 13–24 included in the BDT[42] discriminant.

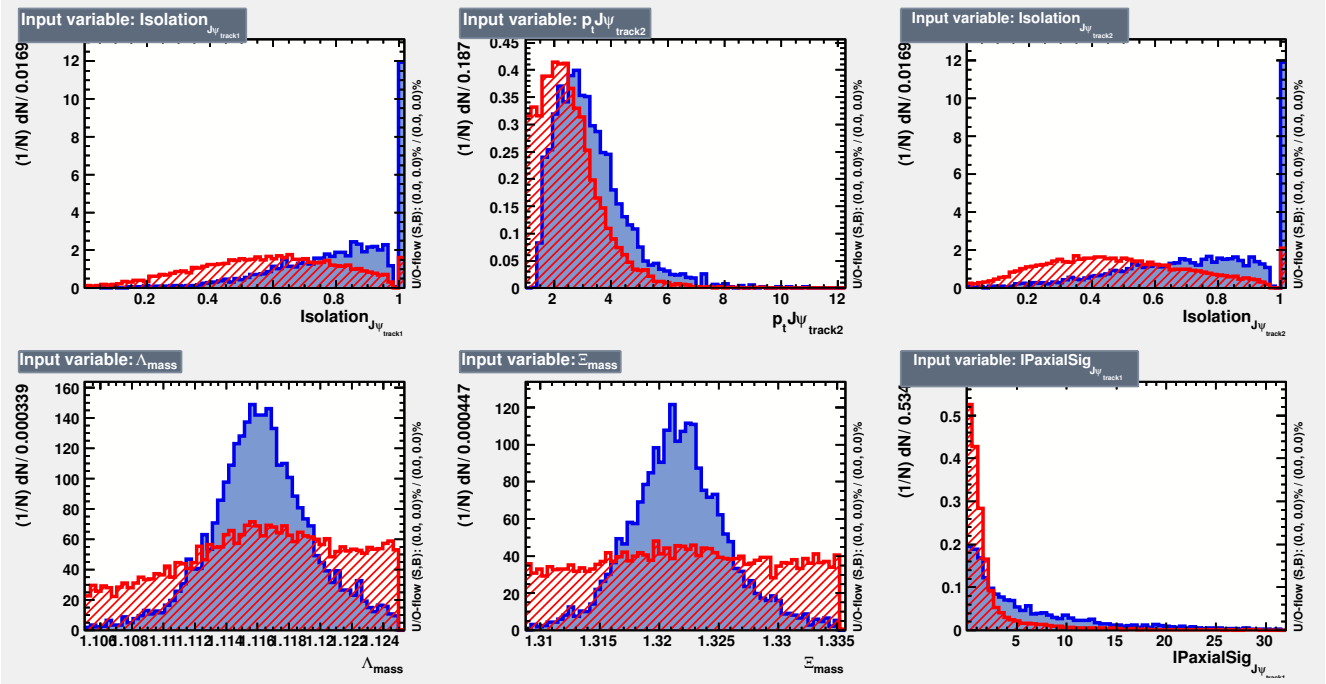

(a) variables 25–30

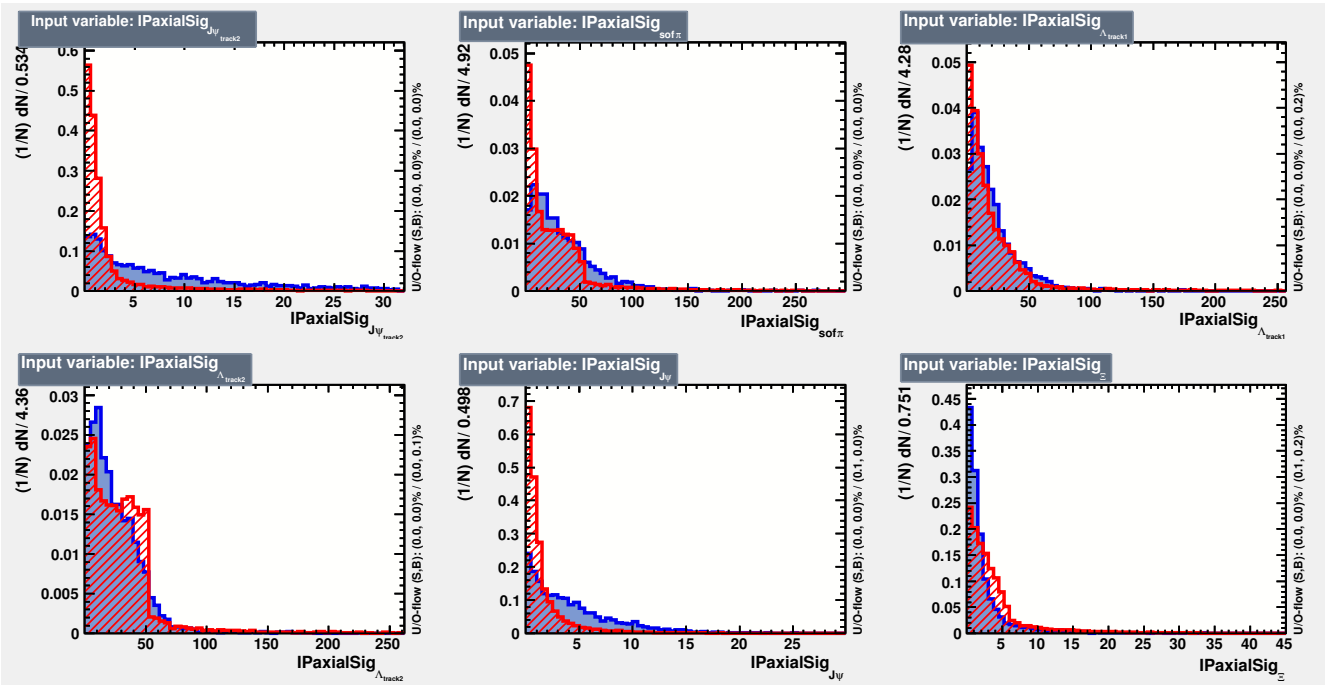

(b) variables 31–36

Figure 6: Ξ_b^- Signal and background distributions for input variables 25–36 included in the BDT[42] discriminant.

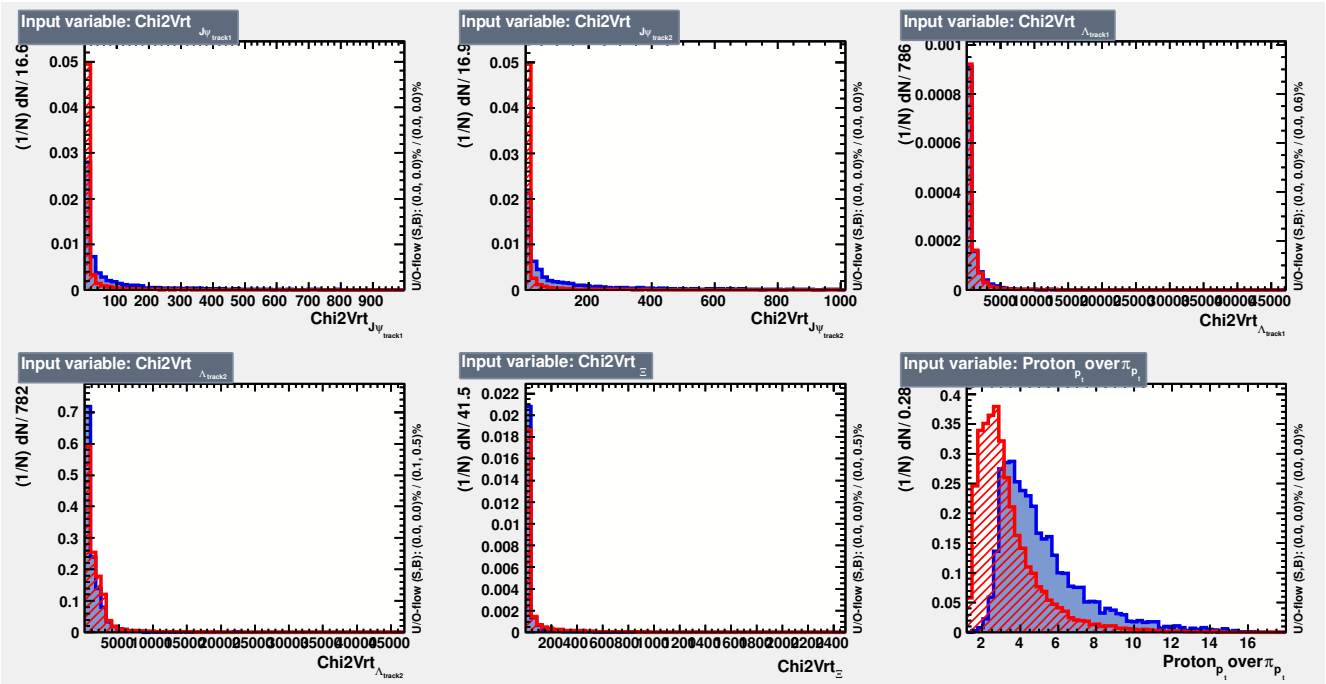

(a) variables 37–42

Figure 7: Ξ_b^- Signal and background distributions for input variables 37–42 included in the BDT[42] discriminant.

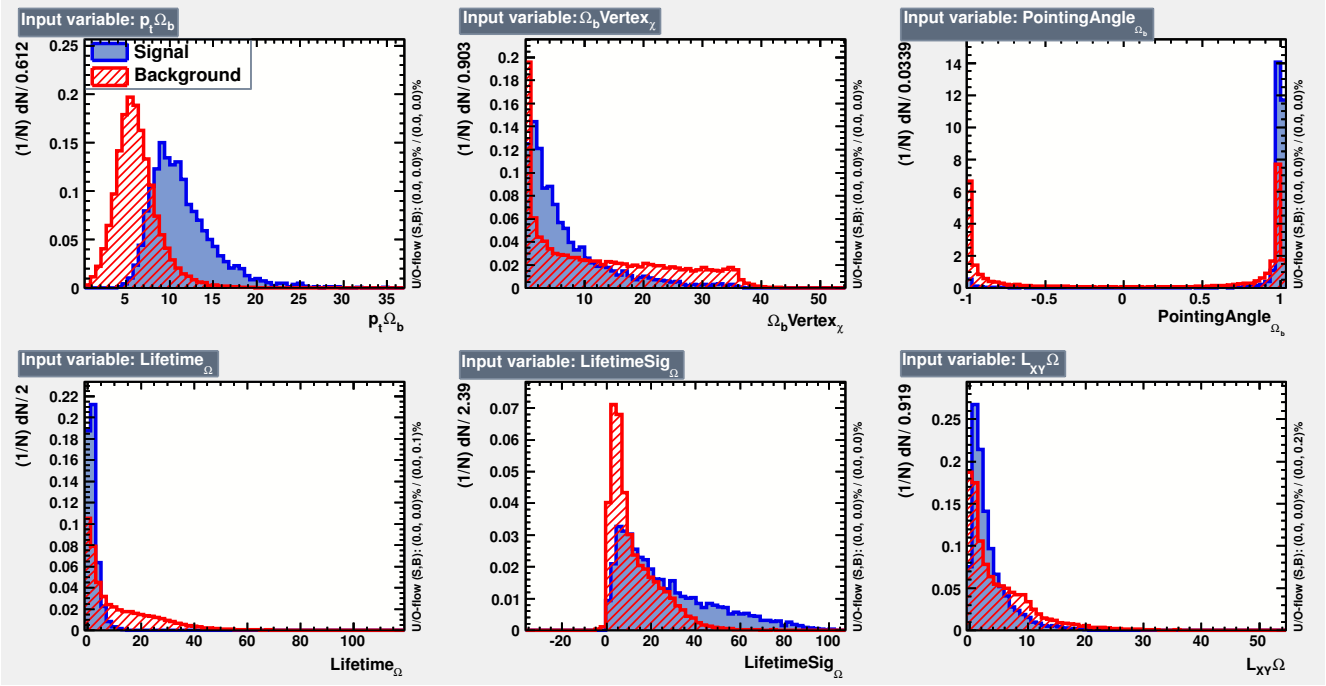

(a) variables 1–6

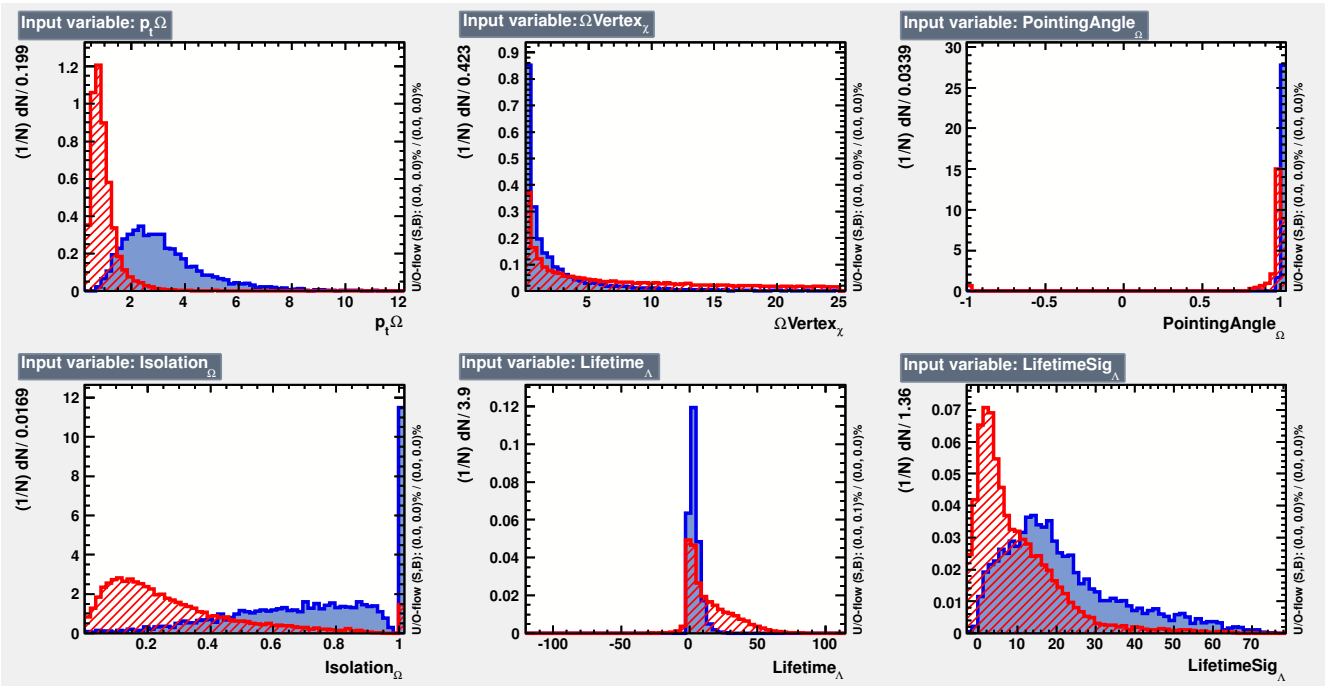

(b) variables 7–12

Figure 8: Ω_b^- Signal and background distributions for input variables 1–12 included in the BDT[42] discriminant.

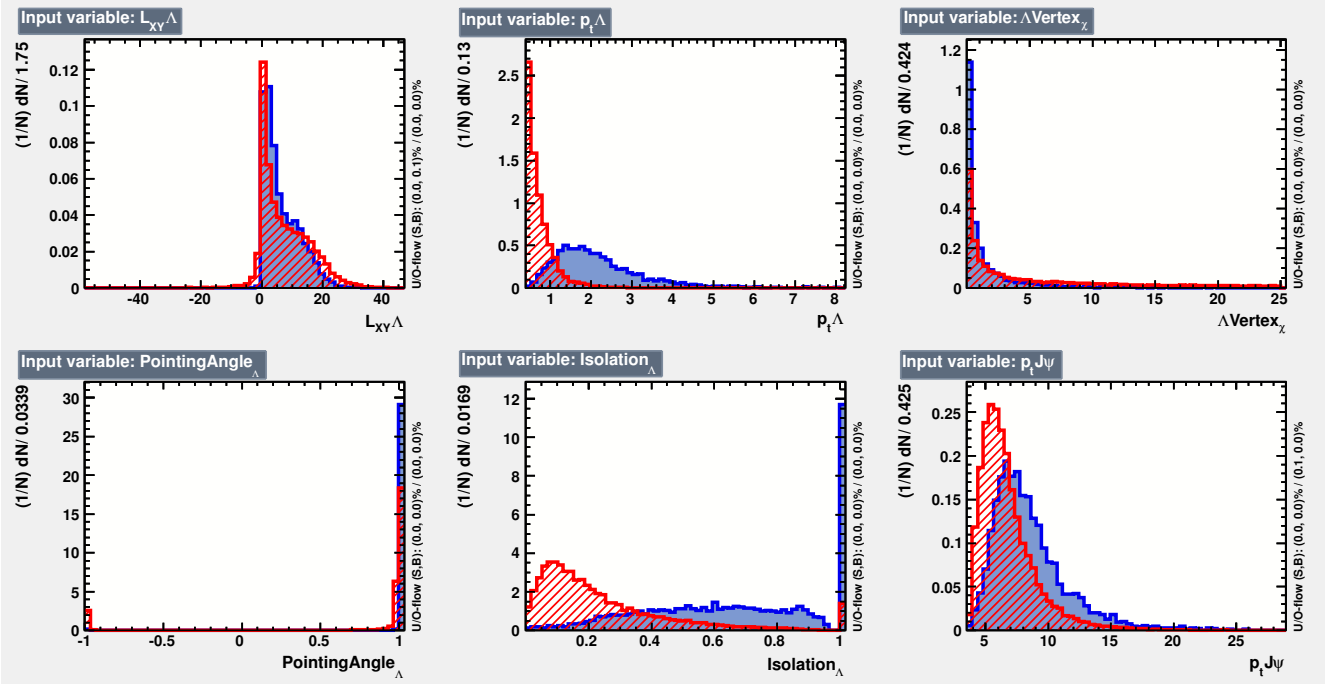

(a) variables 13–18

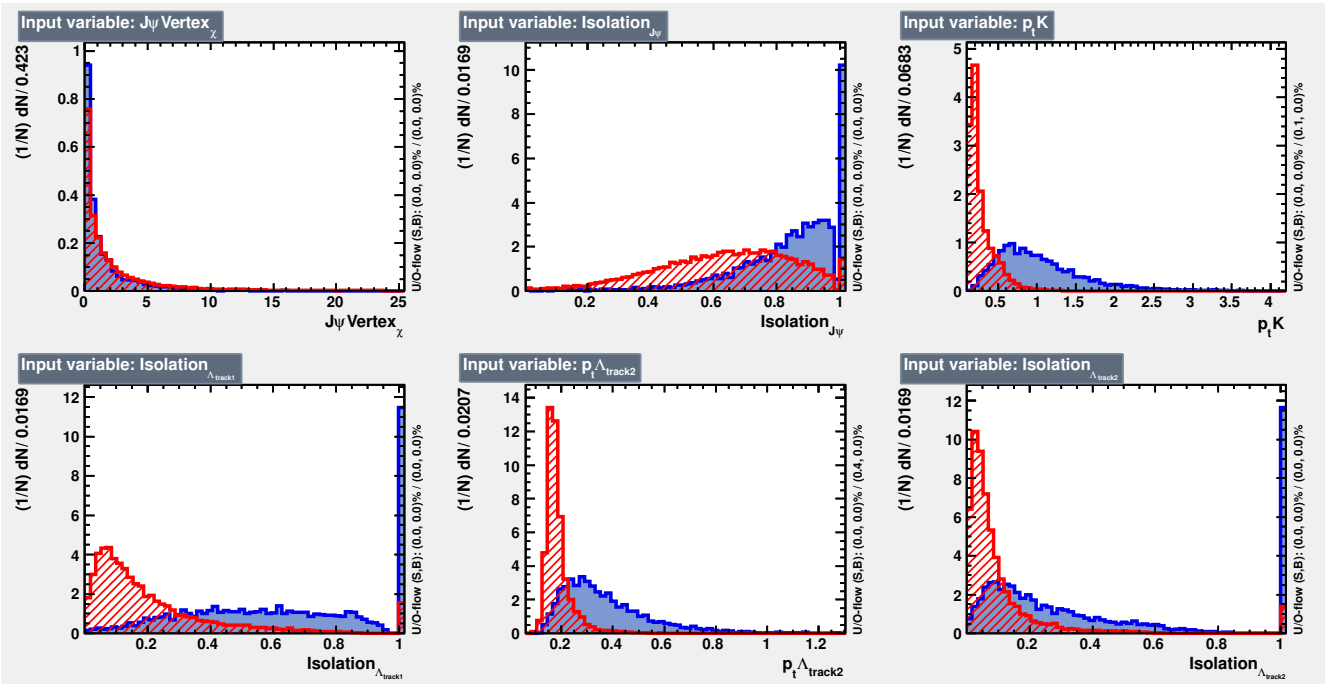

(b) variables 19–24

Figure 9: Ω_b^- Signal and background distributions for input variables 13–24 included in the BDT[42] discriminant.

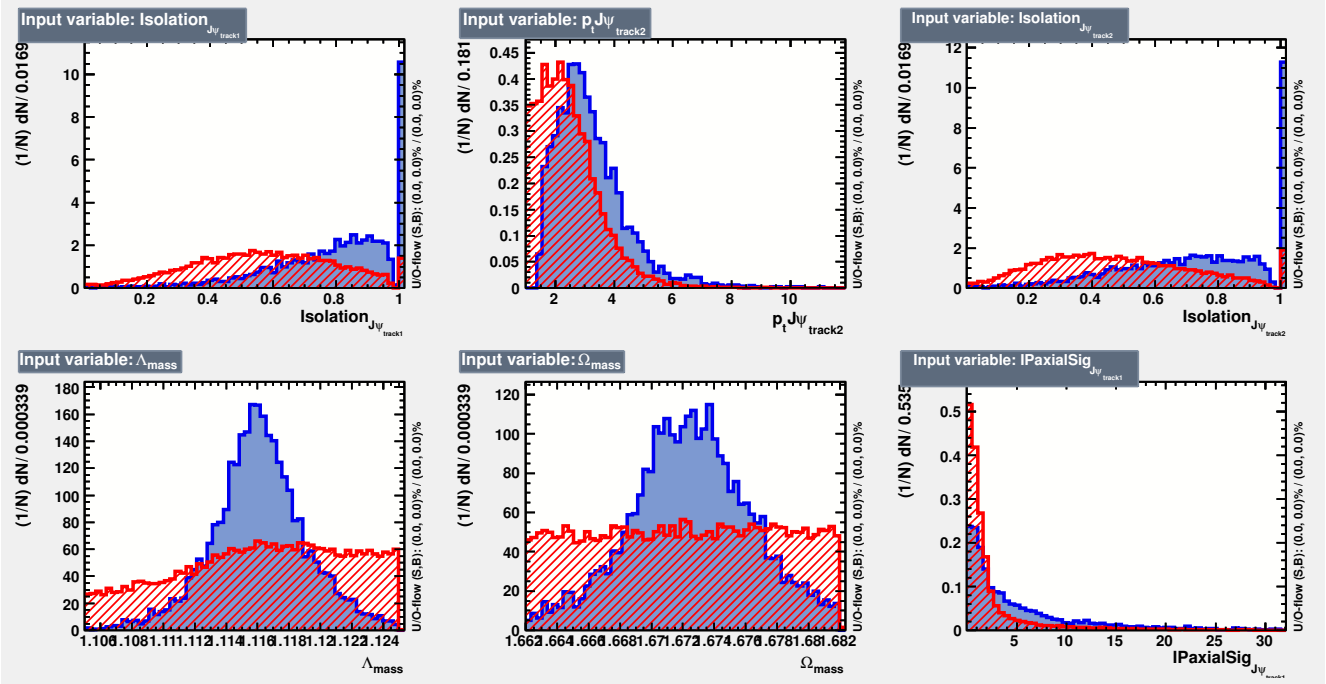

(a) variables 25–30

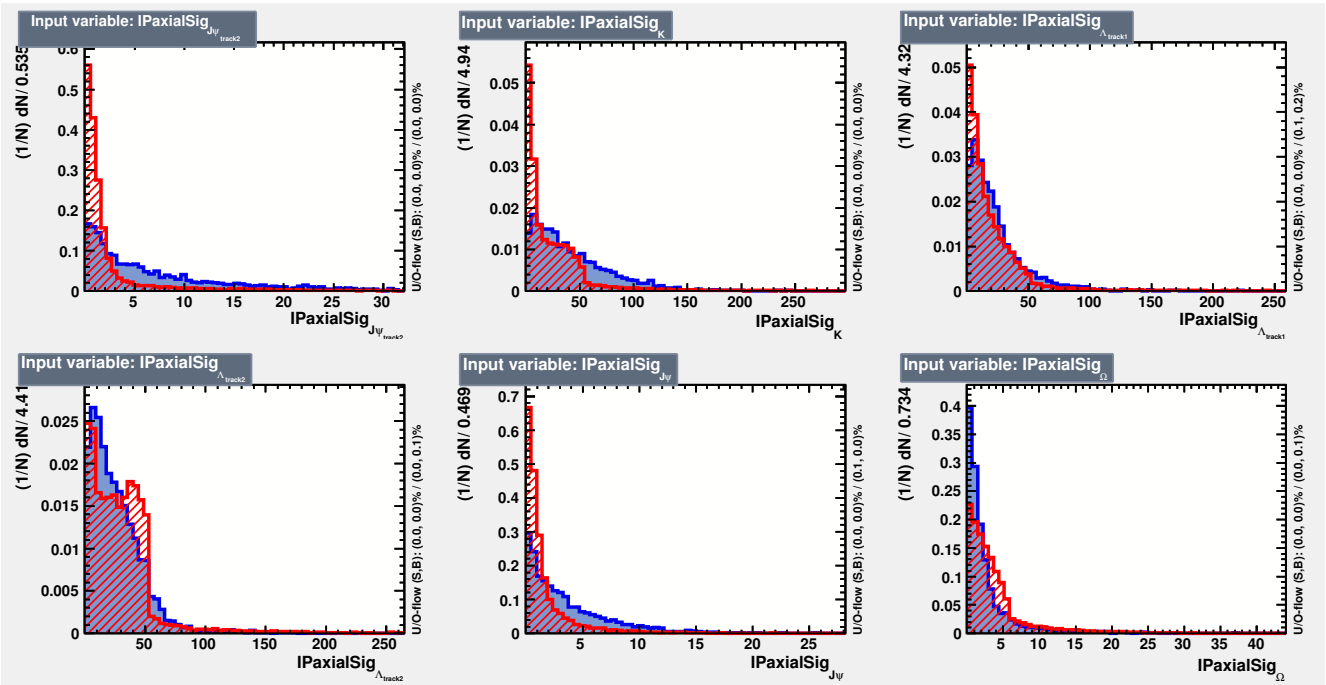

(b) variables 31–36

Figure 10: Ω_b^- Signal and background distributions for input variables 25–36 included in the BDT[42] discriminant.

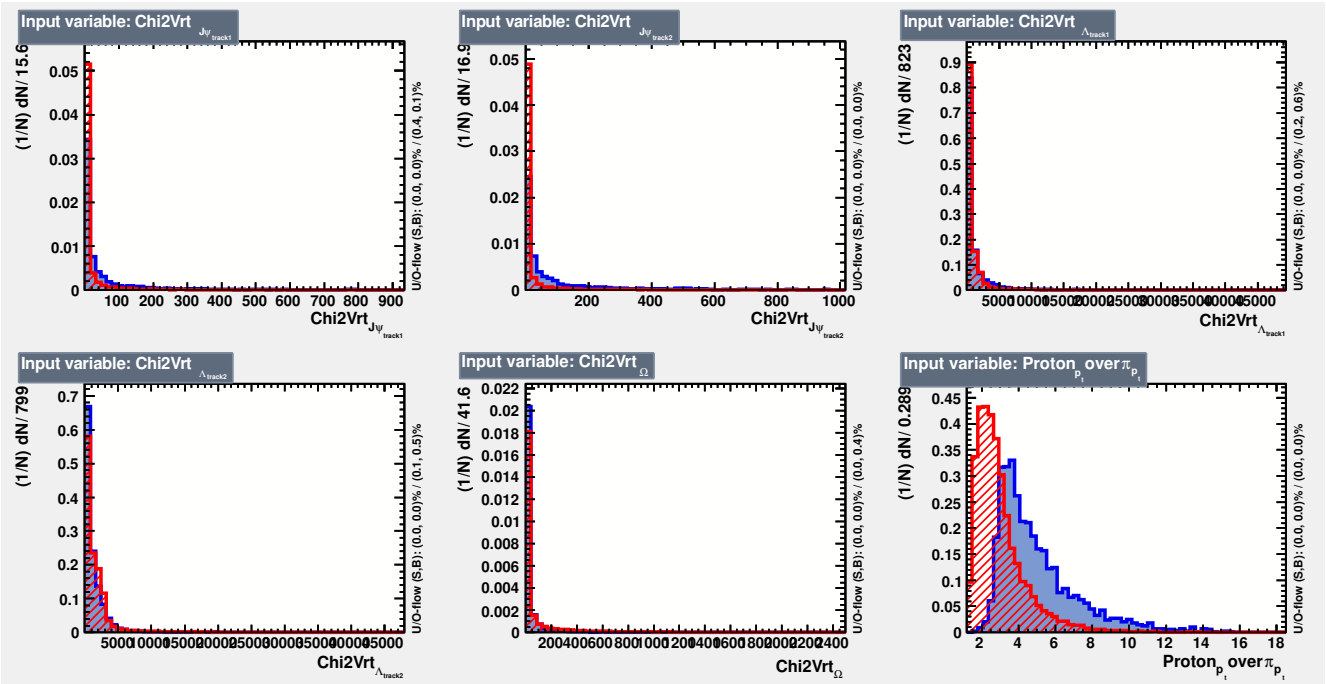

(a) variables 37–42

Figure 11: Ω_b^- Signal and background distributions for input variables 37–42 included in the BDT[42] discriminant.

Apendix D Correlations between BDT Input Variables

The two dimensional grid of parameter correlations for Ξ_b^- signal and background samples, for the 42 variable BDT, are shown in Figs. 12 and 13, respectively. In each case, these plots are divided into four quadrants for ease of interpretation.

The corresponding Ω_b^- plots are shown in Figs. 14 and 15.

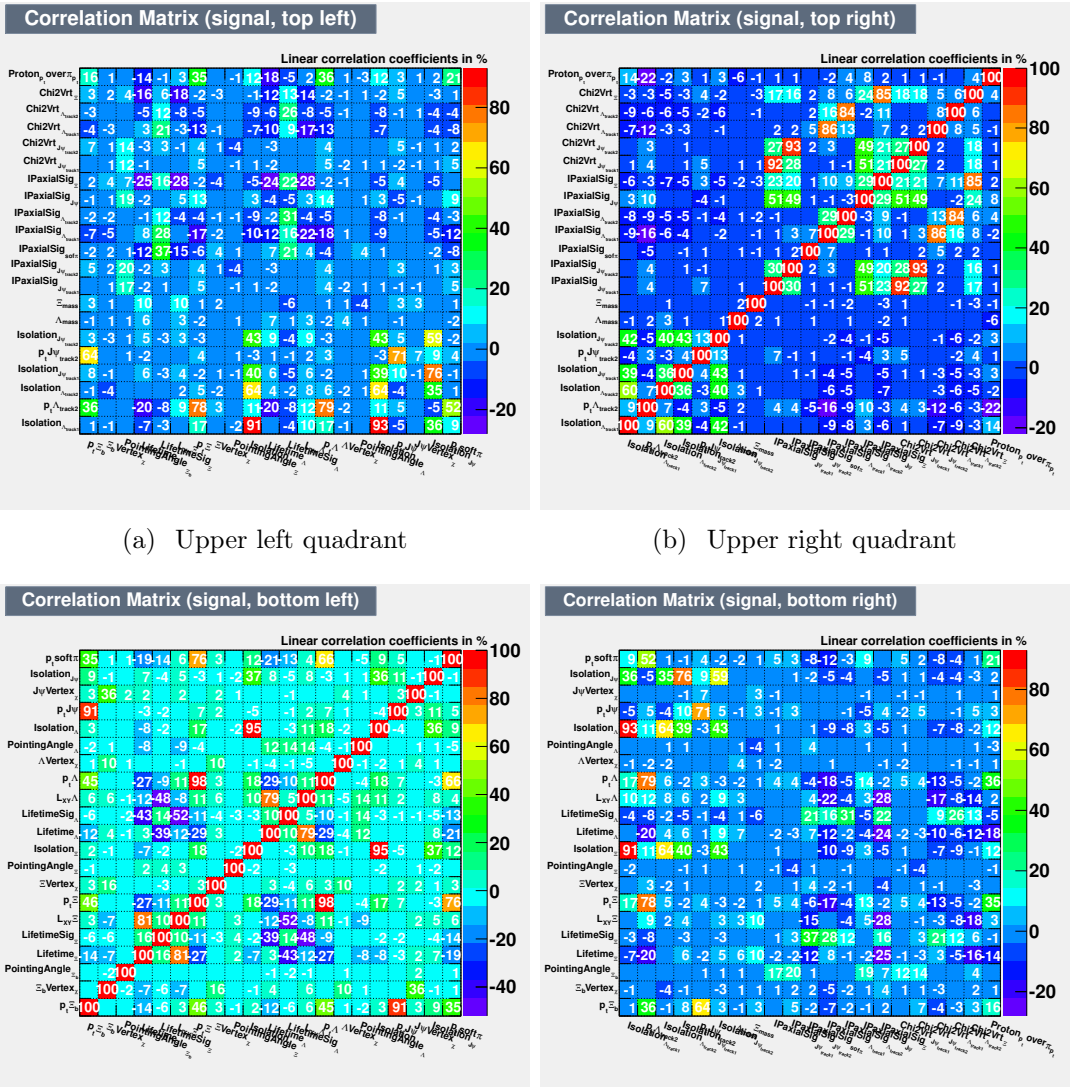

(a) Upper left quadrant

(b) Upper right quadrant

(c) Lower left quadrant

(d) Lower right quadrant

Figure 12: Correlations for the Ξ_b^- signal training sample, for all variables included in the BDT[42] discriminant. Note that the four quadrants have different scales, and hence slightly different color codes.

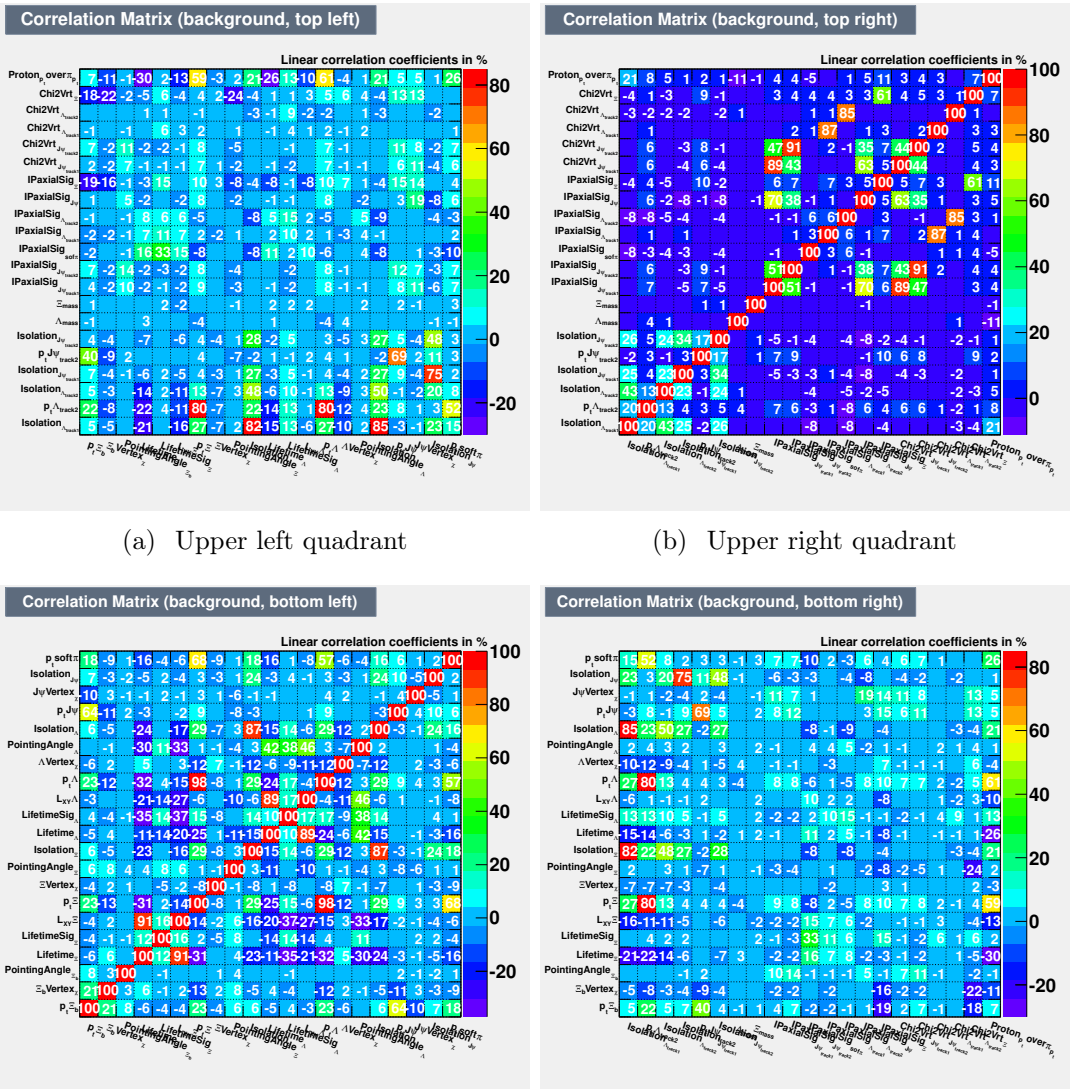

(a) Upper left quadrant

(b) Upper right quadrant

(c) Lower left quadrant

(d) Lower right quadrant

Figure 13: Correlations for the Ξ_b^- background training sample, for all variables included in the BDT[42] discriminant. Note that the four quadrants have different scales, and hence slightly different color codes.

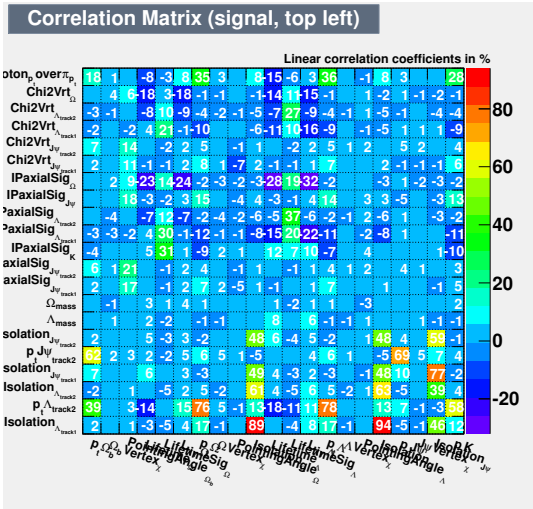

(a) Upper left quadrant

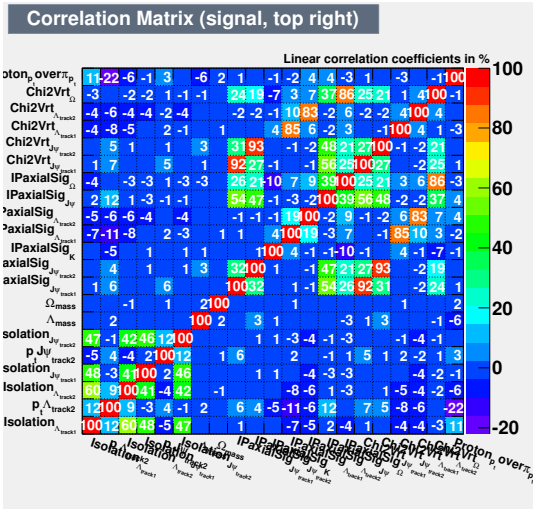

(b) Upper right quadrant

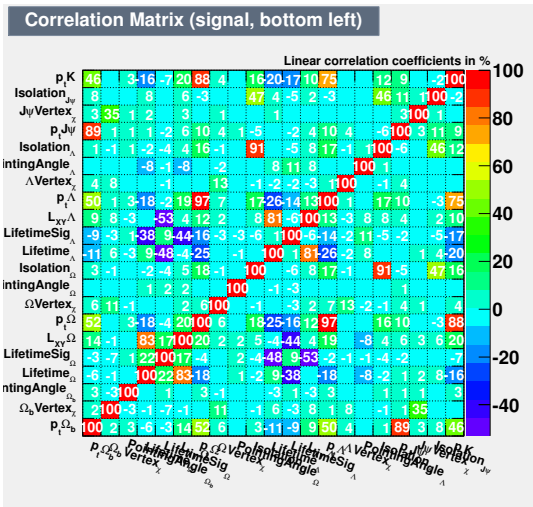

(c) Lower left quadrant

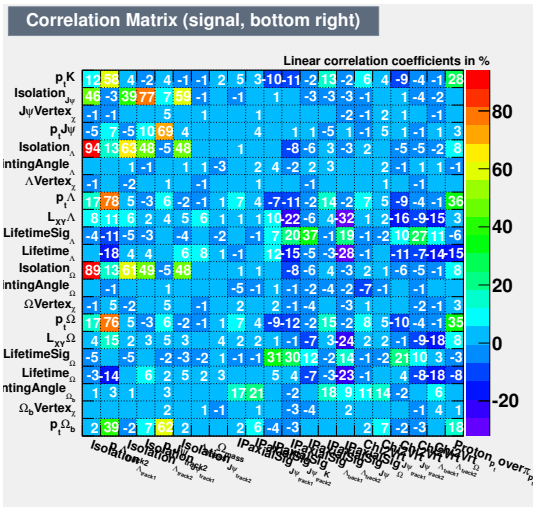

(d) Lower right quadrant

Figure 14: Correlations for the Ω_b^- signal training sample, for all variables included in the BDT[42] discriminant. Note that the four quadrants have different scales, and hence slightly different color codes.

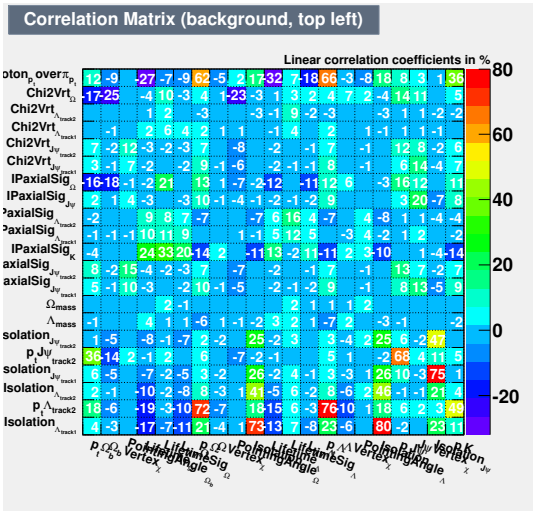

(a) Upper left quadrant

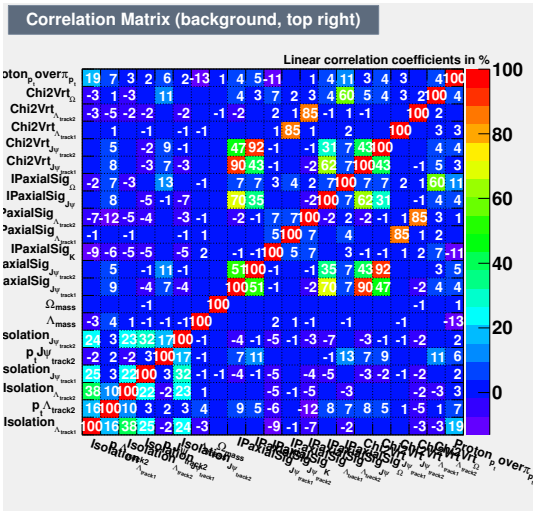

(b) Upper right quadrant

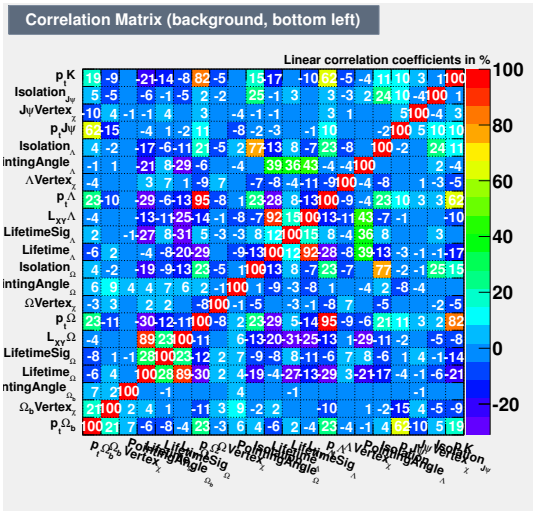

(c) Lower left quadrant

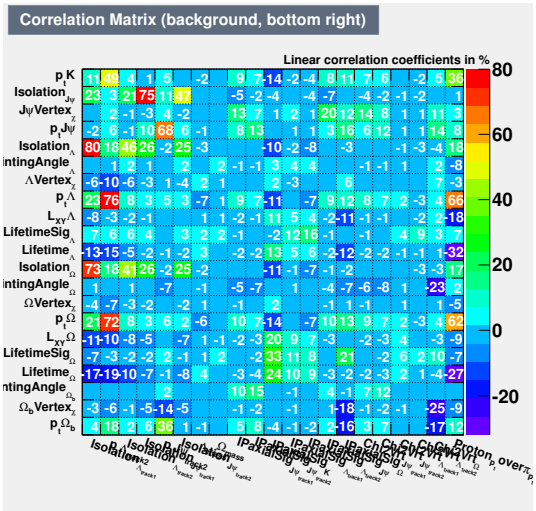

(d) Lower right quadrant

Figure 15: Correlations for the Ω_b^- background training sample, for all variables included in the BDT[42] discriminant. Note that the four quadrants have different scales, and hence slightly different color codes.

Apendix E Correlations between $M(\Xi_b^-)$ and BDT Variables

The correlation coefficients between $M(\Xi_b^-)$ and the 42 input variables used in the BDT, for both signal and background training samples, are listed in Table 2.

Variable	$M(\Xi_b^-)$ correlation coefficient (%) signal	background
$\tau(\Xi^-)$	-1	2
$\tau(\Lambda^0)$	-2	0
$\cos(\theta_{\Xi^-})$	-2	2
$L_{xy}(\Xi^-)$	0	1
$\tau^{\rm sig}(\Lambda^0)$	0	0
$p_T(\Xi_b^-)$	4	-1
$p_T(\pi_\Xi)$	0	-3
$M(\Lambda^0)$	6	2
$M(\Xi^-)$	11	0
$\chi^2_{\rm PV\to}(p)$	-1	0
$\tau^{\rm sig}(\Xi^-)$	0	0
$\chi^2_{\rm PV\to}(\Xi^-)$	-1	-3
$\chi^2_{\rm PV\to}(\pi_\Lambda)$	0	0
$p_T(\mu_2)$	0	0
${\rm IP}^{\rm sig}(\mu_2)$	-2	-2
$I(J/\psi)$	1	4
$\cos(\theta_{\Xi_b^-})$	0	0
$p_T(p)/p_T(\pi)$	4	-4
$I(\Xi^-)$	1	0
${\rm IP}^{\rm sig}(\mu_1)$	0	-2
$\chi^2_{\rm PV\to}(\mu_2)$	-3	-2
${\rm IP}^{\rm sig}(\pi_\Xi$	0	0
$L_{xy}(\Lambda^0)$	0	-1
$p_T(\pi_\Lambda)$	2	-4
$p_T(\Xi^-)$	6	-5
$\cos(\theta_{\Lambda^0})$	-2	-1
$\chi^2_V(J/\psi)$	0	-1
$\chi^2_V(\Lambda^0)$	2	0
${\rm IP}^{\rm sig}(p)$	-2	0
$I(\mu_2)$	0	3
$\chi^2_V(\Xi^-)$	0	0
$\chi^2_{\rm PV\to}(\mu_1)$	0	-1
$I(\mu_1)$	0	4
$\chi^2_V(\Xi_b^-)$	0	5
$p_T(\Lambda^0)$	7	-6
${\rm IP}^{\rm sig}(\Xi^-)$	1	-4
$I(\Lambda^0)$	1	0
$I(p)$	1	0
$p_T(J/\psi)$	3	1
${\rm IP}^{\rm sig}(J/\psi)$	-1	-1
${\rm IP}^{\rm sig}(\pi_\Lambda$	0	0
$I(\pi_\Lambda)$	0	0

Table 2: Correlation coefficients between $M(\Xi_b^-)$ and each of the 42 input variables used in the BDT, for both signal and background training samples.

Apendix F $M(\Xi_b^-)$ distribution for wrong-sign events as the BDT cut is tightened

The wrong-sign Ξ_b^- candidates are by construction signal-free, and hence show the effect of the BDT on the mass-dependence of background. Figures 16–17 show the $M(\Xi_b^-)$ distributions for successively tighter BDT cuts.

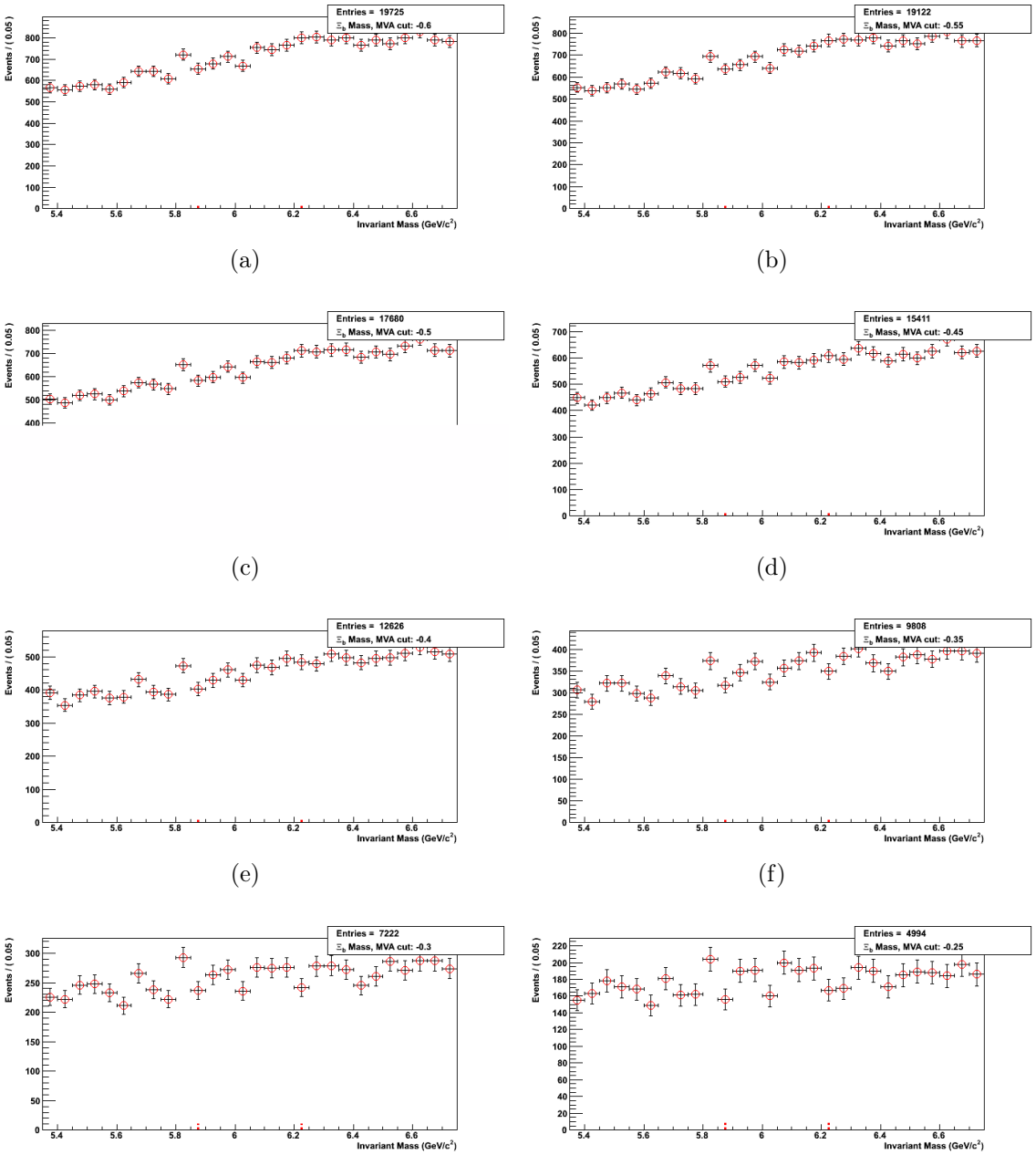

Figure 16: $M(\Xi_b^-)$ distributions, for wrong-sign events, as successively tighter BDT cuts are applied.

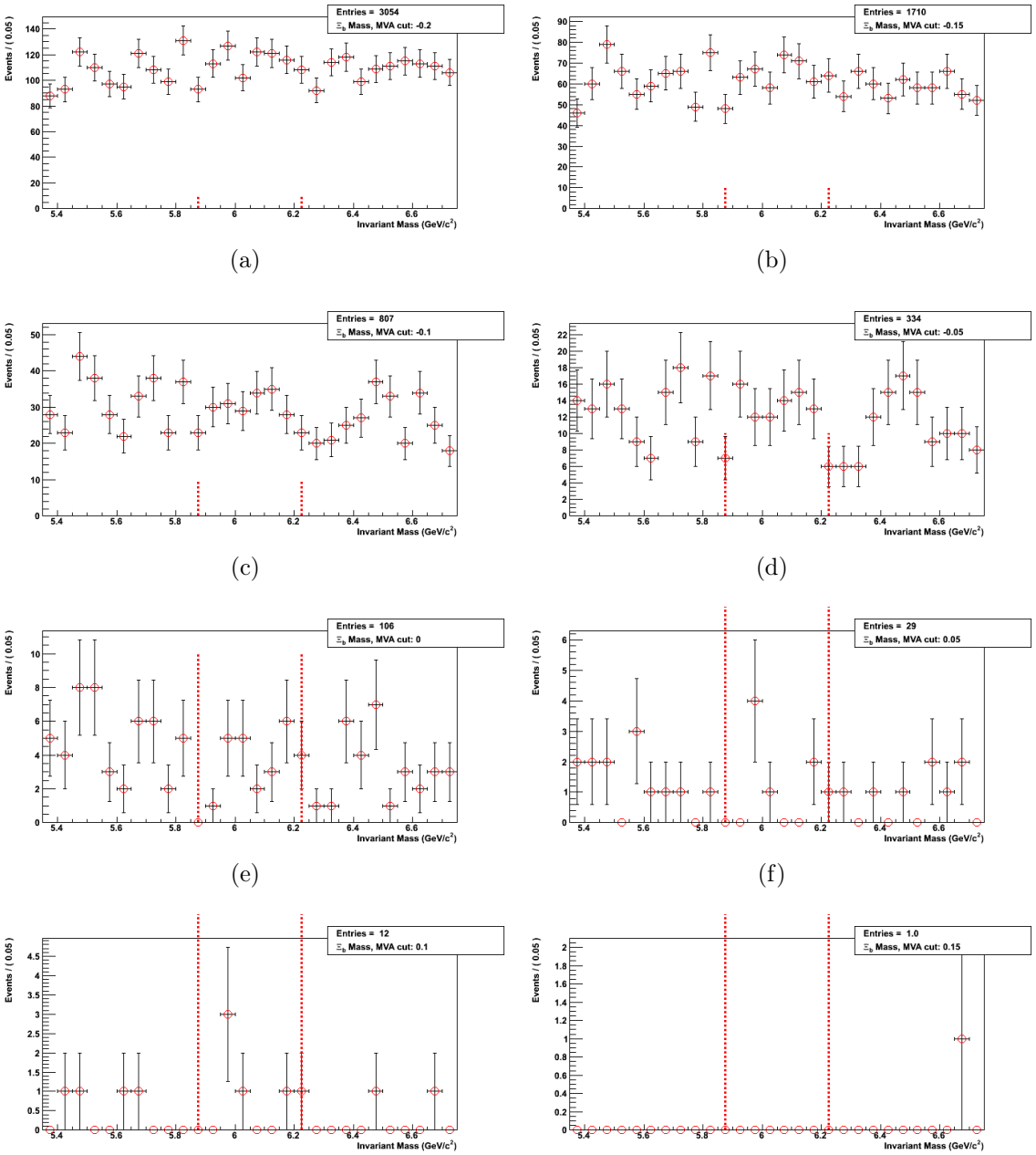

(a) (b) (c) (d) (e) (f) (g) (h)

Figure 17: $M(\Xi_b^-)$ distributions, for wrong-sign events, as successively tighter BDT cuts are applied.

Apendix G Comparing results with 2007 and 2011 extended tracking versions (Run IIa)

Part of the difficulty in making comparisons between the original DØ Ξ_b^- and Ω_b^- publications, and this new analysis, is that the former used the 2007 version of the extended tracking algorithm, whereas the latter uses the 2011 version. The most significant change is that the 2007 version performed all the tracking from scratch, throwing away the tracks found with the default algorithm; in contrast, the 2011 version merges the lists of tracks found by the default and extended algorithms, with some intelligent discarding of duplicate tracks.

The 2007 version is only available for Run IIa, as there were technical problems in implementing it for Run IIb. The 2011 version is available for both Run IIa and Run IIb, hence the IIa sample is the only one available for making comparisons between the versions.

In practice, while the 2011 approach sounds more efficient, it can actually be less so as a result of oversaturation of shared hits in the track-finding process. Each track has a limit on the number of 'shared hits' it can use, and more tracks result in more shared hits, and hence a lower efficiency of this requirement.

A large number of studies were undertaken to investigate the performance of the 2007 and 2011 versions. In general, for the sub-sample of events that are common to both versions after the J/ψ skim, the 2011 algorithm gives larger yields of J/ψ, Λ^0, and Ξ^- signal candidates in Run IIa data. There is also a small additional set of events that are only present for the 2011 version: these events likely failed the J/ψ skim requirements for the 2007 version, probably because one of the muon tracks was not reconstructed.

Figure 18 shows a comparison of the 2007 and 2011 Run IIa data, after application of the same selection requirements imposed on the original publication (so-called 'PRL cuts') [22]. Figure 19 shows a similar comparison of the 2007 and 2011 Run IIa data, but after application of the BDT cut (BDT42 > 0.130).

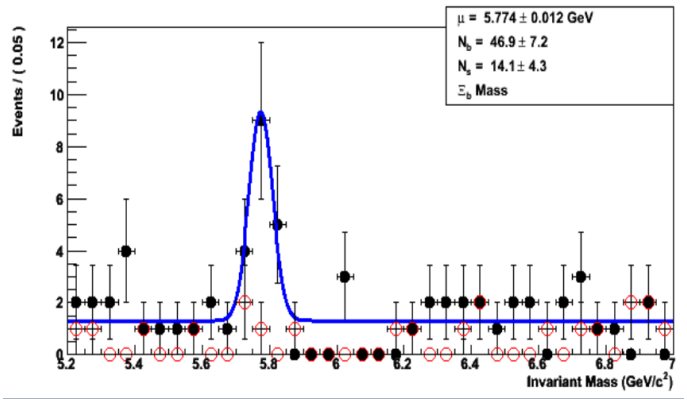

(a) 2007 XAA algorithm

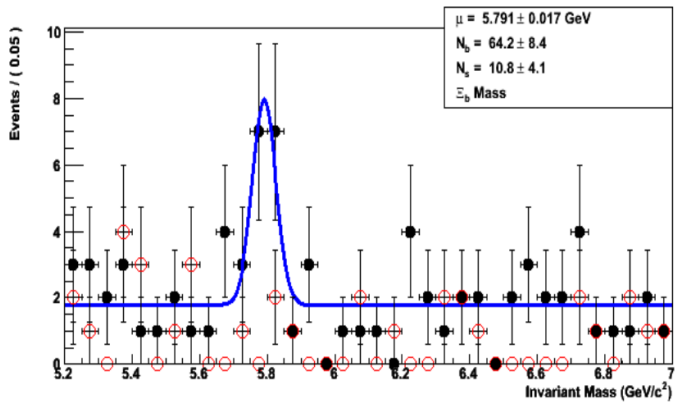

(b) 2011 XAA algorithm

Figure 18: Comparison of the Run IIa data as reconstructed using the 2007 and 2011 versions of the extended tracking algorithm (XAA), after application of the cuts used in the original publication. The 2007 version has lower background, and perhaps slightly more signal: this was the version used for the original publication. The 2011 version accepts additional tracks, giving higher backgrounds, but may also have a lower signal efficiency.

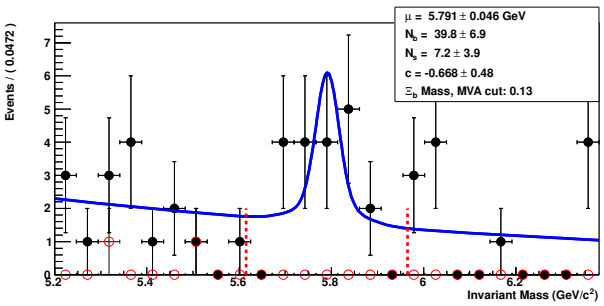

(a) 2007 XAA algorithm

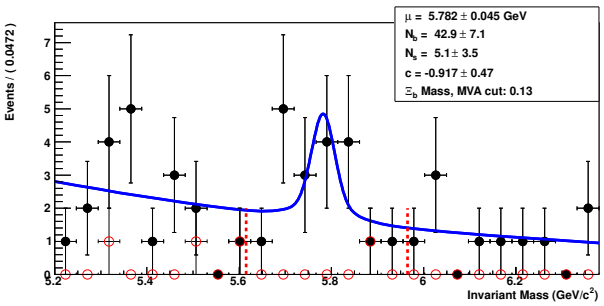

(b) 2011 XAA algorithm

Figure 19: Comparison of the Run IIa data as reconstructed using the 2007 and 2011 versions of the extended tracking algorithm (XAA), after application of the BDT cut used in this new analysis.

Apendix H Event-by-event comparison of Run IIa Ω_b^- candidates from original publication and new analysis

The PRL2008 analysis selected a total of 78 events after all requirements. Of these, 32 events are not even present in the data sample after the new extended tracking algorithm is applied. Of the remaining 46 events, just one fails the preselection requirements, while 11/45 of the preselected events fail the data quality requirements, and just 7/34 of these pass the BDT cut.

These results are summarised in Tables 3–4. The former lists the 71/78 events from PRL2008 that fail the final requirements of the new analysis, showing at which stage of the selection chain they fail (the order is: BANA, preselection, data quality, BDT). The second table shows the 34 PRL2008 events that pass the quality requirements, and shows the BDT output value of each candidate from the new analysis (the final selection criterion is BDT>0.100). The seven events passing this BDT requirement are shown in blue.

Table 4 also shows information on the reconstructed Ω_b^- masses, from both PRL2008 and the new analysis, and their difference. Note that this is just a comparison of the event numbers - the specific tracks used to build the b baryon candidates may differ between the two analyses, since the track reconstruction has been re-performed. The shifts are typically of order 20 MeV between the two versions, with some outlisers having even larger differences. For scale, the mass resolution is around 30 MeV for this channel.

Table 3: List of the 71/78 Ω_b^- events from the original DØ publication (PRL2008, using only Run IIa data) that fail the final requirements of the new analysis, showing at which stage of the selection chain they fail (the order is: BANA, preselection, data quality, BDT). The fourth column shows whether the candidate is in the signal (S) or background (B) regions.

Run	event	M(PRL) (MeV)	mass region (S/B)	failed
152419	773856	6335.624	S	BDT
160585	554395	6154.512	S	BDT
163943	4409921	6286.062	S	BDT
167300	1360420	5990.438	S	BANA
168715	4944530	6740.241	B	BANA
173016	14553526	6198.785	S	BANA
174999	41823047	6917.226	B	BANA
176298	6684569	5808.267	B	BANA
176566	10253398	6533.040	B	BDT
177889	29415557	6010.407	S	BANA

Table 3: (continued)

Run	event	M(PRL) (MeV)	mass region (S/B)	failed
177935	1100858	6104.838	S	BANA
178242	34631417	6267.342	S	BDT
178446	2143	5945.344	S	BDT
179066	5036775	5685.159	B	BDT
179194	8663968	5867.919	B	BANA
179236	61796454	5674.977	B	BANA
179910	41520853	6082.665	S	BANA
180208	1713982	6166.889	S	BDT
180736	18427541	6163.343	S	Quality
187818	74249875	5916.054	B	BANA
188028	16573826	6172.063	S	BANA
189317	25412866	6678.204	B	BANA
189400	38941529	6709.374	B	BANA
191330	45751824	6332.727	S	BDT
191617	26759040	6205.100	S	BDT
192580	77820161	6212.005	S	BANA
192667	51883621	6013.875	S	BDT
192872	91767441	5764.635	B	BDT
193800	40131420	6197.710	S	BDT
194729	52839533	6117.869	S	BDT
195139	75494624	6720.045	B	BDT
195239	13018117	6162.319	S	BANA
195381	67225740	6796.250	B	Quality
195565	72670485	5765.104	B	BDT
203266	4351525	6389.002	B	BANA
203613	50042678	6554.440	B	BDT
203929	22881065	6158.335	S	Quality
204009	15108647	6162.176	S	BDT
204010	25983617	6565.955	B	Quality
204158	53612596	6751.408	B	BDT
204159	73163351	6718.659	B	BANA
206917	80642851	5894.412	B	BANA
207020	115025112	5951.568	S	BANA
207231	2188630	6533.908	B	BANA
207255	65033880	6177.860	S	BDT
207291	22632859	6792.820	B	BANA
207354	28412162	6004.997	S	BDT
207571	20570372	5783.729	B	BDT

Table 3: (continued)

Run	event	M(PRL) (MeV)	mass region (S/B)	failed
207867	41954385	6825.897	B	Quality
208	110255687	6079.188	S	PSelec
208121	39312631	5727.999	B	BANA
208691	10703838	5918.028	B	BANA
209165	54484753	5680.678	B	Quality
209613	31938752	6162.704	S	Quality
210159	57181987	6061.770	S	BDT
210172	24829066	6112.304	S	BANA
210215	11632454	6276.017	S	BANA
210421	87644530	6163.563	S	BDT
210609	36508887	6967.876	B	BDT
211252	39151457	6746.307	B	Quality
211481	81822578	6983.675	B	BDT
211814	79361986	5957.745	S	BANA
211917	41206905	6156.171	S	BANA
212088	21960775	6639.544	B	Quality
213245	3711233	6468.697	B	BDT
213256	78789672	5765.941	B	BANA
213309	34358251	6105.085	S	BANA
213390	65577220	6490.448	B	BANA
213407	33689402	6552.200	B	Quality
213608	33401485	6172.512	S	BANA
215596	12128479	5764.680	B	Quality

Table 4: List of the 34 PRL2008 events that pass the quality requirements for the new analysis. Shown are the BDT output value of each candidate from the new analysis (the final selection criterion is BDT$>$ 0.100). The seven events passing this BDT requirement are shown in blue. Also shown are the reconstructed Ω_b^- masses, from both PRL2008 and the new analysis, and their difference.

Run	event	M(PRL) (MeV)	M(now) (Mev)	M(PRL) - M(now) (MeV)	mass region (S/B)	BDT value
152419	773856	6335.6	6324.2	11.3	S	0.069891
160585	554395	6154.5	6326.2	-171.7	S	0.029044
163943	4409921	6286.0	6300.6	-14.6	S	-0.168170
167288	36793546	6199.7	6227.2	-27.5	S	0.144836
170016	14492331	5861.0	5861.5	-0.5	B	0.103025
176534	6644838	5772.7	5789.9	-17.3	B	0.194634
176566	10253398	6533.0	6540.7	-7.6	B	-0.094977
178242	34631417	6267.3	6258.2	9.1	S	-0.091480
178446	2143000	5945.3	5944.3	0.9	S	0.070591
179066	5036775	5685.1	5688.7	-3.5	B	-0.559770
179070	10936802	5950.6	5933.0	17.6	S	0.131546
180208	1713982	6166.8	6103.6	63.2	S	-0.363628
191330	45751824	6332.7	6313.0	19.6	S	0.052850
191617	26759040	6205.1	6153.9	51.1	S	-0.113657
191622	75966101	6168.6	6153.5	15.1	S	0.154156
192667	51883621	6013.8	6007.7	6.0	S	0.089706
192872	91767441	5764.6	5763.7	0.8	B	0.094999
193800	40131420	6197.7	6188.9	8.8	S	0.008282
194729	52839533	6117.8	6133.4	-15.5	S	0.008753
195139	75494624	6720.0	6679.5	40.4	B	-0.146652
195565	72670485	5765.1	5776.3	-11.2	B	0.056670
203613	50042678	6554.4	6554.9	-0.5	B	-0.329571
203978	41379640	6587.3	6570.5	16.8	B	0.186315
204009	15108647	6162.1	6199.8	-37.6	S	0.072302
204158	53612596	6751.4	6744.0	7.4	B	0.042661
207255	65033880	6177.8	6181.8	-4.0	S	-0.082125
207291	20553215	6183.1	6153.9	29.2	S	0.119638
207354	28412162	6004.9	6023.7	-18.7	S	-0.070121
207571	20570372	5783.7	5777.6	6.0	B	-0.004082
210159	57181987	6061.7	6057.7	4.0	S	-0.411638
210421	87644530	6163.5	6213.6	-50.0	S	-0.096034
210609	36508887	6967.8	6970.0	-2.2	B	-0.532661

Table 4: (continued)

Run	event	M(PRL) (MeV)	M(now) (Mev)	M(PRL) - M(now) (MeV)	mass region (S/B)	BDT value
211481	81822578	6983.6	6978.2	5.4	B	-0.324039
213245	3711233	6468.6	6458.3	10.3	B	-0.286283